

Microstructure Characterization of Continuous-Discontinuous Fibre Reinforced Polymers based on Volumetric Images

Zur Erlangung des akademischen Grades eines
Doktors der Ingenieurwissenschaften
(Dr.-Ing.)

bei der Fakultät für Maschinenbau
des Karlsruher Instituts für Technologie (KIT)

genehmigte
DISSERTATION

von
M.Sc. Pascal Pinter
aus
Bad Mergentheim

Datum der mündlichen Prüfung: 24. April 2018
Referent: Prof. Dr.-Ing. Peter Elsner
Korreferenten: Prof. Dr. Kaan Inal
Prof. (apl.) Dr.-Ing. Kay André Weidenmann

Preface

The work was performed in the group of Hybrid and Lightweight materials, Institute of Applied Materials at the Karlsruhe Institute of Technology, during the period of May 2015 to February 2018. The research documented in this thesis has been funded by the German Research Foundation (DFG) within the International Research Training Group "Integrated engineering of continuous-discontinuous long fibre reinforced polymer structures" (GRK 2078). The support by the German Research Foundation (DFG) is gratefully acknowledged.

I would like to thank my supervisor Peter Elsner and co-supervisor Kay André Weidenmann for supporting my work in the past three years and for many thought-provoking impulses. Furthermore, their quick and sometimes spontaneous helpfulness in urgent situations is greatly acknowledged.

I also want to thank my co-supervisor Kaan Inal from the University of Waterloo in Canada for his professional support. He and his entire work group have been very welcoming and helpful during my stay in Canada. Not only in technical competence, but also during settling in the life abroad.

The help of the Institute for Engineering Mechanics (ITM), especially of Loredana Kehrer, with understanding mechanical models for fibre reinforced polymers is gratefully acknowledged.

Furthermore, I would like to thank the technical staff of IAM-WK and the mechanics of the machine shop for their fast and good work whenever I needed help.

Many thanks to my colleagues from IAM-WK for the excellent collaboration and the pleasant working environment.

Moreover, I would like to thank the students Anselm Heuer, Ludwig Schöttl and Lukas Englert who have supported my work for the present thesis.

Special thanks to Benjamin Bertram who helped a lot with understanding object-oriented programming when I started implementing image processing tools. I also like to thank Stefan Dietrich for many valuable discussions.

I am deeply grateful to my family and for their support and in particular to my fiancée Annerose for her patience in recent years.

Abstract

Extracting quantitative descriptors from computed tomography scans of fibre reinforced polymers is essential for modelling mechanical and thermal properties. The precision of CT-scanners has been improved significantly in recent years and thus, images with an resolution below one micro meter can be acquired. Modern age computers offer the opportunity to process those large data-sets of volumetric image data and to extract significant statistics.

The present thesis deals with the quantification of microstructural features of fibre reinforced polymers from CT-scans. Therefore, various algorithms have been implemented and validated in order to determine the fibre orientation, volume fraction, curvature and length. Furthermore, two approaches for the evaluation of surface curvature have been compared.

Results show that some of the available methods for fibre orientation analysis are very robust and thus, also very noisy and low contrast images can be processed with sufficient accuracy. Fibre length distributions derived from fibre tracking algorithms lead to very good correspondence compared with conventional methods at a specimen size of up to 5 mm while data from larger samples is less reliable.

Kurzfassung

Die quantitative Beschreibung der Mikrostruktur von Faserverbundwerkstoffen ist elementar für die Modellierung von thermischen und mechanischen Eigenschaften. Durch die stetige Entwicklung der Computertomographie ist es heute möglich dreidimensionale Bilddaten von Werkstoffen mit einer Auflösung von unter einem Mikrometer zu erzeugen. Moderne Computersysteme bieten ausreichend Rechenleistung um die resultierenden volumetrischen Bilddaten automatisiert auszuwerten und relevante Statistiken zu erzeugen.

Die vorliegende Arbeit befasst sich mit der Quantifizierung von mikrostrukturellen Merkmalen von faserverstärkten Polymeren unter Verwendung von computertomographischen Aufnahmen. Diverse Verfahren zur Bestimmung von lokalen Faserorientierungen, -volumengehalt, -krümmungen und -längen wurden implementiert und validiert. Des Weiteren wurden zwei Ansätze zur Berechnung von lokalen Oberflächenkrümmungen zur Porositätsanalyse verglichen.

Die Ergebnisse zeigen, dass einige der bereits verfügbaren Orientierungsanalyseverfahren bereits sehr robust sind und auch mit stark verrauschten Aufnahmen mit geringem Kontrast sehr gute Resultate erzielen. Faserlängenverteilungen, die mittels Fasertrackingverfahren aus computertomographischen Aufnahmen extrahiert wurden lieferten nur bis zu einer Probengröße von 5 mm verlässliche Faserlängenverteilungen und sind daher nur bedingt für die Anwendung an langfaserverstärkten Polymeren geeignet.

Symbols and Abbreviations

Abbreviations

ANTs	Advanced Normaization Tools
APL	Attenuation path length
ART	Algebraic reconstruction techniques
CF	Carbon fibre
CoDiCo	Continuous-discontinuous
CT	Computed tomography
DiCo	Discontinuous
FLD	Fibre length distribution
FOD	Fibre orientation distribution
GF	Glass fibre
IBOF	Invariant-based optimal fitting
IDD	Interaction direct derivative
IM	Injection moulding
ITK	Insight Segmentation and Registration Toolkit
LFRP	Long fibre reinforced polymer
LFT	Long-Fibre-Reinforced Thermoplastic

Symbols and Abbreviations

ODF	Orientation distribution function
PP	Polypropylene
RVE	Representative Volume Element
SC	Self-consistent
SMC	Sheet Moulding Compound
SVE	Statistical Volume Element
SVR	Support vector regression
TGA	Thermogravimetric analysis
UD	Unidirectional
UPPH	Unsaturated polyester polyurethane resin
VTK	Visualization Toolkit

Latin Letters - Scalars

\overline{FD}	<u>F</u> ocus- <u>D</u> etector distance
\overline{FO}	<u>F</u> ocus- <u>O</u> bject distance
A, B, C, D, E	Partial sums over image histogram
a_i	Angular deviation
c	Coherence measure
c_v	Volume fraction
c_w	Weight fraction
D_x	Filter mask for numerical derivative in x
D_y	Filter mask for numerical derivative in y
E_A	Average over all global errors θ_{gE} of a set of test images

E_c	Error criterion for curvature
E_T	Tensor-based error
$E_{c,p}$	Percentage error criterion for curvature
f_l	Fibre length distribution function
h	Filter mask
I	Input image
I_0	Initial intensity
I_D	Remaining Intensity behind an object
L	Fibre length
l	Transmission length
N_G	Maximum grey value dependent on data type
N_p	Total number of projections acquired for a single scan
O	Orientation space
p	Set of material parameters
p_i	Weight function
R	Fibre radius
$r(\cdot)$	Highest filter response of the anisotropic Gaussian filter
R_μ	Relative attenuation
S	Surface
s_d	Detector voxel size
s_i	Voxel spacing
s_o	Object voxel size
t	Thresholding value
V	Volume

Symbols and Abbreviations

W	Window for filter mask
w	Weight

Latin Letters- Vectors

b	Binormal vector
f	Function of parametrized spatial curve
n	Fibre orientation vector
n_s	Normal vector
t	Tangent vector
v	Eigenvector corresponding to the highest filter response
z	Function of spatial curve parametrized in dependence of the arc length

Latin Letters - 2nd Order Tensors

H	Hessian matrix
J	Structure tensor
N	Orientation tensor
S	Shape operator

Latin Letters - 4th Order Tensors

C	Stiffness tensor
-----	------------------

x

\mathbb{N} Orientation tensor

Greek Letters - Scalars

α Absorption coefficient
 δ Dirac's delta distribution
 γ Directional accordance
 κ Curvature
 κ_G Gaussian curvature
 κ_M Mean curvature
 κ_{max} Maximum curvature
 κ_{min} Minimum curvature
 κ_n n-th principal curvature
 λ Eigenvalues
 λ_w Wavelength
 μ Attenuation coefficient
 μ_s Scatter coefficient
 μ_t Quotient of partial sum for thresholding
 ν Eigenvectors
 ϕ Azimuth angle
 ψ Orientation distribution function
 ρ Density
 Σ Covariance matrix
 σ Standard deviation

Symbols and Abbreviations

τ	Torsion
θ	Elevation angle
θ_E	Angle between real and measured orientation
θ_{gE}	Averaged θ_E over the entire image

Indizes

$(\cdot)_\rho$	Second iteration of Gaussian filtering for calculation of the structure tensor
$(\cdot)_\sigma$	Gaussian filtered
$(\cdot)_a$	Angular
$(\cdot)_c$	Composite
$(\cdot)_f$	Fibre
$(\cdot)_I$	Input
$(\cdot)_m$	Matrix
$(\cdot)_O$	Output
$(\cdot)_r$	Radial
$(\cdot)_s$	Coefficient of the shape operator
$(\cdot)_t$	Related to thresholding value
$(\cdot)_{tot}$	Total

Image Operators

$\kappa(\cdot)$	Coherence measure
-----------------	-------------------

$\mathbf{H}(\cdot)$	Hessian matrix
$\mathbf{J}(\cdot)$	Structure tensor
$D(\cdot)$	Numerical derivative
$f_{cv}(\cdot)$	Circular voting filter
$G(\cdot)$	Gaussian filter
$w(\cdot)$	Medialness filter

Symbols

$(\cdot)^{\top}$	Transposed
$(\cdot)_{\perp}$	Normal direction
*	Convolution
\cdot	Scalar product
Δ	Difference
∇	Gradient
$\overline{(\cdot)}$	Effective values
∂	Partial derivative

Contents

Abstract	iii
Kurzfassung	v
Symbols and Abbreviations	vii
1 Introduction	1
1.1 Motivation	1
1.2 Objectives	2
2 State of the Art	3
2.1 Preliminary Remarks	3
2.1.1 Notation	3
2.1.2 Representative and Statistical Volume Element	3
2.2 Computed Tomography	4
2.2.1 Principle	4
2.2.2 Reconstruction	6
2.3 Image Processing	6
2.3.1 Image Histogram	7
2.3.2 Fundamental Filters	7
2.3.3 Segmentation of Images	9
2.3.4 Skeletonization	13
2.4 Fibre Orientation Distribution	15
2.4.1 Methods for Orientation Determination from Microscopic Images	15
2.4.2 Voxel-based Methods from 3D Images	17
2.4.3 Statistical Descriptors of Orientation	22
2.5 Fibre Length Distribution	25
2.5.1 Destructive Methods for FLD Determination	26
2.5.2 Non-Destructive Fibre Length Distributions from CT Im- ages using Fibre Tracking Approaches	27
2.6 Fibre Volume Content	29
2.6.1 Specimen Incineration	29
2.6.2 Principle of Archimedes	30
2.6.3 X-Ray based Methods	30

Contents

2.7	Porosity and Inclusion Analysis	31
2.7.1	Descriptors for Morphology	31
2.7.2	Surface Curvature	32
2.8	Application in Homogenisation of Mechanical Properties	35
2.9	Research Questions	36
3	Material	39
3.1	Long Fibre Reinforced Polymers (LFRP)	40
3.1.1	Sheet Moulding Compounds	40
3.1.2	Long Fibre Reinforced Thermoplastic	44
3.1.3	Overview LFRP	44
3.2	Validation Materials	45
3.2.1	Fibre Orientation Distributions	46
3.2.2	Fibre Volume Content	47
3.2.3	Fibre Tracking and Fibre Length Distributions	49
3.2.4	Surface Curvature	49
4	Development of Analytical Methods	53
4.1	Fibre Orientation Distribution	53
4.1.1	Implementation of Voxel-Based Methods	53
4.1.2	Statistical Orientation Distributions	56
4.1.3	Artificial Images and Error Criterion	59
4.1.4	Separation of different Microstructures	61
4.2	Fibre Tracking in CT-images	62
4.2.1	Circular Voting Filter	62
4.2.2	Segmentation and Skeletonization	64
4.2.3	Tracking Algorithm	65
4.2.4	Parametrization of Spatial Curves	66
4.2.5	Fibre Length Distribution from Spatial Curves	69
4.2.6	Fibre Orientation Tensors from Spatial Curves	69
4.2.7	Fibre Curvature and Torsion from Spatial Curves	69
4.3	Porosity and Inclusion Analysis	71
4.3.1	Segmentation and Volume Fraction	71
4.3.2	Determination of Surface Curvature	71
5	Experimental	75
5.1	CT-Scanners	75
5.1.1	YXLON CT Precision	75
5.1.2	Zeiss Xradia 520 Versa	76
5.2	Fibre Orientation Distribution	76
5.2.1	Artificial Images	76
5.2.2	Real Images with known Orientation	78
5.2.3	LFRP Material	80

5.3	Fibre Volume Fraction	82
5.3.1	Thresholding Techniques for CT Images	82
5.3.2	Thermogravimetric Analysis (TGA)	83
5.4	Fibre Length Distribution and Fibre Tracking	83
5.4.1	FibreShape FiVer	84
5.4.2	FASEP	84
5.4.3	μ CT Investigations	84
5.5	Surface Curvature Analysis	88
5.5.1	Artificial Images	88
5.5.2	Real Images with known Curvature	88
5.5.3	Pore Analysis on Continuous CFRP	89
6	Results	91
6.1	Fibre Orientation Distribution	91
6.1.1	Artificial Images with One and Two Fibres	91
6.1.2	Evaluation of GeoDict [®] Structures	100
6.1.3	Real Images with known Orientation	101
6.1.4	LFRP Material	102
6.2	Fibre Volume Fraction	108
6.2.1	Thermogravimetric Analysis (TGA)	108
6.2.2	Thresholding Techniques on CT Images	108
6.3	Fibre Length Distribution	112
6.3.1	FibreShape FiVer	112
6.3.2	FASEP	112
6.4	Fibre Tracking in CT Images	113
6.4.1	Fibre Length Analysis	113
6.4.2	Curvature Analysis	115
6.4.3	Fibre Orientation Tensors	117
6.5	Surface Curvature Analysis	118
6.5.1	Artificial Images	118
6.5.2	Real Images for Validation	119
6.5.3	Pore Analysis on Continuous CFRP	122
7	Discussion	123
7.1	Fibre Orientation Distribution	123
7.1.1	Experiments on Artificial Fibres	123
7.1.2	Artificial Fibre Architectures	128
7.1.3	Real Images with known Orientation	129
7.1.4	Orientation Tensors derived from Spatial Curves	132
7.1.5	LFRP Material	132
7.2	Fibre Volume Fraction	134
7.3	Fibre Length Distribution	137
7.3.1	Optical Methods	137

Contents

7.3.2	FLD derived from CT-Images	138
7.4	Fibre Curvature	140
7.5	Surface Curvature Analysis	145
7.5.1	Surface Curvature Analysis on Artificial Images	145
7.5.2	Surface Curvature Analysis on Real Images for Validation	145
8	Conclusion	149

1 Introduction

1.1 Motivation

Long fibre reinforced materials have gained importance in automotive and aerospace industry in recent years. Discontinuous fibre reinforcements like commonly used Sheet Moulding Compounds (SMC) enable to produce complex geometries due to their good formability at low scrap rates. Moreover, there are continuous fibre reinforced polymers which provide a high stiffness and a controlled fibre alignment. Those materials are harder to process and scrap rates can get high dependent on the application. A smart combination of continuous and discontinuous fibre reinforced polymers (CoDiCo polymers) provides advantages of both material systems. Complex geometries can be produced from SMC material while load paths are reinforced locally by unidirectional fibre tapes. Especially in automotive industries, mechanical properties of new materials have to be predictable using available mechanical models. In order to design new safe cars that comply with modern security standards, reliable static simulations are needed as well as crash simulations. Therefore, the International research Training Group (GRK 2078) aims for an integrated development of continuous-discontinuous long fibre reinforced polymers. All aspects of the novel material systems from topology optimization over manufacturing to static and dynamic material testing are considered.

The thesis at hand addresses to a precise microstructure characterization and description of CoDiCo polymers and their constituents based on X-Ray computed tomography. Those investigations are crucial for mechanical models and for the validation of simulations of the manufacturing process. Fibre orientation distributions (FODs) are one of the most important characteristics especially for elastic modelling. Beside optical methods, FODs can be derived three-dimensionally from volumetric images acquired by a computed tomography system. Many algorithms have been developed to evaluate local orientations "voxel-based" from volumetric images, meaning that the orientation is estimated in each image point by consideration of the local neighbourhood. Even though there are many methods developed to evaluate this kind of data, there is a lack of information about the precision that can be achieved. Also, the performance of different algorithms on noisy and low contrast CT images

1 Introduction

are not investigated yet. A further problem is the determination of local fibre volume fractions from CT images. In fact, common threshold segmentation methods are implemented in most image processing tools, but the algorithms perform quite different on differing material combinations and fibre architectures when e.g. fibres are separated as it can be seen in LFT material or if they exist in bundles like in SMC. Fibre length distributions (FLDs) are usually determined by incineration of the matrix material and subsequent separation and optical measurement of the fibres. This conventional method has the disadvantage that fibres can break during the separation process. Furthermore, long fibres are hard to separate in general as they can be very tangled. Using a fibre tracking algorithm on high resolution image data enables to determine FLDs non-destructively from CT data. Another major advantage of fibre tracking algorithms is the opportunity to determine fibre curvatures from resulting spatial curves, what is not possible with any other known method. Pores within composite materials can influence the macroscopic mechanical properties significantly due to notch effects. Methods for determination of the pore size, sphericity and distribution within materials are already implemented in commercial tools like *VGStudio MAX* or *AVIZO*. Within this thesis, two algorithms for evaluating curvatures from voxel data are compared in order to describe the geometry of pores and to detect sharp edges by a high curvature value.

1.2 Objectives

The aim of this thesis is to develop, evaluate and compare methods for characterization of microstructures of continuous-discontinuous long fibre reinforced polymers. Therefore, a robust and efficient algorithm for orientation analysis on volumetric images has to be identified. In order to determine the fibre volume fraction of CT-scans properly, a technique has to be found which enables for the evaluation of the fibre content for different microstructures. As there is no accessible software for the non-destructive investigation of fibre lengths, a tool has to be developed to derive FLDs from volumetric images. The implementation of a fibre tracking algorithm also enables for the evaluation of fibre torsion and curvature using a parametrisation of the fibre path. For the characterization of pores within composite materials, a reliable method for the determination of surface curvatures is useful for the detection of potential notches. As a side benefit, the surface curvature can also be used to spot fibre ends.

2 State of the Art

2.1 Preliminary Remarks

2.1.1 Notation

In most parts of this work, a direct tensor notation is used. Where applicable, a component form of the tensor, i.e., index notation is used. Thus, a second order tensor reads $\mathbf{A} = A_{ij}$. The Einstein summation convention is used which implies a sum over repeated indices. Scalars are denoted by lower case letters a and Vectors by bold lowercase letters \mathbf{a} . Second and fourth order tensors are written as bold capital \mathbf{A} and doubled capital \mathbb{A} letters. The scalar product and the dyadic product are indicated by $\mathbf{A} \cdot \mathbf{B}$ and $\mathbf{A} \otimes \mathbf{B}$.

2.1.2 Representative and Statistical Volume Element

In long fibre reinforced polymers, the local microstructure can be very different depending on manufacturing parameters and the flow conditions at the present location. Due to this reason, it is not expedient to search for a representative volume element (RVE) that describes the material on the macroscale. A RVE is quite obvious for periodic microstructures where the smallest cell describes the whole microstructure (Fig. 2.1). In this case, the micro-scale can easily be linked to the macro scale. For the long fibre reinforced material used within this contribution, the microstructure in a single part can be very different according to the flow conditions and is not periodic. Thus, a description on the mesoscale, which is located between the micro and the macroscale, is needed. The description on this scale takes the statistics of a larger region into account (Fig. 2.2) and is called statistical volume element (SVE) [1]. With increasing size of the SVE, it becomes an RVE for an infinite region as it describes the overall material properties.

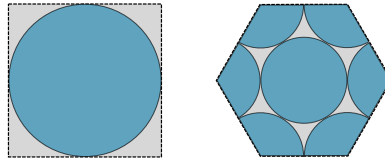


Figure 2.1: Periodic structures for continuous fibre reinforced materials.

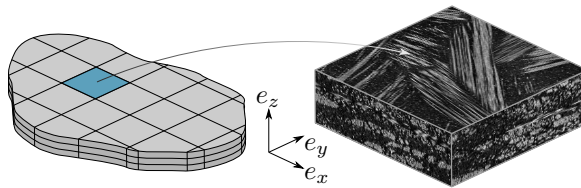


Figure 2.2: Example of a statistical volume element.

2.2 Computed Tomography

In recent years, computed tomography methods gained in image quality as well as in resolution. Modern CT scanner with a resolution of $1 \mu\text{m}$ and below allows for the investigation of inner structures within various composite materials. This enables to derive characteristics of materials using a non-destructive method, what was hardly possible a couple of years ago. The following section gives a very basic insight into the mode of operation of computed tomography. For a deeper understanding, Buzug describes the functionality of CT-scanners very briefly in "Computed Tomography" [2].

2.2.1 Principle

CT scanners are based on X-Rays and make use of the different attenuation coefficients of materials. X-Rays are generated within an X-Ray tube. Electrons are accelerated by an acceleration voltage between the filament and the target. The focussing and the displacement of the electron beam on the target is realised by magnetic lenses around the beam tube. This regulation of the focus spot is most important since it influences the blur in resulting high resolution images significantly. When electrons hit the target, bremsstrahlung is generated in form of X-Rays which are used for investigations.

2.2 Computed Tomography

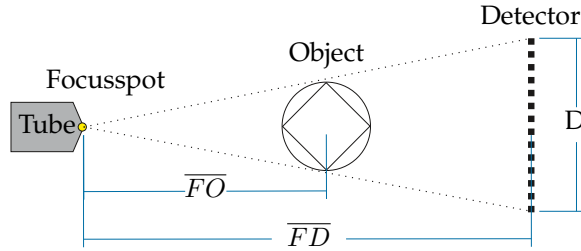


Figure 2.3: Schematic layout of a commercial computed tomography system.

The object of interest is placed on a rotatable platform between focus spot and detector. This platform and the detector can be moved in horizontal direction to adjust the image region as well as the resolution. The physical voxel size in the resulting image is given by

$$s_o = \frac{\overline{FO}}{\overline{FD}} \cdot s_d \quad (2.1)$$

where s_o is the voxel size in the objects coordinate system, s_d is the pixel size on the detector, \overline{FO} the focus object distance and \overline{FD} the focus detector distance.

In commercial CT scanners, the image intensity is captured by a detector, which consists of a scintillator in order to transform X-Rays into visible light and a CMOS sensor that captures those light impulses. In common detectors, the CMOS sensor is mounted directly on the scintillator plate, so the pixel spacing on the detector is fixed. There are also detectors with optical lenses between scintillator and sensor like e.g. in X-Ray microscopes. This technology enables to "zoom" on the scintillator to get higher physical resolutions by using a smaller region on the scintillator at the same resolution of the camera.

The general relation between attenuation coefficient, transmission length and intensity is given by the law of Lambert-Beer

$$I_D(l) = I_0 \cdot e^{\int_0^l -\mu(t) dt}. \quad (2.2)$$

I_D describes the remaining intensity at the detector after passing an object with attenuation coefficient μ for a transmission length of l along the path t while the initial intensity without an object is I_0 . The linear attenuation coefficient μ is a combination of absorption coefficient α and scatter coefficient μ_s [2].

$$\mu(x) = \mu_s(x) + \alpha(x). \quad (2.3)$$

2.2.2 Reconstruction

Using the set-up mentioned above, a certain number of two-dimensional projection images are acquired at N_p rotation angles. As a rule of thumb, at least as many images have to be acquired as the horizontal resolution of the resulting image is mentioned to be in order to fulfil all requirements for a proper reconstruction [2]. Subsequently, a volumetric image can be derived from those projections by the reconstruction. The Feldkamp algorithm is the most commonly used method up to now. It was developed by Feldkamp [3] in 1984 and enables to reconstruct three-dimensional images from cone beam CT projection images. Nevertheless, this method is only an approximation for technical investigations.

Using the Feldkamp reconstruction, X-ray radiation is assumed to be monochromatic. In reality, the attenuation coefficient is also dependent on the wavelength $\mu(\lambda_w)$. Due to this circumstance, rays with a high wavelength (soft beams) are absorbed much faster than low wavelength (hard) beams. Commonly used detectors are not energy dispersive, so the intensity at a certain point is just a scalar and not the entire spectrum of the light. As this information is missing, reconstruction methods also do not take the spectrum into account and as a result, components made of dense materials are shown darker in the centre than on the edge. Soft beams are absorbed near the surface of the specimen and only the hard rays remain. This effect is called beam hardening. Cupping is one example for an artefact that results from beam hardening. The name was derived from its appearance as it is associated with a view into a cup as dense circular regions are brighter on the edge than in the centre of the object. Nowadays, there are also algebraic reconstruction techniques (ART) [4]. Those methods enable to handle beam hardening effects much better, but they are computational very expensive. Nevertheless, with increasing computing power, it is likely that those methods will get more common in future.

2.3 Image Processing

Methods described in the following are designed for processing volumetric images that are reconstructed from N_p x-ray projection images from the CT. The raw reconstructed image is a matrix $I(\mathbf{x})$ including an integer value for every point \mathbf{x} . Implementations of the methods were carried out in *MATLAB*, the *Insight Segmentation and Registration Toolkit (ITK)* and *ImageJ*.

MATLAB is a commercial tool by *MathWorks* for data analysis and algorithm development using a direct expression of matrices and arrays within a graphi-

cal user interface. It shows its advantages during debugging of new algorithms since all variables are easily accessible.

ITK is an open-source cross-platform system. It provides most of the common filters in a C++ development environment, where filters can be modified and connected in form of a pipeline structure [5]. Thus, new methods can be implemented easily and efficiently. Usually, *ITK* programs are designed for the use on the command line, but it can also be used with the Visualization Toolkit (VTK) [6] to develop a graphical user interface (GUI).

Composight is an open source project developed at IAM-WK [7] which includes most of the software introduced in this thesis. It provides small, problem-specific application for viewing, filtering and segmentation of volumetric data such as CT-scans. The implementation is based on *ITK*, *VTK* and *Qt*.

ImageJ is also an open-source software for scientific image analysis [8, 9]. It is written in Java and provides a GUI so effects of filters can be seen directly. Even distances, angles etc. can be measured using the inbuilt tools what is a great advantage for the validation of algorithms. *Fiji* [10] is basically the same programme as *ImageJ*, but it provides many useful plugins for 2D and 3D image processing initially.

2.3.1 Image Histogram

The image histogram is a crucial image feature derived from all grey values of an image without information about the location. It shows the number of appearances of a certain value y_i , where i stands for the grey value on the x -axis. Figure 2.4 shows an example for the histogram of an 8-bit grey-scale image. As it is bimodal, there are apparently two different phases in the image, where the left peak in the histogram results from a darker area and the right wide peak from a lighter area.

2.3.2 Fundamental Filters

Discrete Convolution

In order to apply filter masks to an image $I(x)$, the discrete convolution [11] can be utilized in the form

$$I'(x, y, z) = \sum_{x'=-L}^L \sum_{y'=-M}^M \sum_{z'=-N}^N h(x', y', z') I(x - x', y - y', z - z') \quad (2.4)$$

2 State of the Art

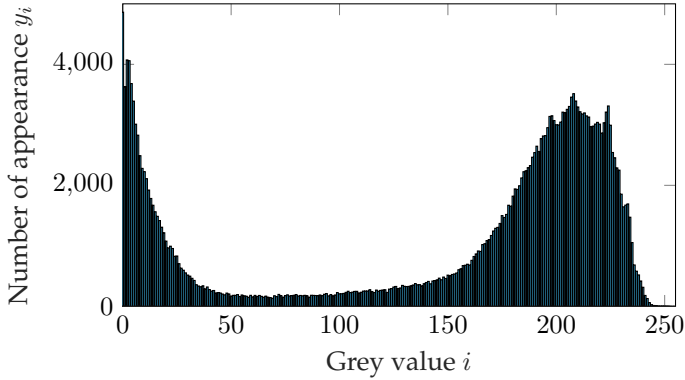


Figure 2.4: Bimodal histogram of a grey-scale image.

where $I'(x, y, z)$ is the filtered image and $h(x', y', z')$ is a discrete filter mask with a size of $(2L + 1) \times (2M + 1) \times (2N + 1)$. Common filters that can be implemented that way are e.g. the binomial filter or the Gaussian filter, where the latter one is the most common. The model using a filter mask may be good to illustrate how filters work in general, but they are relatively slow. Many filters, especially those that can be separated, can be implemented as recursive algorithm that processes the images line by line so that random accesses to the memory are unnecessary.

Gaussian Filter

The Gaussian filter is essential for most of the following image processing tools. For illustration, the filter is introduced as a simple filter mask with the Gaussian function

$$G(x) = \frac{1}{\sigma\sqrt{2\pi}} e^{-\frac{x^2}{2\sigma^2}} \quad (2.5)$$

for the one-dimensional case with the blurring parameter σ . The Gaussian filter can be applied to the image by creating a filter mask of certain size describing a Gaussian function in two or three dimensions and convolving this mask with the initial image I . The mask should be normed in order that the sum of all included values results in one. There are many implementations of recursive Gaussian filters available in open source projects, in this work we will use the *RecursiveGaussianImageFilter* from *ITK* [12, 13].

Image Gradient

The derivative of an image can be computed by a simple symmetric difference quotient. The partial derivatives for a two-dimensional image can easily be written as filter mask [11]

$$D_x = \frac{1}{2} [1 \quad 0 \quad -1] \quad ; \quad D_y = \frac{1}{2} \begin{bmatrix} 1 \\ 0 \\ -1 \end{bmatrix} \quad (2.6)$$

while the gradient of the 2D image on a certain point \mathbf{x} is

$$\text{grad}(I(\mathbf{x})) = \nabla(I(\mathbf{x})) = \begin{bmatrix} \frac{\partial I(\mathbf{x})}{\partial x} \\ \frac{\partial I(\mathbf{x})}{\partial y} \end{bmatrix} = \begin{bmatrix} D_x \\ D_y \end{bmatrix}. \quad (2.7)$$

Derivatives of higher order may be built respectively. For computational advantages, the derivative can be combined with the Gaussian blur filter. A recursive implementation *GradientRecursiveGaussianImageFilter* is already included in *ITK*.

2.3.3 Segmentation of Images

Global Threshold

The aim of the thresholding procedure is to find a grey value $0 \leq t \leq N_G$, which subdivides an image in two areas consisting of different materials without considering the location of those voxels. t is called the threshold and N_G is the maximum grey value depending on the data type of the image. Many methods have been developed in order to find a suitable global threshold for the segmentation of images either in 2D or even for volumetric images. *ImageJ* provides a couple of thresholding algorithms shown in this section. Niemistö gives a brief introduction for some of those thresholding techniques within the documentation [14] of his open source project *HistThresh toolbox* [15]. Also, the work of Glasbey from 1993 gives an overview of different thresholding techniques. In his work, the following partial sums are introduced for a better understanding of the different algorithms

$$A_j = \sum_{i=0}^j y_i, \quad B_j = \sum_{i=0}^j i y_i, \quad C_j = \sum_{i=0}^j i^2 y_i \quad (2.8)$$

2 State of the Art

where i is the grey value of the histogram on the x -axis and y_i is the number of occurrences of this value.

Iterative Selection Method: This method was developed by Ridler and Calvard in 1978 [16] and is the default method, also called IsoData, for global thresholding in *ImageJ*. A starting point for the threshold is chosen e.g. as the mean value of all pixels. Subsequently, all grey values higher and lower than the initial threshold are averaged separately. From those two mean values, the average is calculated and used as threshold for the next iteration. This procedure is repeated until the change of the fractions becomes smaller than a chosen residual value.

The **Method by Huang** [17] is based either on the Shannon's entropy or the Yager's measure to minimize the fuzziness of the input image. The implementation in *ImageJ* makes use of the Shannon's entropy. It is calculated as the absolute value of difference between the grey value at each point of the histogram and the average of the region where it belongs to. The threshold that minimizes this function is set as the global threshold. This method is particularly suitable for images with one sharp and another blurred peak in the histogram since it enables to account for the connected fuzzy region.

Intermodes was developed by Prewitt and Mendelsohn [18]. It requires a bimodal histogram which is filtered by a mean filter with a width of three iteratively until only two local maxima on the curve remain. Subsequently, the minimum value between those two maxima is used for segmentation. In *ImageJ*, this method is also called "Minimum".

MaxEntropy by Kapur et al. [19] is one out of several thresholding techniques based on the entropy. It makes use of the partial sums

$$E_j = \sum_{i=0}^j y_i \log(y_i) \quad \text{for } j = 0, 1, \dots, n \quad ; \quad n \leq N_G. \quad (2.9)$$

Subsequently,

$$\frac{E_j}{A_j} - \log(A_j) + \frac{E_n - E_j}{A_n - A_j} - \log(A_n - A_j) \quad (2.10)$$

is evaluated for each point where the maximum value is used as threshold t [20]. Other methods that are based on entropy measures are the **RenyiEntropy**, which works just like MaxEntropy but is based on the Renyi Entropy [19], which is an generalization of the Shannon's Entropy. Furthermore, **Shanbhag**

[21] implemented this method for bimodal histograms in 1994 which is a modified Version of Kapurs MaxEntropy. The method by Li from 1993 minimizes the cross entropy.

Mean is a simple thresholding method, which is included in the overview of Glasbey [20]. It uses the mean of the grey value distribution as threshold

$$t = \frac{B_n}{A_n}. \quad (2.11)$$

This algorithm will show its weakness for not taking the shape of the distribution of multiple modes in the histogram into account. Therefore, it does not perform well e.g. on bimodal histograms where one peak is significantly larger than the other one.

MinError(I) by Kittler and Illingworth [22] utilizes a Gaussian mixture model for determining the threshold t . Therefore, it is assumed that the grey values are distributed like a bimodal Gaussian distribution with different variances. The statistics are defined as

$$\begin{aligned} p_t &= \frac{A_t}{A_n}, & q_t &= \frac{A_n - A_t}{A_n}, \\ \mu_{t,1} &= \frac{B_t}{A_t}, & \mu_{t,2} &= \frac{B_n - B_t}{A_n - A_t}, \\ \sigma_{t,1}^2 &= \frac{C_t}{A_t} - \mu_{t,1}^2, & \sigma_{t,2}^2 &= \frac{C_n - C_t}{A_n - A_t} - \mu_{t,2}^2 \end{aligned} \quad (2.12)$$

and are used in the function

$$p_j \log \left(\frac{\sigma_{j,1}}{p_j} \right) + q_j \log \left(\frac{\sigma_{j,2}}{q_j} \right) \quad (2.13)$$

while the value j , that minimizes the result is used for the threshold t .

The **Moments** method was introduced by Tsai in 1985 [23]. It computes the grey-level moments of the input image and selects the threshold in a way that the moments of the thresholded image remain the same. Using the notation of Glasbey [20], the threshold is set to the grey value that is closest to x_0 , where

$$\begin{aligned} x_0 &= \frac{1}{2} - \frac{\frac{B_n}{A_n} + \frac{x_2}{2}}{\sqrt{x_2^2 - 4x_1}}, & x_1 &= \frac{B_n D_n - C_n^2}{A_n C_n - B_n^2} \\ x_2 &= \frac{B_n C_n - A_n D_n}{A_n C_n - B_n^2}, & D_n &= \sum_{i=0}^n i^3 y_i \end{aligned} \quad (2.14)$$

2 State of the Art

Otsu [24] defines the means of the grey values in two classes using

$$\mu_{t,1} = \frac{B_t}{A_t}, \mu_{t,2} = \frac{B_n - B_t}{A_n - A_t} \quad (2.15)$$

and the threshold is set to the value that maximizes

$$A_j(A_n - A_j)(\mu_{t,1} - \mu_{t,2})^2. \quad (2.16)$$

The variance between the classes are maximized while the variance in the class is minimized.

The **Percentile** method introduced by Doyle in 1962 [25] takes a known object fraction into account. As a standard method, the percentile is set to $p = 50\%$, so t is set to the value of j , where

$$p = \frac{A_j}{A_n - A_j} \cdot 100\%. \quad (2.17)$$

While this approach does not make sense for unknown object fractions, it can be helpful for the segmentation of images with known object fraction.

The **Triangle** method is a geometrical method by Zack et al. [26]. It was developed for histograms with a peak near to the upper or lower end of the histogram (Figure 2.5). From the peak value, a line is drawn to the other end of the histogram. The histogram is normed, so the maximum value in y is 1.0 just as the range from the peak to the end of the curve in x . The algorithm searches for a line that is perpendicular to the first one and touches the histogram with maximum distance. The corresponding value of i is used as threshold.

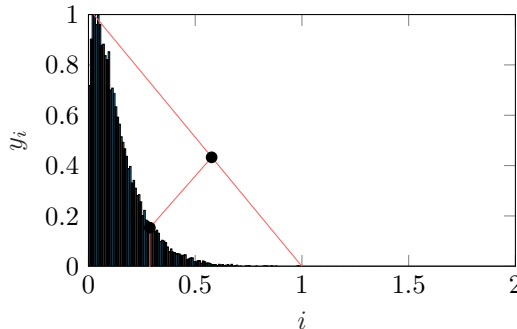


Figure 2.5: Graphical solution of the triangle thresholding technique.

2.3.4 Skeletonization

Skeletonization - also called binary thinning - refers to an image processing technique that reduces any kind of structure to their centrelines. The crucial idea of this method is to apply a symmetric erosion algorithm on a binary image iteratively until only the skeleton of the object remains [27]. Hanno Homann published an ITK based implementation of the thinning algorithm introduced by Lee et al. [28] in 2007. The same method was also transferred to the user friendly ImageJ plugin *Skeletonize3D* by Ignacio Arganda-Carreras in 2008 [29].

The algorithms of Lee [28] allows for a fast skeletonization of volumetric images by using an efficient decision tree structure instead of a simple lookup table. This method is much faster than conventional methods that make use of look-up tables for each configuration and enables to process volumetric images in a reasonable time. During the thinning procedure, the 26 neighbourhood of each voxel is taken into account in order to decide if the present point belongs to a surface and if it can be deleted or not.

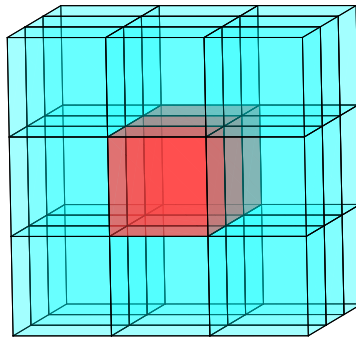


Figure 2.6: 26-neighbourhood of a voxel at a finished part of a skeleton (red).

This is an iterative procedure and is carried out repeatedly until the image does not change anymore and the data is finally skeletonized. Figure 2.6 shows the 26-neighbourhood of a skeletonized fibre. Lee et al. showed that the developed algorithm ensures the invariance of the Euler characteristic and thus, no holes are created in the structure during thinning.

Arganda-Carreras also implemented the ImageJ plugin *AnalyzeSkeleton* to analyse the resulting skeleton from the skeletonization. The plugin takes a skeletonized binary image as input. Since all lines have a thickness of only one

2 State of the Art

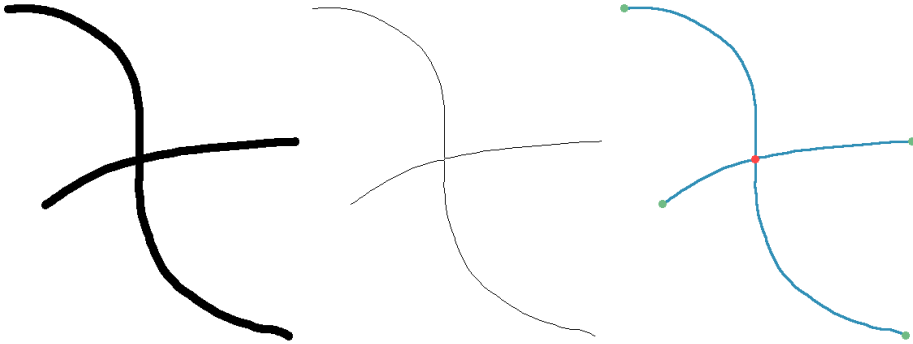


Figure 2.7: Example of a skeletonization in 2D. Left: Initial image drawn with a line thickness of 10 px. Middle: Image processed by the ImageJ skeletonization by Arganda-Carreras. Right: Result from the *AnalyzeSkeleton*-algorithm. End-points are illustrated in green, junction points in red and slab voxels in blue.

voxel, every voxel can be assigned to one of the following groups by observing the 26-neighbourhood of each point (cf. Figure 2.7 right):

- Slab voxels: All voxels with exactly two neighbours
- Junction voxels: Voxels with three and more neighbours
- End point voxels: Voxels with less than two neighbours

Based on this data, a network of branches, junctions and end-points is built for each independent skeleton and can be used for further analysis (see Fig. 2.8). Each branch consists of a certain number of slab voxels, depending on its length. Furthermore, each branch is connected to exactly two vertex voxels, where the branch is connected to a junction or an end-point. The junction class also includes those vertex points as well as the connected branches and the voxels that belong to the junction at hand since junctions can consist out of many voxels that have more than two neighbours. End-points only include a vertex voxel and the connected branch. Based on this graph, the results of the *AnalyzeSkeleton* plugin is created, which outputs e.g. the number of branches and junctions within a skeleton or the longest path throughout the skeletons.

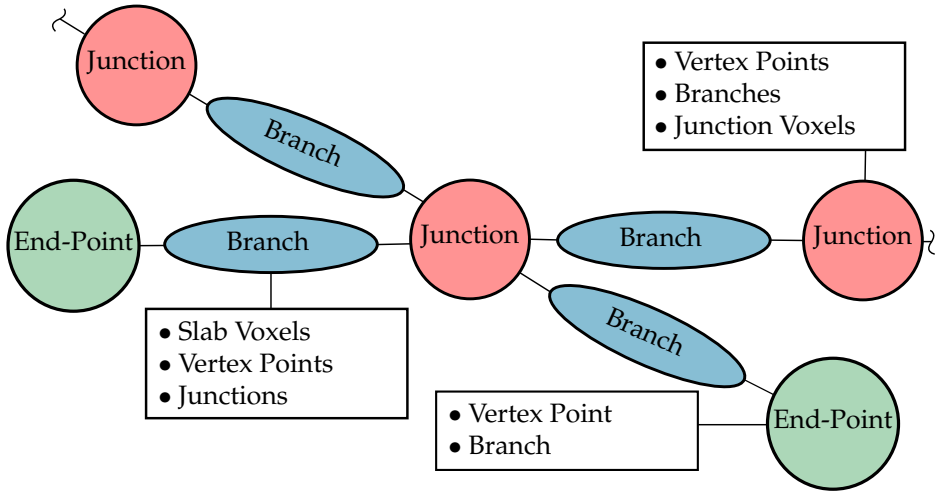


Figure 2.8: Exemplary graphical representation of a network that is built by the *AnalyzeSkeleton ImageJ* plugin from previously skeletonized data as shown in figure 2.7 [30].

2.4 Fibre Orientation Distribution

In the past decades, many methods for the determination of fibre orientations were developed and evaluated. As there was no opportunity to acquire high resolution volumetric images in the early days, some more or less simple approaches were used to calculate the orientation in fibre reinforced composites. In this work, we will concentrate on methods using image processing. But there are also ways to derive the FOD directly from physical characteristics like e.g. the absorption of polarized microwaves passing the material under different angles [31].

2.4.1 Methods for Orientation Determination from Microscopic Images

Stereology

The term Stereology refers to the study of measuring three-dimensional geometrical quantities from two-dimensional images [32]. Thereby, it is possible to derive even three-dimensional properties if the shape of the inclusions in the

2 State of the Art

material at hand is taken into account. As computed tomography was very restricted to the computational possibilities until the 1990s, stereology was a common way to extract information about the orientation from fibre reinforced polymers. There are many publications about orientation analysis from two-dimensional images. Underwood introduced procedures for the determination of 3D characteristics from two-dimensional images in 1972 [32]. Up from that point, stereology measures have been used in various publications [33, 34, 35] in order to derive orientation distributions from microscopic images. Fibre orientation is derived from a two-dimensional image plane through a fibre reinforced polymer. Figure 2.9 shows an image plane with a single fibre. The orientation can be calculated by the principal axes of the resulting ellipsoid, there the smaller value is the fibre radius. A common issue is, that the fibre orientation is not unique. A fibre with angle of (θ, ϕ) shows the same ellipsoid as with an angle of $(\theta, \phi + \pi)$. In 1996, the method was extended by Davidson in 1996 in order to derive real three-dimensional by grinding the sample down for a couple of μm and registration of the new image [36].

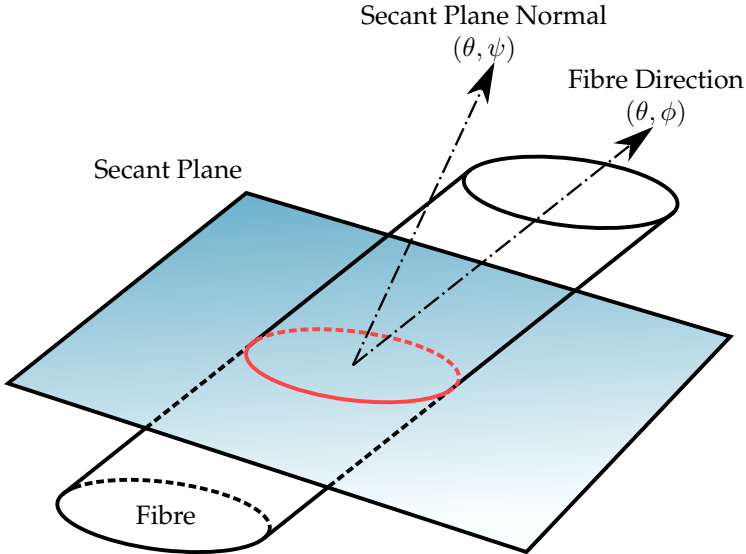


Figure 2.9: Cross section area of a secant plane through a fibre: Stereology makes use of the ellipsoidal cross-section to calculate the fibre orientation [35].

2.4.2 Voxel-based Methods from 3D Images

Anisotropic Gaussian Filter

The anisotropic Gaussian filter for orientation analysis was introduced by Robb et al. in 2007 [37] and extended by a new sampling method for discrete directions on the half-sphere by Wirjadi et al. in 2009 [38, 39]. The filter can be applied to binarized as well as to grey value images. It is based on an anisotropic Gaussian filter which is described by the kernel

$$G(\mathbf{x}) = \frac{1}{(2\pi)^{\frac{3}{2}} \det(\Sigma)^{\frac{1}{2}}} \exp\left(-\frac{1}{2}\mathbf{x}^t \Sigma^{-1} \mathbf{x}\right) \quad (2.18)$$

for three-dimensional data, where Σ is the covariance matrix

$$\Sigma = (\nu_{i,1} \quad \nu_{i,2} \quad \nu_{i,3}) \cdot \begin{pmatrix} \lambda_1 & 0 & 0 \\ 0 & \lambda_2 & 0 \\ 0 & 0 & \lambda_3 \end{pmatrix} \cdot \begin{pmatrix} \nu_{i,1} \\ \nu_{i,2} \\ \nu_{i,3} \end{pmatrix}. \quad (2.19)$$

The eigenvalues $\{\lambda_1, \lambda_2, \lambda_3\}$ of the covariance matrix define the actual shape of the filter. For the orientation analysis of fibres, it is recommended to be chosen to $\lambda_1 = \lambda_2 = \frac{1}{2}\lambda_3$ [38]. It results in a Gaussian filter mask that is isotropic in the $e_1 - e_2$ plane and twice as wide in e_3 -direction. The normed eigenvectors $\nu_i = \{\nu_1 \cdots \nu_n\}$ are given by n samples on a half-sphere, that are picked with respect to the sphere partitioning algorithm developed by Fliege and Maier in 1999 [40]. The multiplication with the eigenvector rotates the covariance matrix to a new coordinate system, defined by $\{e'_1, e'_2, e'_3\}$ where the Gaussian kernel G it is convoluted with the initial image $I(\mathbf{x})$ for all sampled orientations. Figure 2.10 depicts the principle of the filter. Since Fibre A is well aligned to the anisotropic Gaussian filter, it leads to a high filter response. Fibre B shows a high angular offset and results in a lower value. While calculating the filter response for each sample, the image is transferred to the orientation space

$$O(\mathbf{x}) = (r(\mathbf{x}), \mathbf{v}(\mathbf{x})). \quad (2.20)$$

In orientation space, only the highest filter response

$$r(\mathbf{x}) = \max_{\nu} [G * I](\mathbf{x}) \quad (2.21)$$

2 State of the Art

and its corresponding eigenvector

$$\mathbf{v}(\mathbf{x}) = \operatorname{argmax}_{\nu} [G * I](\mathbf{x}) \quad (2.22)$$

is saved as result during processing. Once the image is filtered with all orientations $\{\nu_1 \cdots \nu_n\}$, $\mathbf{v}(\mathbf{x})$ includes the eigenvector of the best corresponding orientation in each voxel of the image and can be used for further statistics like orientation tensors or histograms.

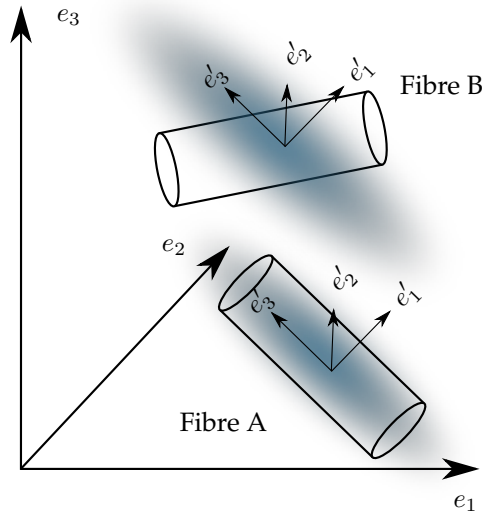


Figure 2.10: Principle of the orientation analysis using the anisotropic Gaussian Filter. The anisotropic Gaussian filter is rotated to a new coordinate system defined by $\{e'_1, e'_2, e'_3\}$. Fibre A is well aligned to the rotated Gaussian kernel and leads to a high filter response for the currently investigated orientation. Fibre B is badly aligned and leads to a lower response.

Hessian Matrix

In the case of image processing, the Hessian matrix is a square matrix of second order partial derivative of the present image $I(\mathbf{x})$. It was often used and discussed in the past century in order to detect valleys and ridges in topology what is of high interest for hydrology. Actually, the problem described e.g. by Rothe in 1915 [41] can be used in the same way for 2D image analysis. Elbischger et al. [42] introduced an algorithm for orientation analysis for 2D images and in 2006 Daniels et al. [43] implemented a method for the evaluation of local orientations in volumetric images based on the three-dimensional Hessian matrix

$$\mathbf{H}(\mathbf{x}) = \nabla^2 I_\sigma(\mathbf{x}) \hat{=} \begin{bmatrix} \frac{\partial^2 I_\sigma}{\partial x^2} & \frac{\partial^2 I_\sigma}{\partial x \partial y} & \frac{\partial^2 I_\sigma}{\partial x \partial z} \\ \frac{\partial^2 I_\sigma}{\partial y \partial x} & \frac{\partial^2 I_\sigma}{\partial y^2} & \frac{\partial^2 I_\sigma}{\partial y \partial z} \\ \frac{\partial^2 I_\sigma}{\partial z \partial x} & \frac{\partial^2 I_\sigma}{\partial z \partial y} & \frac{\partial^2 I_\sigma}{\partial z^2} \end{bmatrix}. \quad (2.23)$$

The Hessian matrix can be evaluated numerically in each voxel of the volumetric image, or every pixel in a 2D image, respectively. It is a measure of the local curvature of the image. It is important to keep in mind that in first place the curvature is not derived directly from geometrical objects within the image, but from the grey values. Figure 2.11 shows this circumstance on two simple examples of an one-dimensional line with grey values represented by a Gaussian function on the left. On the right, there is a two-dimensional image which is shown as a surface plot. It is derived from a line in order to imitate a fibre that is filtered by a Gaussian blur. In the one-dimensional case there is only one curvature κ . For a two-dimensional image, there are two curvatures κ_1 and κ_2 . An eigenanalysis of the Hessian matrix leads to the directions according to the principle curvatures at a local point. Using the eigenvector that corresponds to the smallest eigenvalue, the orientation of e.g. a fibre can be calculated since there is only a very small curvature along the fibres (see κ_1 in Figure 2.11). The method in 3D works analogous but can hardly be depicted since there are three principal curvatures. Generally speaking, the eigenvector to the smallest eigenvalue of the Hessian matrix results in a vector that points to the direction where the gradient of the grey values is the lowest. This direction corresponds to the fibre direction in volumetric images.

2 State of the Art

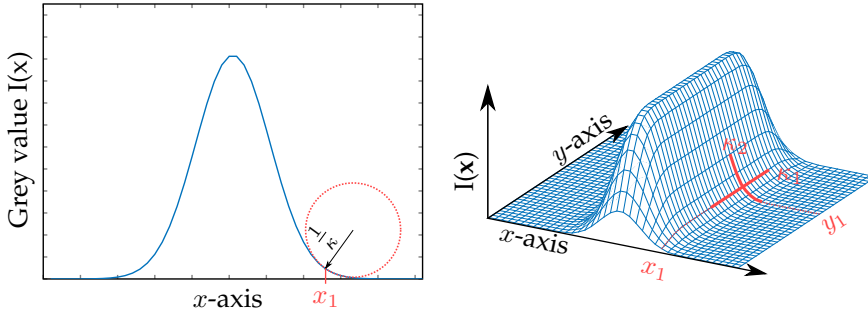


Figure 2.11: Curvature in an one-dimensional line (left) and a two-dimensional image (right). Red lines mark the curvatures of the grey values evaluated in a certain point in both examples. In 1D, there is only one curvature κ . For 2D images, the analysis leads to two curvatures κ_1, κ_2 , where the smaller one can be found in direction of the image structure.

Structure Tensor

Orientation analysis on three-dimensional images using the structure tensor is briefly described by van Ginkel [44]. Krause et al. utilized the method in 2010 in order to derive orientation data from CT images of fibre reinforced composites [45]. The structure tensor is derived from only the first derivative of an image. Figure 2.12 (a) depicts the gradients in a single cross-section of a plane and one fibre. All gradients point from the dark background in fibre direction. In a first step, the dyadic product of the image gradient with itself is evaluated in each voxel (Eq. 2.24).

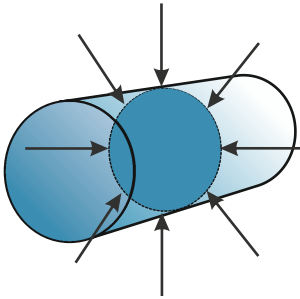
$$\nabla I_{\sigma}(\mathbf{x}) \otimes \nabla I_{\sigma}(\mathbf{x}) \hat{=} \begin{bmatrix} \left(\frac{\partial I_{\sigma}}{\partial x}\right)^2 & \frac{\partial I_{\sigma}}{\partial x} \frac{\partial I_{\sigma}}{\partial y} & \frac{\partial I_{\sigma}}{\partial x} \frac{\partial I_{\sigma}}{\partial z} \\ \frac{\partial I_{\sigma}}{\partial y} \frac{\partial I_{\sigma}}{\partial x} & \left(\frac{\partial I_{\sigma}}{\partial y}\right)^2 & \frac{\partial I_{\sigma}}{\partial y} \frac{\partial I_{\sigma}}{\partial z} \\ \frac{\partial I_{\sigma}}{\partial z} \frac{\partial I_{\sigma}}{\partial x} & \frac{\partial I_{\sigma}}{\partial z} \frac{\partial I_{\sigma}}{\partial y} & \left(\frac{\partial I_{\sigma}}{\partial z}\right)^2 \end{bmatrix} \quad (2.24)$$

As an eigenanalysis of $\nabla I_{\sigma}(\mathbf{x}) \otimes \nabla I_{\sigma}(\mathbf{x})$ always result $\lambda_1 = \lambda_2 = 0$ and $\lambda_3 > 0$, the tensor can be visualized as a line in Figure 2.12 (b). These tensors are blurred

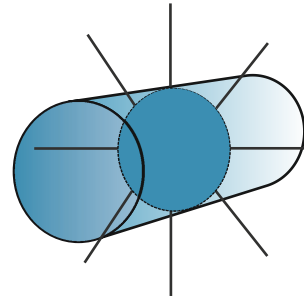
2.4 Fibre Orientation Distribution

with a Gaussian kernel with the blurring parameter ρ in order to receive the structure tensor

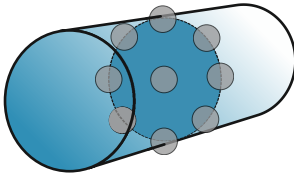
$$\mathbf{J}_\rho(\mathbf{x}) = G(\nabla I_\sigma(\mathbf{x}) \otimes \nabla I_\sigma(\mathbf{x}), \rho). \quad (2.25)$$



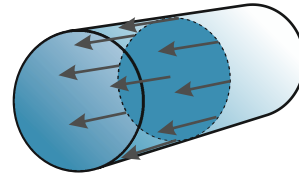
(a) Image gradients derived from scalar grey value image.



(b) Tensor resulting from dyadic product of gradient.



(c) Structure tensor: Blurred tensors within an image region.



(d) Orientations derived from averaged structure tensors.

Figure 2.12: Determining the fibre orientation using the structure tensor [46].

Since all the initial tensors are perpendicular to the surface of the fibre, the graphical representation of the averaged structure tensor will be planar in an idealized point of view (Figure 2.12 (c)). As one of the principal values of the

2 State of the Art

tensor is much smaller for fibrous structures, the local orientation can be calculated by applying an eigenanalysis. The eigenvector to the smallest eigenvalue describes the fibre orientation at a certain voxel. Figure 2.12 (d) shows the resulting orientation of the algorithm.

2.4.3 Statistical Descriptors of Orientation

In the previous section, methods for the extraction of the local orientation in CT images were described. For the sake of homogenisation of material properties like stiffness or thermal conductivity, it is necessary to build a statistic for a larger region of the material. This can be done either for each cell of a previously defined mesh or globally for the entire volume.

Orientation Histogram

A simple way to achieve a statistic of the orientation is to bin the orientation of each voxel to a certain class. This is easy for two-dimensional images since there is only one angle and bins can be allocated equidistantly on half of a circle. Note that orientations that are not included in $\{\phi \in \mathbb{R} \mid 0 \leq \phi < \pi\}$ are redundant and can be clustered to the opposing bin (Fig. 2.14 left). The same statistic for a three-dimensional histogram creates some difficulties since an equidistant partition on ϕ and θ does not result in surface patches of the same area on the unit sphere. Thus, it would be necessary to introduce weight factors related to its area for each field on the sphere. Another approach to this issue is a partitioning method that generates fields of equal area like the one introduced by Leopardi in 2006 [47]. It subdivides the sphere in N regions where two of them are the pole caps of the sphere and the remaining $N - 2$ fields are separated with rectilinear lines in spherical polar coordinates (see Fig. 2.13). Also, in this case, facing directions describe the same orientation and can be summarized. Actually, a histogram without redundancy include a half sphere without the negative area $y < 0$ of the x-y-plane and the negative x-axis, where $y = 0$. Obviously it is also possible to include another area of the x-y-plane as long as there is no redundancy (see Fig. 2.14).

Orientation Distribution Function

Another statistical description of orientations within a microstructure are orientation distribution functions (ODF). Since the ODF is a probability density function, the integral over all possible directions $\psi(\phi, \theta)$ has to be 1 as every voxel has any orientation [48]

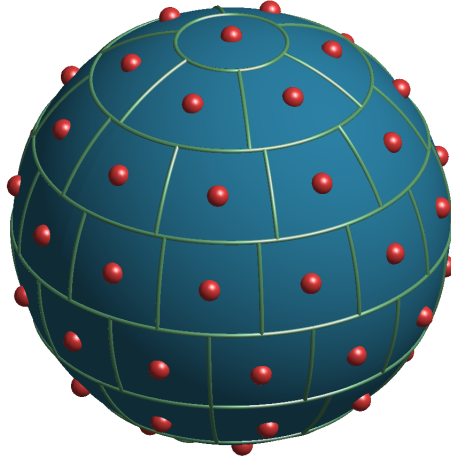


Figure 2.13: Partitioning of the sphere in 60 fields of equal area using the algorithm introduced and implemented by Leopardi [47].

$$\int_{\theta=0}^{\pi} \int_{\phi=0}^{2\pi} \sin(\theta) \psi(\phi, \theta) d\phi d\theta = \oint \psi(\mathbf{n}) d\mathbf{n} = 1. \quad (2.26)$$

A corresponding coordinate system including the unit vector \mathbf{n} is depicted in Figure 2.14. The ODF also has to be symmetric, because opposing directions lead to the same orientation:

$$\psi(\theta, \phi) = \psi(\pi - \theta, \phi + \pi) \quad (2.27)$$

or in euclidean coordinates

$$\psi(\mathbf{n}) = \psi(-\mathbf{n}). \quad (2.28)$$

Especially for fibre orientation distributions, many approaches have been developed in during the last decades. Mohaker et al. compared some of those functions for different material symmetries [49]. They showed that simple orientation distributions can be captured using the Mises-Fisher distribution [50], the Watson ODF [51], a singular kernel ODF [52] and the de la Vallee Poussin ODF [53]. If the orientation distribution gets more complicated, it is sufficient to approximate it by a sum of axially symmetric ODFs with different modal

2 State of the Art

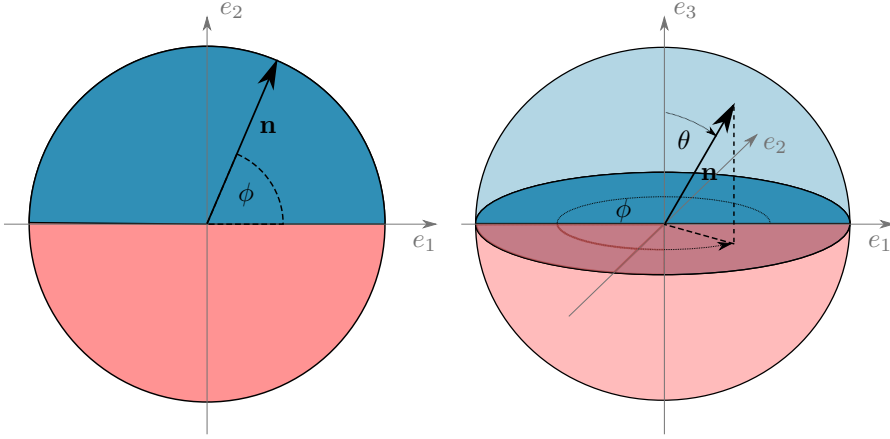


Figure 2.14: Definition of orientation angles in 2D and 3D. Blue areas and volumes are taken into account for the orientation distribution histogram while red areas are redundant due to the opposing directions.

vectors of one of functions mentioned before [49]. The fit of the resulting function can be carried out by an ordinary least-square fit e.g. on an orientation histogram.

Orientation Tensors

With respect to Advani and Tucker [48], orientation tensors can also be utilized to represent statistics about orientation data. They are often used to homogenise mechanical properties in a material. Hence, this work focusses on 2nd and 4th order tensors as those are of high interest for this purpose. The tensors can be derived from a known ODF as followed:

$$N_{ij} = \oint n_i n_j \psi(\mathbf{n}) \, d\mathbf{n} \quad (2.29)$$

$$N_{ijkl} = \oint n_i n_j n_k n_l \psi(\mathbf{n}) \, d\mathbf{n} \quad (2.30)$$

In case of discrete data like it is derived from CT images or two-dimensional images using stereological approaches, an empirical orientation tensor can be derived by

$$\mathbf{N} = \frac{1}{\sum_{i=1}^M w(i)} \sum_{i=1}^M w(i) \mathbf{n} \otimes \mathbf{n} \quad (2.31)$$

or

$$\mathbb{N} = \frac{1}{\sum_{i=1}^M w(i)} \sum_{i=1}^M w(i) \mathbf{n} \otimes \mathbf{n} \otimes \mathbf{n} \otimes \mathbf{n} \quad (2.32)$$

where M is the total number data points extracted from a region of interest. The factor $w(i)$ can be utilized in order to apply a different weight to each of the data points, otherwise it is set to one.

2.5 Fibre Length Distribution

The fibre length distributions (FLD) play an important role for mechanical models that include damage mechanisms. Just as for orientation distributions, it can be built in form of a histogram where fibres in defined intervals of length are summed up, or as an analytical function fit $f_l(L)$ that is normed to an integral value of one.

$$\int_0^{\infty} f_l(L) dL = 1 \quad (2.33)$$

A common density function for fibre length distributions is the two-parameter Weibull distribution [54, 55, 56, 57]

$$f_l(L) = \frac{m}{n} \left(\frac{L}{n}\right)^{m-1} \exp\left[-\left(\frac{L}{n}\right)^m\right]; L > 0, \quad (2.34)$$

where n and m are the scale and shape parameters and L is the fibre length. Figure 2.15 shows an exemplary fibre length histogram with the corresponding Weibull distribution.

2 State of the Art

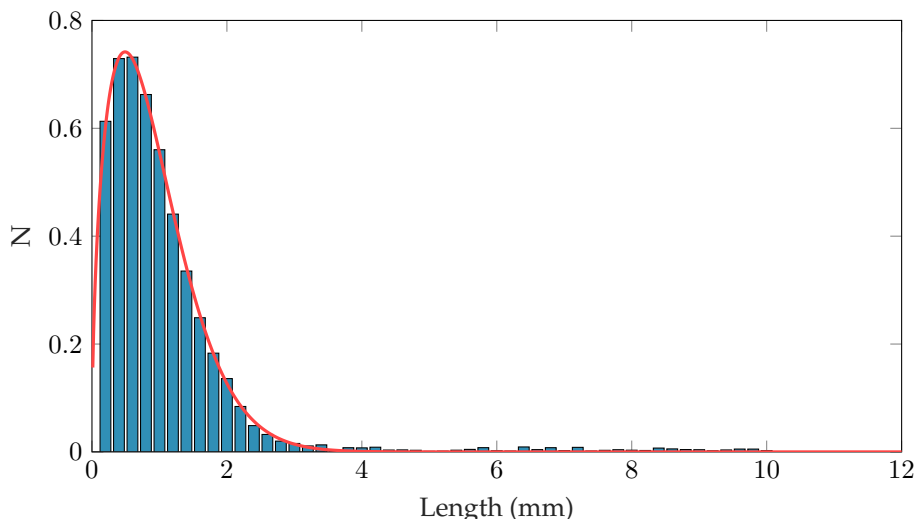


Figure 2.15: Weibull distribution. Blue: Discrete values, Red: Analytical distribution function.

2.5.1 Destructive Methods for FLD Determination

FLDs derived by destructive methods require for the incineration of the samples. When the material is heated up to a certain temperature, the polymer matrix is burnt while the glass or carbon fibres remain. Too high temperatures should be avoided since glass fibres can get sintered. Also, if the heat up is too abrupt, thermal stresses will occur on the fibres which can initiate fibre breakage. Thus, a temperature profile has to be adjusted for each material system in order to extract the fibres as carefully as possible. A standard procedure for sample incineration with the purpose of measuring the fibre or filler content is described in DIN EN ISO 1172 [58].

After incineration, the fibres have to be separated carefully. For that reason, both of the following commercial methods scan the fibres within a fluid as the preparation is gentler. The fibres from the incineration are given into a glass with water and some additives like surfactants and glycerine to improve the wetting of the fibres. Subsequently, the mixture is stirred carefully with a spoon or a stick. When the fibres are separated, a representative part of the mixture is given into another glass and diluted with water, so the density of fibres is lowered. This is done multiple times until the number of fibres is low enough

to be measured by the FASEP or FibreShape FiVer system and the mixture of fluid and fibres is given into a Petri dish.

FASEP

The FASEP system [59, 60] scans fibres in a Petri dish with a inner diameter of 90 mm. The real optical resolution of the scanner is 1700 dpi what is equal to a pixel size of $14.9 \mu\text{m}$. The fibre tracking is carried out by the ALF-algorithm, which is an in-house development of the FASEP company.

FiberShape FiVer

The sample preparation for measuring fibre lengths using the IST AG Fibre-Shape FiVer can be done similarly to the FASEP method. Both methods are almost similar except for the higher real optical resolution of $8 \mu\text{m}$ for the FiVer. Thus, fibres in a range from $10 \mu\text{m}$ up to 10 mm in diameter can be measured. Fibre lengths can range from $30 \mu\text{m}$ to 5 cm where the scanning area is 6 cm x 12 cm. The results are conform with ISO 9276-1 and ISO 13322.

2.5.2 Non-Destructive Fibre Length Distributions from CT Images using Fibre Tracking Approaches

Some algorithms for the determination of fibre lengths from CT images have already been developed in the recent past. In 2011, Salaberger et al. [61] introduced a method for the measurement of short fibre reinforced polymers. Despite the promising results for short fibre reinforced polymers, the algorithm does not account for curved fibres and is thus not suitable for long fibre reinforced polymers. The method developed by Teßmann et al. [62] tracks the centreline of fibres and treats curved fibres correctly. In the following section, the most important information about both algorithms is shown.

Method by Teßmann et al.

The method of Teßmann et al. [62] traces fibres directly from the grey value image. It accounts for the image gradient within the fibre and also takes the fibre diameter into account, which is almost constant for glass fibres. In a first pre-processing step, the original image is filtered by a morphological erode operator to enhance the dark spaces between the fibres. This procedure also enhances the contrast between fibre and matrix. But on the other hand, some fibres that

2 State of the Art

are very close will be merged. Supposedly, those fibres will be found in a later pass since the original picture will be processed repeatedly. For the detection of possible centre points of the fibres, a discrimination function developed by Frangi et al. [63] was used. It is based on the eigenvalues of the Hessian matrix, which was introduced for the sake of orientation analysis in section 2.4.2. After this, the actual fibre tracing algorithm is applied. As the fibre diameter is known, a cylinder approximation is used in order to trace along the fibres, starting from a potential fibre point from the previous step. Thereby, the direction derived from the Hessian matrix is used in order to find the next fibre point. Every fibre that was detected with this method is deleted in the initial image, so the algorithm runs until there are no more fibre-like structures left. Crossing fibres are treated by a maximum change in the angle during each step during tracing. Erroneously encountered gaps within the fibres are tried to resolve by a binary image that includes all the detected fibre points up to that point. If a traced fibre ends at a certain point and this point is already recognized as a fibre in this image, it is marked as a critical point. If critical points of two fibres match, it is assumed to be one fibre. The fibre length of fibre i is determined by the number of fibre voxels n_i and the voxel spacing s_i to

$$L_i = n_i s_i, \quad (2.35)$$

assuming that fibres are aligned to any axis.

Method by Salaberger et al.

Salaberger et al. showed two different concepts of their algorithm for the extraction of fibre lengths [61]. For improving the raw data in contrast and noise, an anisotropic diffusion filter was used.

Concept 1 starts with a segmentation of fibre material from the matrix. For reproducibility, they used the method by Otsu [24] - which is also described in section 2.3.3 - to derive a suitable grey value threshold without an influence of the user. Subsequently, binary thinning is applied to reduce all fibres to their medial axis [28]. A cluster analysis introduced by Pfeifer [64] is carried out, where Clusters are considered to be fibre voxels with more than two adjacent white voxels that are detected by a morphological operator. As a last step, the fibre tracing is applied. It uses the information of the cluster detection algorithm in order to follow fibres to its end or until a cluster is reached. Short branches below a certain length that do not end up in a cluster are considered to be noise from image acquisition. As all segments are processed, the clusters are analysed and the connecting fibres are re-assembled. Since the method was designed for short fibre reinforced polymers, which can be assumed to

be straight, it is sufficient to determine the start and endpoint of each fibre to derive the fibre length by the Euclidean distance

$$L_i = \sqrt{(\Delta x)^2 + (\Delta y)^2 + (\Delta z)^2}, \quad (2.36)$$

where Δ is the difference between start and endpoint of the fibre.

The second concept considered works on grey value images and there is no need of a binarization. The initial image is processed similar to the method by Teßmann using the eigenvalues of the Hessian matrix. In every fibre point, the grey values within a plane perpendicular to the fibre orientation are taken into account. In an ideal case, those should show a peak in the middle of the fibre. Thus, these points are set in a resulting binary image.

The applicability of this algorithm for short fibre reinforced polymers was proven in another publication by Salaberger et al. [65] using different image resolutions from $1 \mu\text{m}$ to $3 \mu\text{m}$. Scans with a voxel size of $1 \mu\text{m}$ and $2 \mu\text{m}$ delivered almost exact results while scans with $3 \mu\text{m}$ decreased the mean value from originally $195.2 \mu\text{m}$ to $178.4 \mu\text{m}$.

2.6 Fibre Volume Content

2.6.1 Specimen Incineration

A destructive method for the purpose of characterising fibre volume contents is the incineration of the polymer matrix. Therefore, samples are heated up in small ceramic melting pots, where the matrix material is burned off and only the fibre material remains. The weight of the full sample and of the remaining fibre material can be measured using a high precision scale. The fibre content by weight is derived directly from those measured values

$$c_{w,f} = \frac{w_f}{w_{tot}} \quad (2.37)$$

where w_f is the weight of the fibres and w_{tot} is the total weight of the sample. Including the density of the constituents and the fact that the weight of the polymer is $w_m = w_{tot} - w_f$, the fibre volume content is given by [66]

$$c_{v,f} = \frac{\frac{w_f}{\rho_f}}{\frac{w_f}{\rho_f} + \frac{w_m}{\rho_m}}. \quad (2.38)$$

2.6.2 Principle of Archimedes

In "An introduction to composite materials" by Hull and Clyne [67], a method for the determination of porosity within composites was described using the principle of Archimedes. Therefore, the density of the composite has to be known exactly. The same approach can be made for the fibre volume fraction in absence of pores. As the volume and the density of a specimen can be measured using Archimedes' principle, the fibre weight content can be calculated through

$$c_{w,f} = \frac{\rho_c - \rho_m}{\rho_f - \rho_m}, \quad (2.39)$$

where ρ_f and ρ_m are the densities for of the fibres and the matrix and ρ_c is the density of the composite measured using Archimedes' principle.

2.6.3 X-Ray based Methods

Volumetric Images

Measuring fibre volume content from volumetric images is a great challenge due to image blur. Using a grey value threshold for separation, the fibre volume content can be "adjusted" in a wide range by choosing a higher or lower value. In general, it is possible to use all of the thresholding techniques described in section 2.3.3 for the segmentation of an image. But effects like beam hardening can influence the image dependent on the arrangement of the fibres so the methods do not necessarily work for all images acquired with the same parameters.

Projection Images

In [68], a method for the use of X-ray projection images has been developed for the purpose of in-line measurement of the local fibre content of SMC material in a production line. A support vector regression (SVR) was utilized using a dataset derived from 17 samples. Those samples were combined in stacks of two with all possible permutations what results in a ground truth of 153 samples. The fibre volume content of the samples was measured subsequently by incineration. The feature space was chosen to the attenuation path length (APL) and the relative attenuation

$$R_{\mu}(\mathbf{x}) = -\ln \frac{I_D(\mathbf{x})}{I_0(\mathbf{x})} \quad (2.40)$$

in a certain point or region. Applying the law of Lambert-Beer (eq. 2.2), the attenuation should be linear with the APL in a logarithmic diagram. But as there are effects like beam hardening, the values are no longer linear dependent. For that reason, a SVR was trained in order to fit a hyperplane which links the feature space to a certain fibre volume content. After training, the maximum error in fibre volume content using optimal parameters was 0.44 vol % for planar specimen. Further tests with a corrugated sample resulted in an error of up to 4 vol % in areas where the penetration length was high. However, the SVR has not been trained with specimen of a thickness up to that point so it is likely that the method can be improved if the reference plates are adjusted to the range of the penetration lengths that appear with the sample shape of interest.

2.7 Porosity and Inclusion Analysis

2.7.1 Descriptors for Morphology

Measures in order to describe the shape of pores are frequently used for the characterization of foam structures. Elmoutaouakkil et al [69] introduced a couple of descriptors for porous structures that can also be used for the sake of characterizing pores in polymer structures. For this reason, the following descriptors are of interest:

- **Number of Pores**
- **Surface S**
- **Volume V**
- **Sphericity:**
 $SP = 6V \sqrt{\frac{\pi}{S^3}}$, gets equal to 1 for spherical pores
- **Morphological Factor F :**
 is derived from the eigenvalues of a 3D inertia matrix that is determined for a certain pore. The higher the ratio of the eigenvalues, the higher is the elongation of a pore.

Lin and Miller [70] determined the sphericity of particles in volumetric images by sampling a triangular mesh on the surface of each particle. They employed the marching cubes algorithm [71] for improving of the extracted surface and thereby the results of the sphericity.

2.7.2 Surface Curvature

Despite the descriptors above, also local curvature information of pores can be extracted. Therefore, the image has to be binarized in order to recognize the edges of objects properly. Note that the algorithms will result in an erroneously curvature for an incorrect segmentation since the object will appear eroded or dilated. For two-dimensional images there is only one curvature, while two principal curvatures can be derived from a three-dimensional image (Figure 2.16).

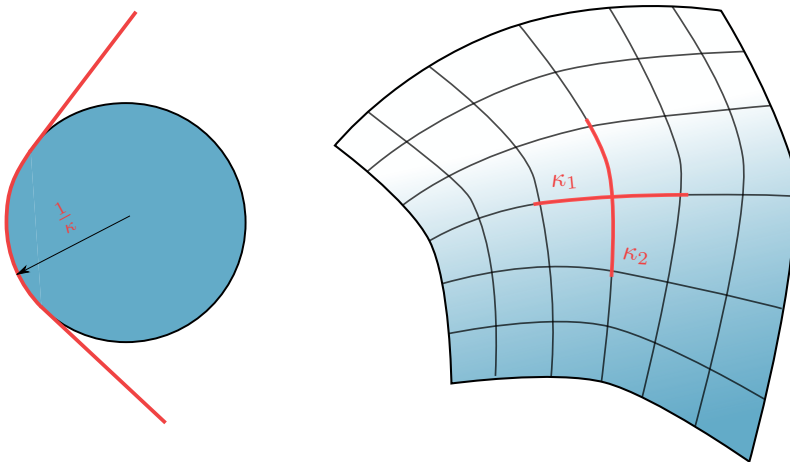


Figure 2.16: Curvature on 2D and 3D structures.

From those principle curvatures for the three-dimensional case, some scalar curvature measures can be derived:

- **Gaussian Curvature** is the product of both principal curvatures in 3D. As one of the principal curvatures is zero, also the Gaussian curvature gets zero.

$$\kappa_G = \kappa_1 \cdot \kappa_2 \quad (2.41)$$

- **Mean Curvature** is the average of the principal curvatures

$$\kappa_M = \frac{1}{2}(\kappa_1 + \kappa_2). \quad (2.42)$$

- **Max Curvature** is the highest of the principal curvatures

$$\kappa_{max} = \max(\{\kappa_1, \kappa_2\}) \quad (2.43)$$

- **Min Curvature** is the lowest of the principal curvatures

$$\kappa_{min} = \min(\{\kappa_1, \kappa_2\}) \quad (2.44)$$

In order to derive the surface curvatures from surface voxels in CT images, we will investigate two different approaches. The first one is named the "patch-based method" since it runs on a specified surface patch of the local structure. The second method is called the "Hessian-based method" as the curvature is derived directly from the Hessian matrix. Therefore, some definitions from differential geometry are needed. A mathematical surface S^2 in three-dimensional space is a two-dimensional regular submanifold of \mathbb{R}^3 [72]. This surface can also be described by a normal vector field in \mathbb{R}^3 , where every surface normal has its origin on a surface point $p \in S$ and has the unit length. Those normal vectors are expressed in a local coordinate system F with the Normal vector \mathbf{n}_s and two perpendicular tangent vectors \mathbf{t}_1 and \mathbf{t}_2 .

$$F = \{\mathbf{n}_s, \mathbf{t}_1 = \frac{\mathbf{n}_{s\perp}}{\|\mathbf{n}_{s\perp}\|}, \mathbf{t}_2 = \mathbf{n}_s \times \mathbf{t}_1\} \quad (2.45)$$

Note that the local coordinate system does not have to be aligned to the principal curvatures of the surface. The Gaussian map, which takes part in both of the following methods, makes use of the local vector field around a given point as the change of those vectors is directly related to the curvature at a given point [73].

Patch-based Method

This approach is implemented in the *Advanced Normalization Tools (ANTs)* [74] and is based on the original paper of Avants and Gee from 2003 [73]. For the evaluation, a patch size has to be chosen that specifies the radius of the local neighbourhood taken into account at each voxel. In the *ANTs* implementation, this parameter is called σ [75] for the command line tool. Using the Gaussian map in the local frame, the derivative of the normal vector $\mathbf{n}_{s,u}$ in u-direction, which is perpendicular to \mathbf{n}_s - just like $\mathbf{n}_{s,v}$ in v-direction - can be written as a linear combination of the tangent vectors \mathbf{t}_1 and \mathbf{t}_2 :

$$\mathbf{n}_{s,u} = a\mathbf{t}_1 + c\mathbf{t}_2 \quad (2.46)$$

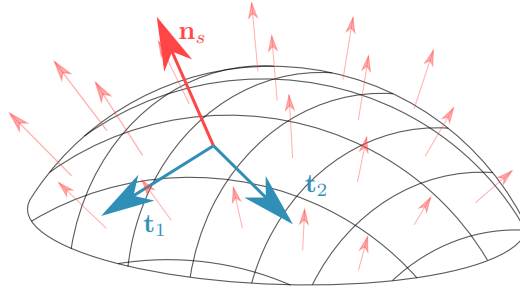


Figure 2.17: Illustration of Gauss map. \mathbf{n} shows the normal vector to the surface of an object for a certain point, where the Gaussian map is evaluated. \mathbf{t}_1 and \mathbf{t}_2 illustrate the vectors of the corresponding plane where the surface normal vectors derived from the image gradient in a certain region are mapped to.

$$\mathbf{n}_{s,v} = b\mathbf{t}_1 + d\mathbf{t}_2 \quad (2.47)$$

The Jacobian of $d\mathbf{n}_s(p)$ in the local coordinates u and v leads to the shape operator S

$$\mathbf{S} = \begin{bmatrix} a_s & c_s \\ b_s & d_s \end{bmatrix} \quad (2.48)$$

with the coefficients a_s, b_s, c_s, d_s , where the local curvatures can be derived from the eigenvalues of S and the principal directions from its eigenvectors.

Hessian-based Method

The implementation of this method is based on Hughes publication "Differential Geometry of Implicit Surfaces in 3-Space - a Primer" [76], where he worked out a recapitulation of Dombrowskis work from 1968 [77]. It was proven that the surface curvature can be derived directly from a function that is defined in \mathbb{R}^3 , what enables to process volumetric images directly without using the Gaussian map on local surface patches. Nevertheless, the shape operator - also called "Weingarten map" in the Hughes work - was also used for the derivation of the following formulas. It was shown that the shape operator is independent

2.8 Application in Homogenisation of Mechanical Properties

of the path that was chosen on the surface. Therefore, we can also choose an arbitrary orthonormal basis for the local tangents to calculate the eigenvalues from the shape operator in matrix form

$$\mathbf{S} = \frac{1}{\|\nabla I(\mathbf{p})\|} \begin{bmatrix} \mathbf{t}_1^t \mathbf{H}(\mathbf{p}) \mathbf{t}_1 & \mathbf{t}_1^t \mathbf{H}(\mathbf{p}) \mathbf{t}_2 \\ \mathbf{t}_2^t \mathbf{H}(\mathbf{p}) \mathbf{t}_1 & \mathbf{t}_2^t \mathbf{H}(\mathbf{p}) \mathbf{t}_2 \end{bmatrix}. \quad (2.49)$$

The point \mathbf{p} refers to all points on \mathbb{R}^3 , where $\|\nabla I(\mathbf{p})\| > 0$. In case of a binarized image, those are only points at the surface of an object. A detailed description of the Gaussian map and the shape operator can be found in "Differential geometry" by Tu [72].

2.8 Application in Homogenisation of Mechanical Properties

A statistical description of the fibre orientation distribution is indispensable for an accurate mechanical model of long fibre reinforced polymers.

Using discrete fibre orientations \mathbf{n}_α , homogenisation methods can be applied to predict the homogenised effective stiffness tensor $\bar{\mathbb{C}}$ depending on the fibre material parameters p_f and the matrix material parameters p_m

$$\bar{\mathbb{C}} = \mathbb{f}(p_f, p_m, \mathbf{n}_\alpha). \quad (2.50)$$

Herein, p_f and p_m contain additional information, such as volume fraction, stiffness of both constituents and the aspect ratio of the fibres. Orientation histograms (cf. Sec. 2.4.3) can be utilized to calculate effective material properties for a pseudo grain model. For this purpose, the considered domain is divided into subdomains containing fibres of a certain orientation. The resulting subdomains can be described by a pseudo-grain model. The advantage of such an approach is to directly use a histogram for a certain orientation where the volume percentage represents the fraction of a pseudo-grain domain within the subdivided microstructure. Based on this, the elastic stiffness can be predicted using e.g. the functionally graded interface model [78]. Effective thermoelastic properties can be derived by the self-consistent scheme (SC), the interaction direct derivative or a Hashin-Shtrikman based two-step method [79, 80]. Furthermore, the effective material properties can be determined by the fibre orientation distribution function $\psi(\mathbf{n})$

$$\bar{\mathbb{C}} = \mathbb{f}(p_f, p_m, \psi(\mathbf{n})). \quad (2.51)$$

2 State of the Art

Orientation distribution functions can be obtained from fibre orientation tensors and combined with the SC and the IDD method [81, 82] for a prediction of the mechanical properties. Other homogenisation schemes, like the Mori-Tanaka method [83] allow for the direct use of orientation tensors. Consequently, the effective stiffness is calculated by

$$\bar{\mathbb{C}} = \mathbb{f}(p_f, p_m, \mathbb{N}, \mathbb{N}), \quad (2.52)$$

using the empirical fibre orientation tensors of second and fourth order \mathbb{N} and \mathbb{N} derived from volumetric images (cf. Sec. 2.4.3). The main advantage of using fourth order tensors directly from CT data is that it is not necessary to make further assumptions regarding closure approximations which influence the orientation distribution. Brylka et al. [84] showed that e.g. the invariant-based closure approximation (IBOF) [85] can lead to deviations in predicted stiffness compared to the direct use of fourth-order orientation tensors. Herein, for a 30 wt% glass fibre reinforced polypropylene composite the deviations in predicted stiffness range up to 9.6 %.

2.9 Research Questions

Recent publications introduced within this chapter seem to be applicable for the determination of local fibre orientations. Thus, the three introduced algorithms based on an anisotropic Gaussian filter, the Hessian matrix and the structure tensor are investigated and evaluated. Therefore, artificial microstructures have to be used as well as real CT-scans of materials with known FOD in order to investigate the accuracy of those methods. Finally, the best performing algorithm can be used to evaluate continuous-discontinuous long fibre reinforced materials to prove the applicability on materials of interest. For the estimation of the accuracy of common image thresholding tools for the determination of fibre volume fractions, available algorithms should be applied and compared with values examined by conventional methods using specimen incineration. Today, the standard procedure for the evaluation of FLDs is still the optical measurement combined with sample incineration since available methods are not accessible or they work only on straight fibres. Determinating FLDs by a non-destructive method enables e.g. for the validation of fracture models using in-situ CT tests. Therefore, a fibre tracking algorithm has to be implemented and applied on long fibre reinforced material. For validation of this method, it has to be compared with conventional destructive optical methods. Using the same data, fibre curvatures can be derived from spatial curves while the results have to be validated manually due to the lack of an alternative method. While the FLD of SMC material is known initially from the manufacturing process, the

2.9 Research Questions

fibre curvature is an interesting characteristic of this material system. Surface curvatures of pores can be useful for the detection of potential notches within fibre materials as those spots have a high curvature. Applying the same method on fibres, it is possible to determine the fibre ends. For a precise determination of curvatures from volumetric images, both of the introduced methods for the evaluation of surface curvatures based on the Hessian matrix and the fit of a surface patch have to be compared on artificial volumetric images and real structures of known curvature in order to find a fast and precise solution.

3 Material



Figure 3.1: GRK 2078 Material. From bottom to top: Continuous carbon fibre SMC, discontinuous glass fibre SMC, hybrid material made of both bulk composites in a sandwich-design with the carbon fibre SMC on the shell and the glass fibre SMC in the core.

All of the methods for microstructure characterization in the following are developed in order to investigate CoDiCo materials consisting of long fibre reinforced polymers (LFRP). For continuous fibre reinforcements, the fibre length and orientation are generally known, but pores that appear between layers are of high scientific interest. Discontinuous fibre reinforcements show a locally varying orientation distribution that depends on the flow conditions in the manufacturing process which can be derived from CT-scans. Figure 3.1 illustrates some of the material systems investigated during the first generation of the GRK 2078. It shows a continuous carbon fibre (CF) reinforced plaque on the bottom, a discontinuous glass fibre (GF) reinforced SMC in the middle and a hybrid material made of a combination of both of them on top. For hybrid materials, the position of interface between the bulk composites can be determined from CT-images.

3.1 Long Fibre Reinforced Polymers (LFRP)

3.1.1 Sheet Moulding Compounds

The term sheet moulding compound (SMC) refers to the sheet-shaped semi-finished product in the production chain. Those sheets are produced continuously on a compounding machine, where chopped fibres fall on a film of uncured matrix material - also called the paste - that is applied on a thin polymer foil. Cutting of the fibres is carried out in a chopper consisting of blades on a roll that specifies the length of fibres. Subsequently, another foil with paste is applied on the top of the dry fibres, forming a laminate of two plies of paste and one ply of fibres that is calendered to induce the compaction, impregnation and the wetting of the fibres. The resulting sheet is rolled on a coil and matured for a specific period of time until it gets a leather-like, workable texture [86].

The final product is produced by compression moulding of the SMC. The sheets are cut into pieces and fitted into the mould after removing the transport foil. Thereby, the entire mould can be covered so the material does not flow during pressing. This avoids the rearrangement of the fibres and the orientation distribution is assumed to be almost planar isotropic. Usually, the SMC is put onto a smaller region within the mould, the material will flow and the fibre orientation in the resulting part will be dependent on the material flow. This flow is also beneficial for a low porosity as air pockets can leak during this process.

In microstructure characterization, the orientation analysis on SMC is most important for material that flowed during compression moulding. The FLD of SMC material can be assumed to be known because fibres appear typically in bundles that rarely break during the entire manufacturing process. This fact justifies to use the fibre length set up in the fibre chopper as the approximated fibre length. Pore analysis can be interesting for SMC materials especially for non-flow material where the manufacturing process is not optimized very well.

Discontinuous GF SMC

Glass fibre reinforcements are most common in the SMC process. Usually, those material systems are used in automotive industry including chalk filler material to receive class A surfaces but a lower strength. The GRK 2078 aims to develop an SMC material for structural parts, so the paste does not include fillers resulting in a worse surface quality. Fibres are usually not separated in SMC and remain as bundles in the finished parts.

3.1 Long Fibre Reinforced Polymers (LFRP)

In CT-scans the fibres show a good visibility due to a high contrast in density compared with the polymer matrix. On the other hand, pores are hardly visible in a GF-composite. The visibility is not only dependent on the difference in density, but also on the fibre architecture. Due to various CT artefacts, shadows show up in less dense regions that are surrounded by dense objects. Figure 3.2 illustrates this issue on a woven glass fibre material. The pores in the dark area between the fibre bundles have a very low contrast while the fibres can be seen clearly.

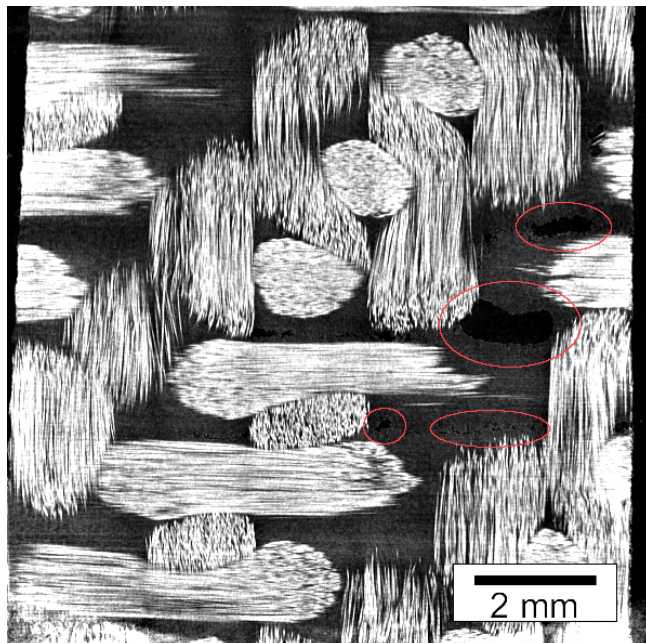


Figure 3.2: CT scan of a woven glass fibre reinforced material with pores. Glass fibres have a good visibility while the contrast of the pores (marked by red circles) is very low.

The latter image is only for demonstration as there are no pores in the GF SMC at hand. Nevertheless, the same effect can be expected for the GF SMC as the fibres are bundled and thus there are shadowed areas between those bundles (Figure 3.3). The matrix material is an unsaturated polyester polyurethane resin (UPPH) from Aliancys and the glass fibres for the DiCo GF SMC came from Johns Manville under the name GF Multistar 272.

3 Material

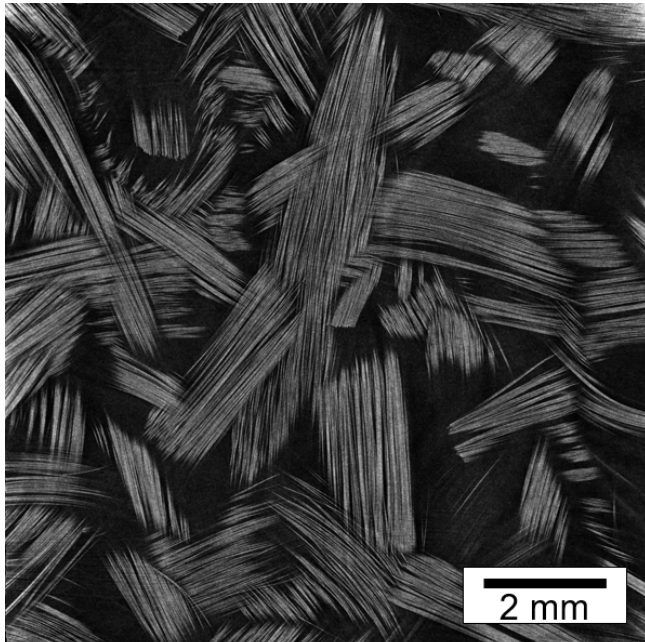


Figure 3.3: CT scan of a glass fibre reinforced SMC.

Discontinuous CF SMC

Production of carbon fibre reinforced SMC corresponds widely to the GF SMC process in the previous section. The matrix material is a UPPH-resin and the fibres are called "Panex 35" from Zoltek. Orientation analysis in CT images is a challenging problem as the contrast between fibres and matrix is very low. Figure 3.4 shows an carbon fibre reinforced SMC. The grey value of matrix material and fibres is almost the same, but the orientation is still visible to the naked eye. It is also apparent that there are no pores within the material since they would be highly visible as it can be seen in Figure 3.10.

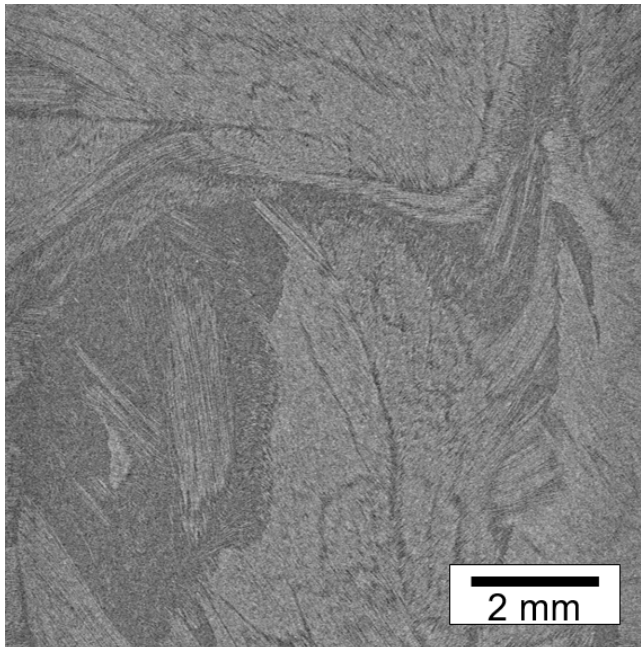


Figure 3.4: CT scan of a carbon fibre SMC. Carbon fibres can not be separated but the orientation can be seen.

Continuous CF SMC

Manufacturing of continuous carbon fibre reinforced polymer in a SMC process is atypical but combined with other materials it enables to produce complex parts with high stiffness and strength. The basis of the constituents is

3 Material

almost similar to those of DiCo CF SMC but with a slight adaption of the matrix material to match the requirements of the new manufacturing process. The production of the semi-finished product is different from the classic method. Here, it was produced on a laboratory scale production line using a special B-stage resin that is heated up using heating plates at the end of the line [87]. This enables to cure the resin to the first of two steps and thus to get a workable but flexible sheet that can be inserted to the mould just like a common SMC material. Bulk continuous carbon fibre reinforced plaques are produced by covering the entire mould with the semi-finished sheets to avoid material flow eventually resulting misalignments of the continuous fibres.

Figure 3.10 shows an example for a carbon fibre layup with pores. The image quality is comparable to the CF SMC: The contrast between fibre and matrix is low but the orientation is visible and pores show a high contrast.

3.1.2 Long Fibre Reinforced Thermoplastic

The most significant difference of long fibre reinforced thermoplastics (LFT) to the SMC material is the thermoplastic matrix material. Therefore, the manufacturing process of the semi-finished product is quite different. The previously compounded polymer matrix is mixed with the glass fibres straight from the bobbin with in an twin-screw extruder [88]. The fibres are shortened just by kneading in the extruder. The material mixture is extruded and cut to a specific size corresponding to the volume of the building component, which is called the plastificate. This semi-finished product can be processed just like the SMC material in a compression flow moulding process. The initial fibre orientation shows a more complicated distribution due to the kneading in the extruder. Usually, all the fibres are separated and bundles are not present. Thus, the fibre curvature is higher due to the reduced bending stiffness of the single fibres. The fibre length distribution not that sharp as it is in SMC material because the fibres are broken randomly in the extruder. Figure 3.5 shows a slice through a glass fibre reinforced LFT material. The primary LFT material in this thesis is made of a PP matrix with 10, 20 and 30 wt % glass fibres of type TufRov 4575.

3.1.3 Overview LFRP

All long fibre reinforced materials are listed in Table 3.1 for a better overview throughout this thesis.

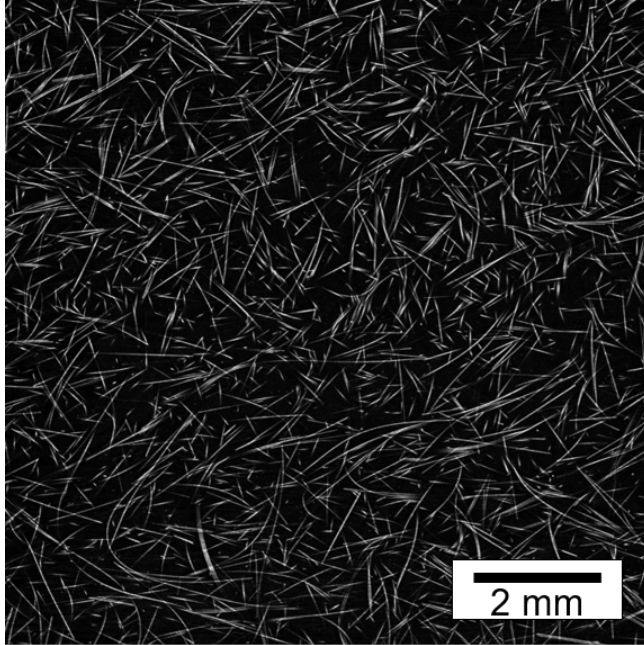


Figure 3.5: CT scan of a glass fibre reinforced LFT material. Fibres have a high contrast to the matrix and the curvature of the fibres is clearly noticeable.

Table 3.1: Primary continuous and discontinuous fibre reinforced materials

Material system	Matrix system	Fibre material	approx. fibre weight content (%)	Fibre length (mm)
DiCo GF SMC	UPPH	GF	41	25.4
DiCo CF SMC	UPPH	CF	55	25.4
Co CF	UPPH	CF	60	-
LFT	PP	GF	{10,20,30}	unknown

3.2 Validation Materials

Even though the aim of this thesis is to characterize CoDiCo LFRP material, which is described within this chapter, in many cases it makes sense to test

3 Material

and validate methods with other material systems. E.g. for orientation analysis tasks, a known FOD is beneficial for validation which is not available for the material at hand. In other cases, like for the fibre tracking method, it is not possible to process the necessary specimen size due to limited computational capabilities. Hence, the fibre length distribution of LFRPs cannot be evaluated, but the fibre tracking algorithm can still be used to determine fibre curvatures. As the X-Ray absorption is almost constant throughout most polymers, the matrix material is not a major concern. Even thermosets and thermoplastics are not distinguishable from the reconstructed image. On the contrary, the fibre material - carbon or glass - influences the contrast within the image significantly. This circumstance justifies the use of alternate materials for the purpose of validation.

3.2.1 Fibre Orientation Distributions

For validation of orientation analysis methods, a physical material with known orientation distribution is needed. Thus, two different Material system including carbon fibres and glass fibres are used for validation in the following.

3D-Printed Specimen

The first material is a 3D printed glass fibre reinforced ABS matrix with a fibre content of 10 wt % [89]. Figure 3.7 (left) shows the high contrast between glass and polymer. Thus, the fibres can be separated easily. The fused deposition modelling (FDM) process, which was used for manufacturing, affects the fibres to be highly aligned to the printing path. A sample was produced with a printing path aligned to the 0° direction (see Fig. 3.6) provoking a sharp fibre orientation distribution.

Pultruded Carbon Fibre Rod

The second real image or validation of orientation analysis methods (Figure 3.7 (right)) shows the microstructure of a carbon fibre reinforced pultrusion rod. The matrix material is epoxy, which contains four carbon fibre rovings which consist of 1200 fibres each. The rod diameter is 4 mm. Carbon fibres show very low contrast to the polymer and cannot be separated individually.

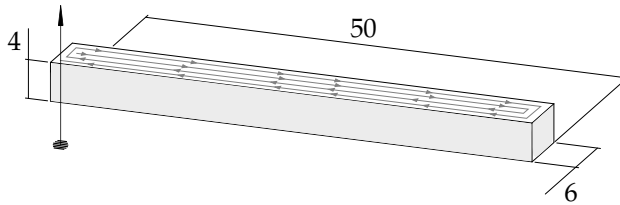


Figure 3.6: 3D-printed GF reinforced sample. The in-plane printing path is shown by the lines on top of the sample. The arrow on the left illustrates the stacking direction of the single layers.

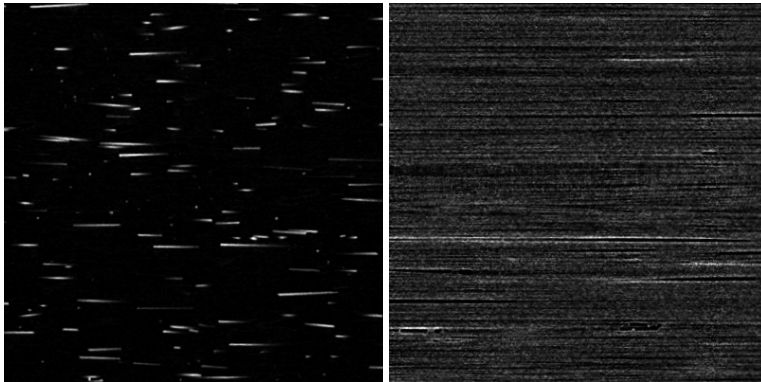


Figure 3.7: CT-Scan of 3D printed ABS GF 10 specimen (left) and the unidirectional continuous carbon fibre reinforced specimen (right) [46].

3.2.2 Fibre Volume Content

Measurement of the fibre volume content from CT-scans requires a high contrast within matrix and fibre material. Hence, those methods are hardly applicable using CFRP samples. As there are further no obvious restrictions to the material system for the determination of fibre volume contents, LFRP material was used directly for the validation of the image processing methods.

3 Material



Figure 3.8: Location of SMC samples on the originally manufactured plate.

DiCo GF SMC

Four discontinuous glass fibre reinforced SMC specimen with a size of $10 \times 10 \times 3 \text{ mm}^3$ were cut from different locations on a plate for validation of thresholding techniques using CT images. Sample locations are illustrated in Figure 3.8 by red ellipses. The plate was manufactured with a fibre volume content of 41 wt %. The semi-finished product was placed over two quadrants of the plate on position C and D and flowed in one direction to the sample positions A and B. The matrix material is an unsaturated polyester polyurethane resin (UPPH) with a density of 1.14 g/cm^3 . Glass fibres have a density of 2.5 g/cm^3 .

LFT

Using LFT material, three glass fibre reinforced samples made of polypropylene (PP) with fibre contents of 10 wt %, 20 wt % and 30 wt % were investigated. The samples were also cut to a size of $10 \times 10 \times 3 \text{ mm}^3$. The densities of the constituents are 0.95 g/cm^3 for PP and 2.5 g/cm^3 for glass fibres.

3.2.3 Fibre Tracking and Fibre Length Distributions

The fibre tracking algorithm enables for the evaluation of FLDs and fibre curvatures. For validation of FLDs, the method can be compared with conventional optical methods based on incineration. Thus, a LFT sample manufactured by injection moulding was used as the average fibre length is short enough to capture it with state of the art CT-scanners. Nevertheless, the method was also applied on a high-resolution scan of DiCo GF SMC in order to demonstrate the applicability on materials with longer fibres even if the actual length of up to 25.4 mm cannot be captured.

IM-LFT

Squared LFT samples with an edge length of a were cropped from injection moulded LFT plates of 4 mm thickness. Fibre content by mass was determined to 28.41 wt % in a plate which was manufactured with equal parameters as the investigated sample. Four different sample sizes were cropped from the sample with an edge length of $a = \{5, 10, 20, 40\}$ mm.

SMC

As the FLD of SMC material is known from the manufacturing parameters and the mean fibre length is much higher than the possible image size, fibres were tracked from CT-images in order to explore the limits of the algorithm.

3.2.4 Surface Curvature

Validation structures of surface curvatures can easily be generated by any spherical objects like bearing balls. Nevertheless, the surface curvature algorithm was also applied to real pores within a CFRP. Note that this method is hardly possible on GFRPs because of the relatively low contrast between matrix material and air.

Reference Object made of Bearing Balls

In order to test the methods for determination of local surface curvatures on real CT-scans, some balls of known diameter were picked from ball-bearings and put into a film container as reference structure. Figure 3.9 illustrates the

3 Material

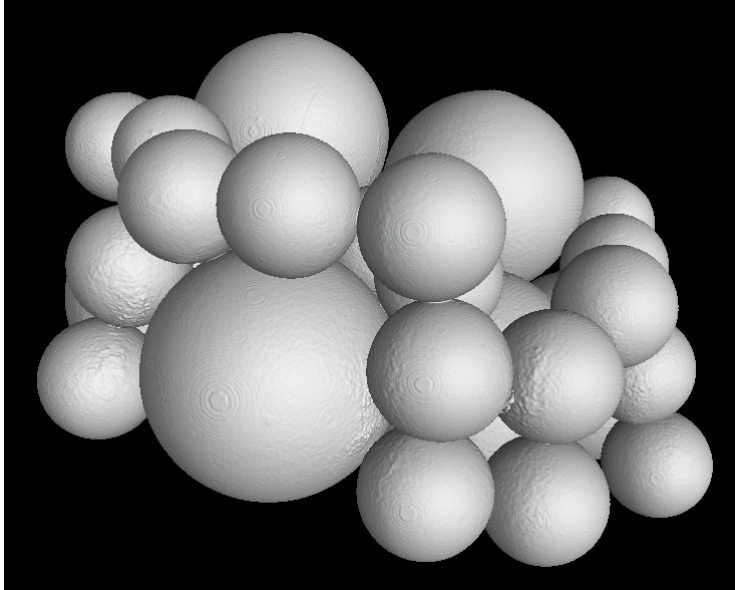


Figure 3.9: CT scan of balls extracted from ball-bearings for validation of curvature analysis [90].

resulting image. The balls have diameters of 8 mm and 4 mm and the film container has a diameter of 31 mm.

Pore Analysis on Continuous CFRP

In order to derive a local surface curvature from real pores, a porous continuous CFRP-layup with PA6 matrix material shown in figure 3.10 was used. The scanned volume has a physical size of $10 \times 10 \times 3.5 \text{ mm}^3$.

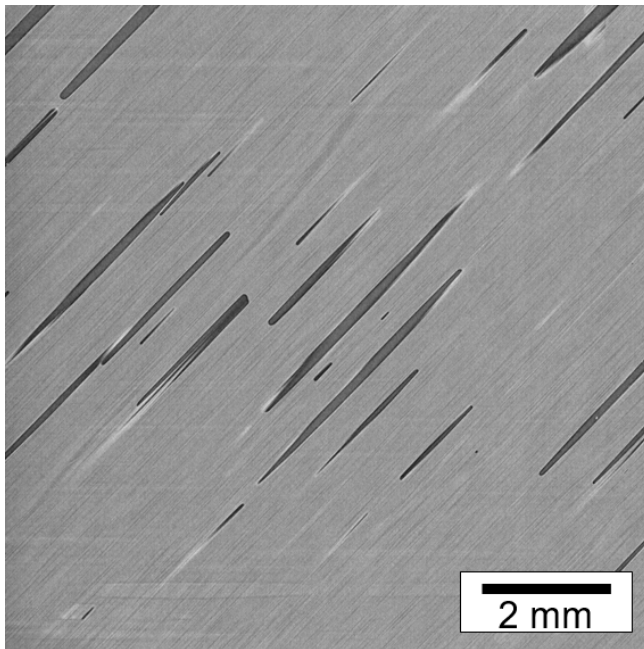


Figure 3.10: CT scan of a carbon fibre reinforced material with pores. Carbon fibres can hardly be recognized while the pores show a high contrast and sharpness.

4 Development of Analytical Methods

4.1 Fibre Orientation Distribution

4.1.1 Implementation of Voxel-Based Methods

Anisotropic Gaussian Filter

The method based on the anisotropic Gaussian filter was mostly implemented in C++ using the *ITK* library. For the partition of the sphere, the original *MATLAB* code by Leopardi [47] is used and imported using the *MATLAB Engine API for C/C++*. The orientations of Leopardi's sphere partitioning are saved to an orientation table containing a sequential number and a corresponding orientation. The initial input image is converted to a float image using the *itk:CastImageFilter*. In section 2.4.2, the method was introduced assuming that the filter mask of the anisotropic Gaussian filter will be rotated. Practically, it is much faster to rotate the entire image since the recursive Gaussian filter is much more efficient than a filter mask. Therefore, a padding is added to the image so it can be rotated without cropping the edges. The rotation is applied using the *itk:ResampleImageFilter*. This transformed image is filtered by an anisotropic Gaussian filter, using the *itk:RecursiveGaussianImageFilter* and applying it for each direction with the blurring parameters λ_1 , λ_2 and λ_3 (see section 2.4.2). The result is compared with an image that includes the highest filter response and the corresponding orientation. This is carried out by the *MaxIntensityFilter*, which writes the number of the orientation and with the corresponding filter response to a vector image in orientation space iteratively for all N orientations. Subsequently the orientation image can be saved either as a vector valued or an integer image which includes the orientation in each voxel as a normed vector or the number of the orientation from the orientation table.

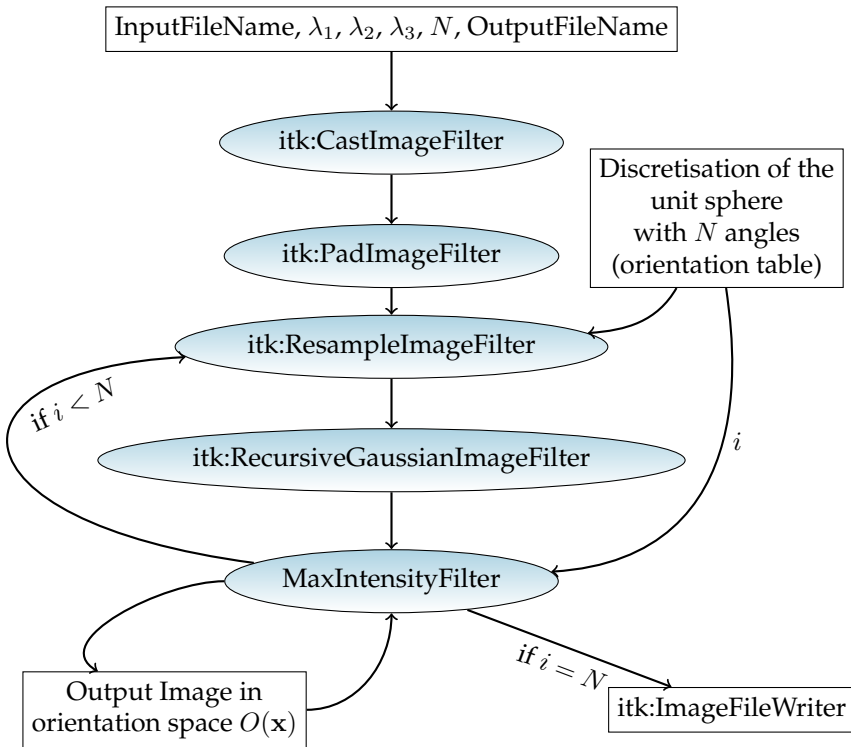


Figure 4.1: Program flow chart for the orientation analysis using the anisotropic Gaussian Filter.

Hessian Matrix

Orientation analysis by the Hessian matrix starts with the *itk:CastImageFilter*, where the input image is transformed to an image of type float. Subsequently, the *itk:HessianRecursiveGaussianImageFilter* calculates the Hessian matrix in each voxel and stores it in form of a symmetric second rank tensor. This step also includes a Gaussian blur, which has to be given to the tool as an input parameter. The orientation is derived by the ITK built in class-function for eigen analysis *itk:SymmetricSecondRankTensor.EigenAnalysis()*. This function returns the eigenvectors and eigenvalues in ascending order, so the first value is used for the orientation in each point. In the last step, the vectors representing the orientation are restricted to one half of the unit sphere in order to avoid redundancy. Furthermore, all vectors appearing on voxels where the original input image is below a certain threshold t are set to zero simultaneously. Fi-

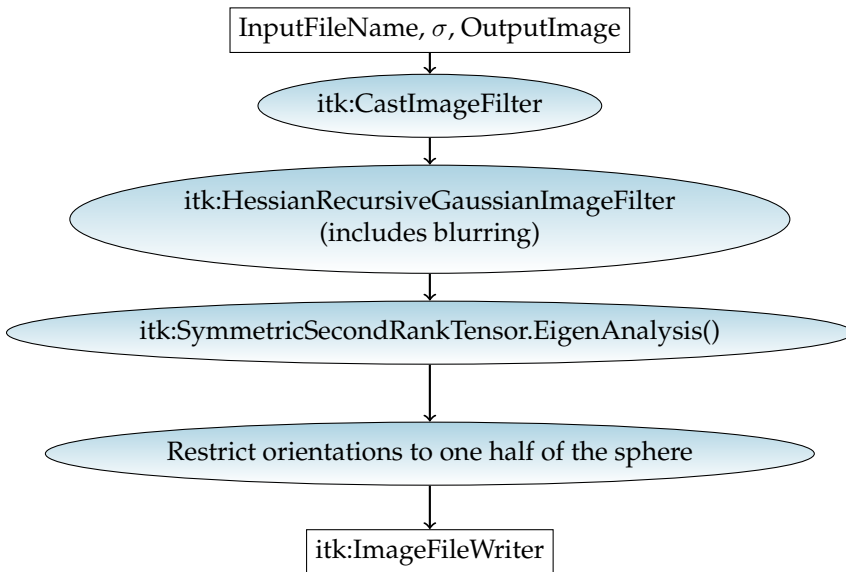


Figure 4.2: Program flow chart for the orientation analysis using the Hessian Matrix.

nally, a vector valued image including the orientation in each voxel is saved as a meta image (.mhd or .mha) using the *itk:ImageFileWriter*.

Structure Tensor

In order to cast the input image to a data type of float, the implementation of the structure tensor based method starts with the *itk:CastImageFilter*. Subsequently, the image gradient is derived using the *itk:GradientImageFilter*. The dyadic product of the gradient (eq. 2.24) is calculated using the ITK built-in iterator class *itk:ImageRegionIterator* and the structure tensor is generated by *itk:RecursiveGaussianImageFilter* (eq. 2.25). The orientation is derived from the structure tensor similarly to the Hessian matrix in the previous section utilizing the class function *SymmetricSecondRankTensor.EigenAnalysis()*. The orientations are restricted on one half on a sphere and voxels below a threshold t in the input image are set to zero in the vector valued output image. The *itk:ImageFileWriter* saves the result as in meta image format.

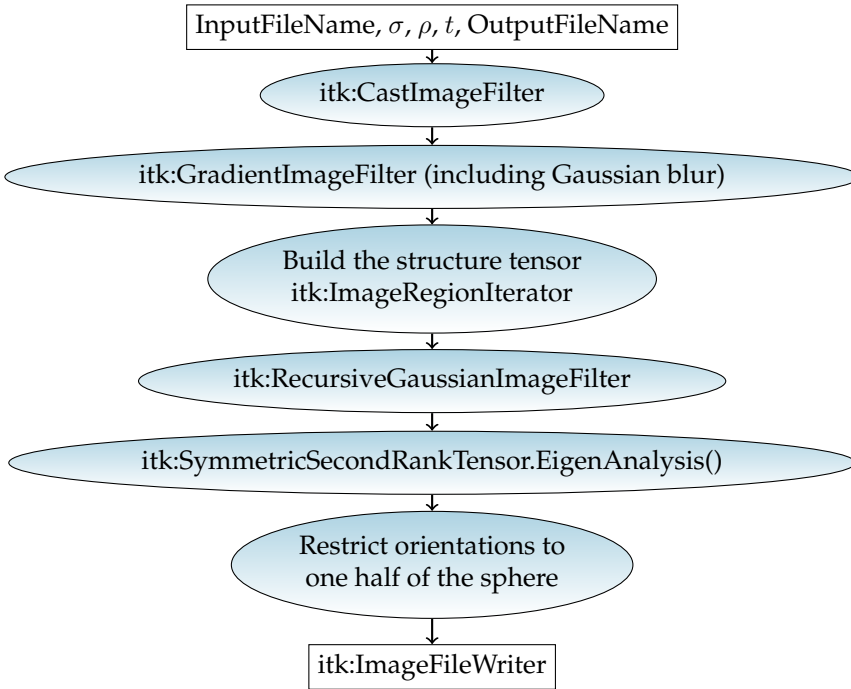


Figure 4.3: Flow chart for the structure tensor based orientation analysis.

4.1.2 Statistical Orientation Distributions

In order to derive statistical descriptors of the orientation from the vector-valued images, the results from the orientation algorithms are imported to *MATLAB* using the MetaImage format. *MATLAB* enables for an easy access to the data as the vectors are stored in a four dimensional matrix and single values or tendencies can be checked easily during the evaluation. Vector valued images are imported using the `mha_read_volume` function available on *Math-Works File Exchange* is implemented by Dirk-Jan Kroon in his toolkit *Read Medical Data 3D*. The image can be imported using the function

```
img = mha_read_volume('FILENAME.mhd');
```

Subsequently, the components of the voxel are accessible using

```
img(c, x, y, z),
```

where c is the component of the orientation vector at the spatial position x, y, z .

Orientation Histograms

The discretization of the orientations on the half sphere is carried out by the tool implemented by Leopardi [47]. Only even quantities of fields on the full sphere are used since the assignment of orientations in the equator plane is not unique if there is an odd number of fields. In general, $N/2$ fields of Leopardi's algorithm for the full sphere are used to generate the histogram. Furthermore, the method results in configurations with and without centre points of the fields in the equator plane. If that is the case and the number of orientations is chosen to be very small, it is not possible to map all the orientations properly to the half sphere as there is no centre point in the equator plane (see Fig. 4.4). This bias is quite large for low numbers of fields like in the middle graph but goes down for larger quantities of fields (e.g. with 150 in the right graph). Nevertheless, only those N with centre points ending up in this equator plane are used for the orientation histograms.

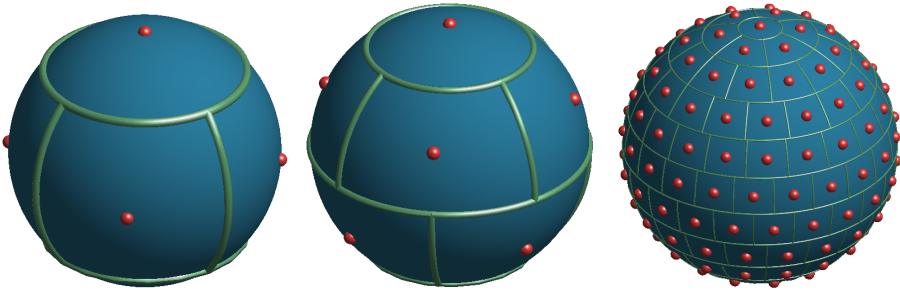


Figure 4.4: Partitions of the sphere created with the *MATLAB* tool of Leopardi. From left to right: Six partitions with centre points in the equator plane / Ten Partitions without centre points in the equator plane / 150 partitions without centre points in the equator plane.

In order to assign the orientations from the vector-valued images to the corresponding fields of the histogram, every vector is compared with the boundaries of each field subsequently. As N is chosen as mentioned before, the assignment of each direction is unique and the search can be skipped after a match to continue with the next vector. Once all voxels of the image are processed, the result can be displayed either in an 3D hedgehog plot or a discrete polar plot. In this contribution, the polar (Fig. 4.5) plot is preferred since it is two dimensional.

4 Development of Analytical Methods

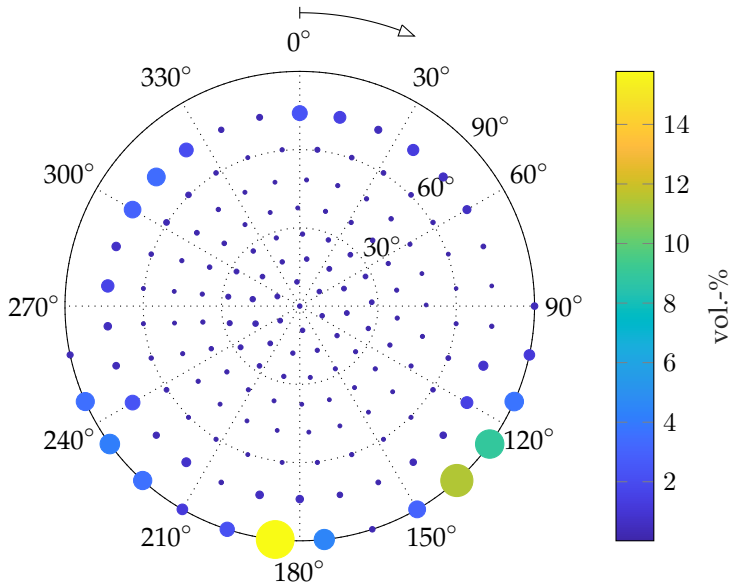


Figure 4.5: Exemplary orientation histogram using a polar plot. Colour and size of each point in the polar plot illustrate the volume fraction of the corresponding orientation.

Orientation Tensors

Orientation tensors are generated across the entire sample or in a smaller region of interest. The *MATLAB* build in functions allow for a fast calculation of orientation tensors by using the sum function in a certain region. E.g. \mathbb{N}_{ij} is given by the sum of all products of the corresponding component of the vectors resulting from the orientation analysis

```
OT2 (n) = sum (sum (sum (img (i, :, :, :) .* img (j, :, :, :))) );
```

Due to the symmetries, only six of the 9 components have to be stored for the 2nd order tensor. To save those tensors efficiently, they are written to an ASCII file in order

```
[a_11 a_12 a_13 a_22 a_23 a_33]
```

where each a_{ij} is stored to the corresponding n th position to the array $OT2 (n)$. Orientation tensors of 4th order can be fully described with 15 independent components which are saved in order

[a_3333 a_3332 a_3322 a_3222 a_2222 a_3331 a_3321 a_3221
a_2221 a_3311 a_3211 a_2211 a_3111 a_2111 a_1111]

and calculated similar to the 2nd order tensors.

4.1.3 Artificial Images and Error Criterion

The validation of orientation data from real CT-data acquired from fibre reinforced polymers it hardly possible as there is no non-destructible method to analyse it with reasonable effort. For that reason, all algorithms were applied to artificial images with known orientation in a first step in order to define error criteria that allow for the evaluation of the algorithms used.

One and Two-Fibre Models

In a first simple approach, a tool was implemented in *ITK* to generate artificial images of cylinders with certain angle θ and distance d . Figure 4.6 illustrates the most important parameters. Further parameters that have to be specified are the edge length of the image w , the fibre diameter D and two angles to rotate the fibres within image in order to make sure that fibres are not aligned to the regular image grid. All lengths and diameters are given in voxels.

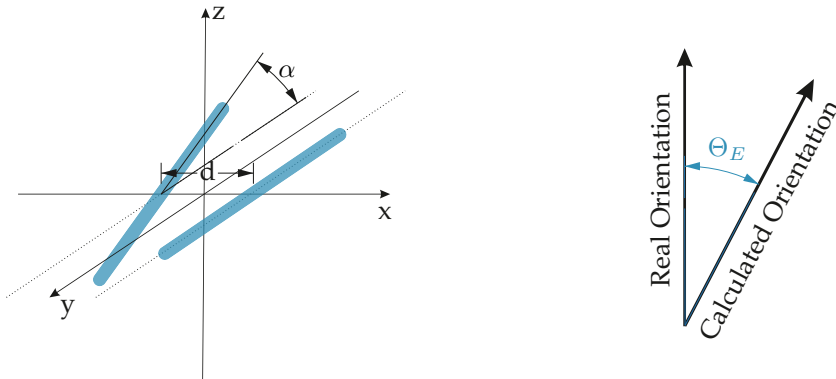


Figure 4.6: Left: Arrangement of the two-fibre models. Images are generated with variable distance d , and angle α . Right: Error in orientation θ_E , which is calculated in each fibre voxel [46].

4 Development of Analytical Methods

The tool generates a binary image as well as a vector valued image that includes the correct orientation in each white voxel of the binary image. The binary image is used as input for all of the implemented algorithms mentioned in section 4.1.1 while the vector valued image provides the data to evaluate an error criterion for each image. This error can be considered on various scales. Locally, it is defined as the spatial angle between the real orientation and the one provided by the orientation algorithm in each voxel (Figure 4.6) and is noted as θ_E . On a global scale for an entire image, θ_{gE} is specified as the average of all local misalignments within an image

$$\theta_{gE}(I(\alpha, d)) = \sum_{i=1}^N \frac{\theta_{E,i}}{N} \quad (4.1)$$

where N is the number of fibre voxels. $I(\alpha, d)$ refers to an image that is generated with the angle α and the distance d between two fibres. Note that the error θ_E cannot be larger than 90° and thus, the global error is $0^\circ \leq \Theta_{gE} \leq 90^\circ$.

As this global measure only takes one configuration of α and d into account, another value is introduced to respect for the fibre architecture. E_A is the average of all global errors Θ_{gE} for a certain set of configurations of the artificial images

$$E_A = \sum_{i=1}^{N_\alpha} \sum_{j=1}^{N_d} \frac{\theta_{gE}(I(\alpha_i, d_j))}{N_\alpha \cdot N_d}. \quad (4.2)$$

N_α and N_d are the total number of angles and distances to investigate. This method enables to estimate the performance of the algorithms for different fibre architectures like unidirectional or isotropic distributed structures.

Orientation Tensors

Artificial microstructures based on orientation tensors were built with the commercial tool GeoDict[®]. It enables to generate microstructures based on orientation tensors with or without periodic boundary conditions. The resulting images were processed with the methods for orientation analysis in section 4.1.1 and the orientation tensor was built from those results. As error measure, the Frobenius norm of the difference of the input and output orientation tensor (\mathbf{N}_I and \mathbf{N}_O) was divided by the Frobenius norm of the input orientation tensor

$$E_T = \frac{\|\mathbf{N}_I - \mathbf{N}_O\|_F}{\|\mathbf{N}_I\|_F}. \quad (4.3)$$

This measure becomes zero for a result that matches the input tensor perfectly, but it can become larger than one due to deviatoric components.

4.1.4 Separation of different Microstructures

Using the local orientation information e.g. in form of orientation tensors, it is possible to separate layers with different microstructures or orientation from layups. Considering an orientation tensor of a planar isotropic material like SMC, the eigenvalues of a local orientation tensor are nearly

$$\lambda_1 \approx \lambda_2 \approx 0.5, \lambda_3 \approx 0. \quad (4.4)$$

The ideal orientation tensor for a unidirectional fibre architecture results in

$$\lambda_1 \approx 1, \lambda_2 \approx \lambda_3 \approx 0 \quad (4.5)$$

so the transition between an SMC and any unidirectional reinforced material can be found by investigating the eigenvalues of a hybrid specimen over thickness in z -direction. For this purpose, the quadratic coherence measure is defined as

$$c = \left(\frac{\lambda_1 - \lambda_2}{\lambda_1 + \lambda_2} \right)^2, \quad (4.6)$$

where λ_1 and λ_2 are the largest eigenvalues of the orientation tensor. The orientation tensors are not evaluated in an isotropic region, but in a plane parallel to the plate surface. This avoids an error resulting from the next layer. Using this method, the area taken into account has to be large enough to include many fibre rovings of the SMC with different orientations to lower the coherence measure c compared to adjacent UD layers.

The segmentation of UD layers with different orientations in a layup can be separated by investigating the principal orientation of the orientation tensor in each layer. Therefore, the eigenvector of the highest eigenvalue in each layer is observed along the z -axis. In ideal case, the derivative of the planar angle - which is derived from the eigenvector - shows a peak at the interface between two layers.

4.2 Fibre Tracking in CT-images

The methods for fibre tracking introduced in this section have been developed in cooperation with fellow colleague Benjamin Bertram. The algorithms are partially published in [30].

In order to derive fibre length distributions or the curvature of fibres from CT-images, their centrelines have to be tracked. Raw high-resolution images of glass fibre reinforced polymers show many touching points of the fibres. This can be a problem since the algorithm can result in the wrong path and connect branches that do not belong to the same fibre. Thus, a set of filters described from section 4.2.1 to 4.2.4 was implemented or adapted to prevent incorrect assignments.

4.2.1 Circular Voting Filter

The circular voting filter was implemented to gain the centrelines of cylindrical structures and to filter out noise and particles. It is used as a pre-filter for the subsequent tracking algorithm. The basic idea of this method is to thin the fibres of the initial image and thus rise the distance between them. Common filters for improving fibrous structures, e.g. the anisotropic diffusion filter, need a lot of input parameters that are not very user-friendly since they are based on the differential equations of Fick's method. In contrast to this, the circular voting filters most important input parameter is the fibre radius. Since the diameter of glass fibres does not vary in a large range, we assume it to be constant. Using it as an input for the filter, the parameter adjustment is easy since it can be measured directly from the raw CT-image.

The circular voting filter is a combination of a surface normal overlap measure w which takes the fibre radius into account, and a coherence measure κ that is derived from the structure tensor. Both make only use of the first derivative of the input image and are combined to the circular voting filter response f_{cv}

$$f_{cv} = \kappa_i^{c_m} \cdot w_i^{1-c_m}. \quad (4.7)$$

Surface Normal Overlap Measure

In order to gain the centreline of the fibres, a surface overlap measure w was taken into account [91]. Figure 4.7 shows the principle of the filter. It is implemented as a filter mask, which is evaluated in each voxel of the image. From

4.2 Fibre Tracking in CT-images

each voxel, the known fibre radius R is combined with a Gaussian function with the blurring factor σ_r .

$$w_i = p_i \exp - \left(\frac{|||r_i|| - R|}{\sigma_r} \right)^2 \quad (4.8)$$

Using this blurring function, also gradients that differ slightly from the real radius are taken into account. Since only the gradients pointing towards the centre point are of interest, the weight function p_i was defined:

$$p_i = \begin{cases} 1 & \text{if } \angle(\nabla(x_i), r) < 60 \\ 0 & \text{else} \end{cases} \quad (4.9)$$

As the orientation of the fibre is not known initially, the filter is looking up a spherical region around the present voxel, what is illustrated by the blurred blue circular region in figure 4.7. If the angular deviation a_i is small, the filter responses a high value what leads to a sharp bright line in the middle of each fibre if the entire image is taken into account.

$$w = \sum_{i \in S} w_i \exp - \left(\frac{a_i}{\sigma_a} \right)^2 \|\nabla(x_i)\| \quad (4.10)$$

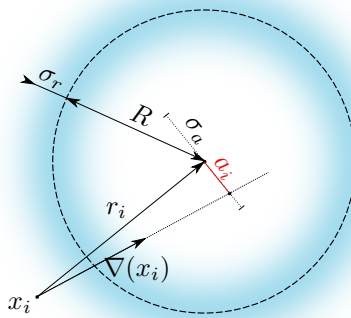


Figure 4.7: Principle of the Circular Voting Filter.

4 Development of Analytical Methods

This filter is used as a medialness filter which returns a high response for every voxel that is located in the centre of a fibre or a sphere. Actually, the response in spherical inclusions will be even higher than in fibres if the radius of it is equal the fibre diameter since all the gradients are pointing to the centre point.

Coherence Measure

Since the medialness measure w leads also to high values for spheres, it is combined with the coherence measure derived from the structure tensor that was defined in section 2.4.2. Therefore, the dyadic products of the image gradients are weighted by the medialness measure to enhance the impact of voxels which are likely to be fibre voxels.

$$\mathbf{J}(W) = \sum_{i \in S} w_i \nabla(x_i) \nabla(x_i)^\top \quad (4.11)$$

Subsequently, the eigen analysis is carried out in each voxel and the coherence measure

$$\kappa(\mathbf{J}) = \frac{\lambda_2}{\alpha + \lambda_3} \quad (4.12)$$

is calculated from the eigenvalues of the structure tensor, where α is a infinitesimal small number to prevent division by zero errors. The eigenvalues are in order $\lambda_1 \geq \lambda_2 \geq \lambda_3$.

4.2.2 Segmentation and Skeletonization

The pre-filtered image is binarized by an ordinary thresholding operation in ImageJ. The threshold is adjusted by hand since a different choice of the fibre radius in the CircularVoting step will influence the data in a way that it is not possible to use a certain thresholding technique like those described in section 2.3.3. For the binarization, the user has to pay attention that the threshold is neither too high so that the fibre is no more connected nor too low so that neighbouring fibres appear to be in contact to each other. The subsequent skeletonization is carried out by the ImageJ plugin described in section 2.3.4.

4.2.3 Tracking Algorithm

The algorithm used for fibre tracking is based on the open-source *ImageJ* plugin *AnalyzeSkeleton* initially implemented by Arganda-Carreras [29] and was modified in order to analyse fibre reinforced polymers. The original method evaluates a skeleton and gives back a couple of characteristics like the number of branches and junctions for each skeleton. As the algorithm is utilised to process fibres that do not have any junctions, some changes had to be implemented to the code. After the skeleton is labelled like described in section 2.3.4, every junction of the skeleton is analysed and dissolved subsequently. Therefore, the local orientation is taken into account. Each branch that is connected to the present junction is followed for a certain number of voxels to calculate a vector from this point to the vertex point. Subsequently, this vector of every adjacent branch is normalised and multiplied with all of those of all other branches of the present junction to get the scalar directional accordance γ .

$$\gamma = \mathbf{n}_i \cdot \mathbf{n}_j \quad (4.13)$$

If γ results in -1, the branches outward in the opposite directions and it is likely that the branches belong to each other. If it is 1, the branches go off in the same direction and it is unlikely that they belong to the same fibre. The directional accordance is taken as a criterion to connect two segments of a fibre that were erroneously subdivided due to a touching point in the thresholded image. If more than two branches are connected to a junction, the two segments with the lowest directional accordance are assigned first by giving them a consecutive number for each fibre. This is subsequently done for all remaining branches until none of them remain unassigned. In case there is a residual single branch after all other segments are assigned, it is assumed to be a new independent fibre that accidentally ended on another one. Figure 4.8 shows the algorithm on an minimal example. Sub-figure (a) shows apparently 3 fibres that are connected in 2D. The junctions are marked with red dots and an italic number from one to three. In a first step, those branches with the lowest directional accordance are connected by giving them the same label. The label is a sequential number while all segments with the same number belong to the same fibre. On the first crossing, the straight segments show the lowest γ and are labelled with one. The remaining branches are assigned to fibre two. Since all segments on junction one are satisfied, the algorithm proceeds with the second one (Figure 4.8 (c)). Again, the straight fibres show the lowest directional correspondence, but in this case one of the branches is already labelled. Thus, the related branch is given the same number. Both remaining branches are labelled with three. As the algorithm processes the third and last junction (Figure 4.8 (d)), the most matching branches are marked with different numbers. Hence,

4 Development of Analytical Methods

Table 4.1: Exemplary output file for three dimensional fibre paths extracted from a volumetric image by the modified ImageJ plugin AnalyzeSkeleton.

```
Fibre No. 1
x      y      z
100    200    300
101    200    300
102    200    300
103    200    300
...
Fibre No. 2
x      y      z
100    250    300
101    250    300
...
```

one of the branches - No. 3 in the example - has to be relabelled. Also, all the other segments belonging to fibre 3 have to be re-labelled in order to connect them. The last remaining segment on the third junction is assumed to be an independent fibre and is labelled with a new sequential number. Once all the segments are assigned to particular fibres, all the voxels of the centrelines are written to an output file. The file has the format shown in Table 4.1 and can be used in order to fit parametrized spatial curves in a further step.

4.2.4 Parametrization of Spatial Curves

Using the fibre voxels and the information about the connectivity of the fibre tracking algorithm, the fibres can be described by a parametrized curve

$$t \mapsto \mathbf{f}(t) \in \mathbb{R}^3, a \leq t \leq b \quad (4.14)$$

along the fibre axis, where $t \in [a, b]$ can be understood as time. In general, there are infinite possibilities to define the same spatial curve with varying velocity. Those curves are fitted to the centre points of fibres derived in the previous section by B-spline functions. Therefore, the *MATLAB* built-in function *spap2* is used. To receive continuous functions for the curvature of the splines on the transition points, a function of at least third order has to be applied. It is also necessary to ensure that the splines can be approximated to the voxel paths sufficiently but are not over-fitted. If the interval of each B-spline fit is chosen too short, the splines can get wavy due to quantification on the voxel pattern.

4.2 Fibre Tracking in CT-images

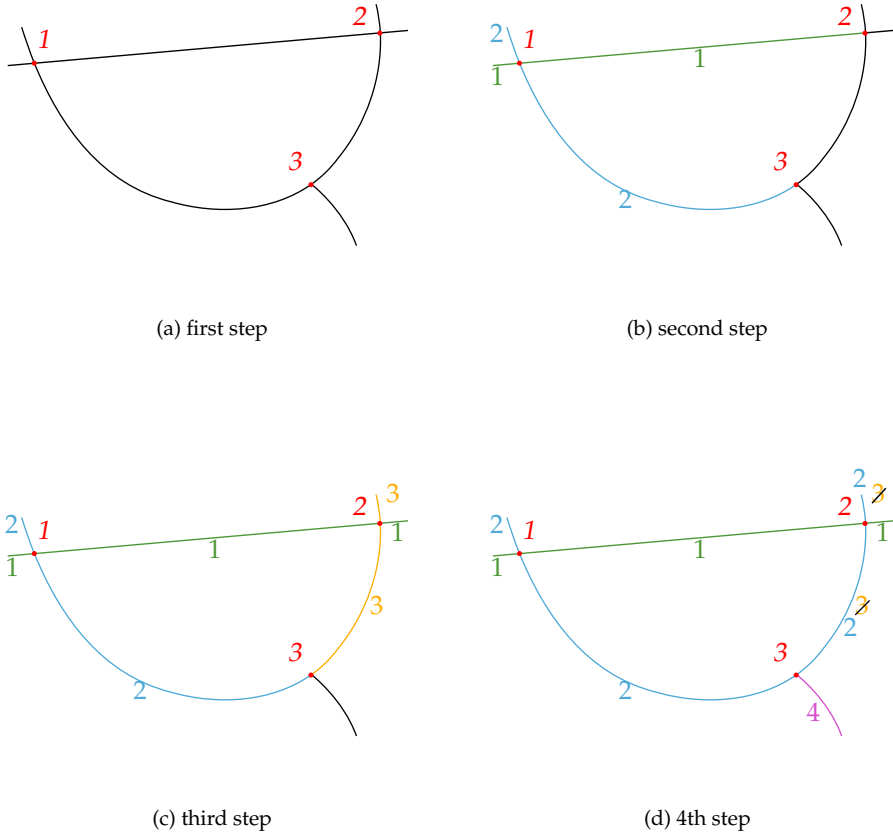


Figure 4.8: Minimum example for additional added method for fibre tracking [30].

Experience has shown that a segment length of twenty voxels produces good results with B-splines of third order. Figure 4.9 shows an exemplary fit of a twelve voxel long fibre. The upper picture shows a fit with a fitting interval of 20 points while the B-splines of the image below are fitted to only 3 points. As the voxel size is only $3\ \mu\text{m}$, the curvature appearing in the latter fit is pretty high because it follows the quantification errors resulting from noise and the voxel grid.

4 Development of Analytical Methods

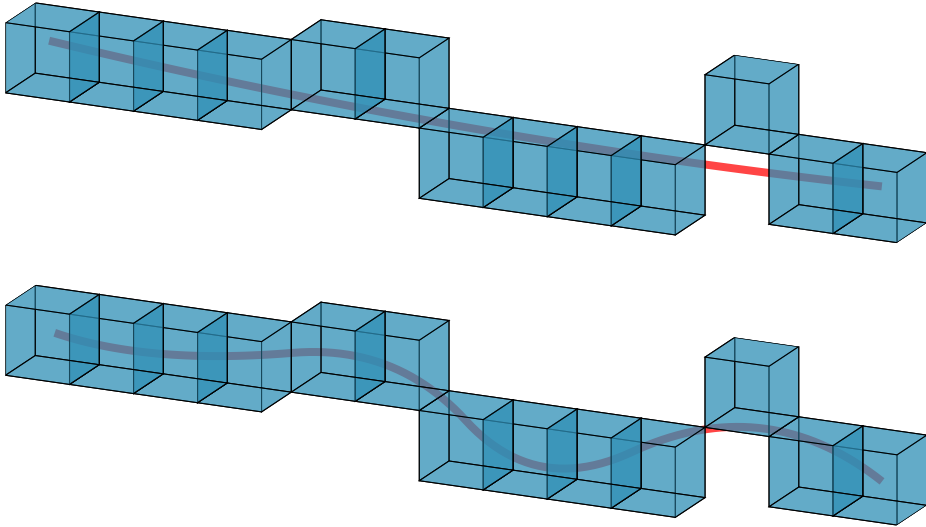


Figure 4.9: B-spline fit of a 13 voxel long fibre. Blue cubes depict the skeletonized fibre with a voxel size of $3 \mu\text{m}$. Above: B-spline interval of 20 points. Below: Same B-spline fit with an interval of only 3 points. The fibre is clearly over-fitted.

For easier handling, the resulting curves are converted in a parametrization in dependence of the arc length

$$s \mapsto \mathbf{z}(s) \in \mathbb{R}^3, 0 \leq s \leq L, \quad (4.15)$$

where

$$\|\mathbf{z}'(s)\|_2 = 1. \quad (4.16)$$

Using this parametrization, $\mathbf{z}(s)$ is defined from 0 to the fibre length L (Fig. 4.10).

4.2.5 Fibre Length Distribution from Spatial Curves

The length of a single fibre can be extracted either from the raw B-splines by integrating over time t

$$L = \int_a^b \|\dot{\mathbf{f}}(t)\|_2 dt \quad (4.17)$$

or directly by using the length L from curves parametrized by arc length. However, the length is determined, the lengths of each fibre is saved to a list with N entries, where N is the number of fibres within the image region. On that basis, the FLD can be created by summing up fibres with a length belonging to specified bins (see section 2.5).

4.2.6 Fibre Orientation Tensors from Spatial Curves

Assuming the diameter of the fibres to be constant, the resulting length weighted orientation tensor should be nearly the same as the volume weighted from voxel-based methods. For a spatial curve $z(s)$ parametrized by the arc length, length weighted orientation tensors of second order can be calculated by integrating the dyadic product of the tangent vector along the fibre axis s

$$N_{ij} = \frac{1}{L_a} \sum_{\alpha=1}^N \left[\int_0^{L_\alpha} z'_{\alpha,i}(s) \cdot z'_{\alpha,j}(s) ds \right] \quad (4.18)$$

and fourth order orientation tensors by

$$N_{ijkl} = \frac{1}{L_a} \sum_{\alpha=1}^N \left[\int_0^{L_\alpha} z'_{\alpha,i}(s) \cdot z'_{\alpha,j}(s) \cdot z'_{\alpha,k}(s) \cdot z'_{\alpha,l}(s) ds \right]. \quad (4.19)$$

The subscript α refers to a certain fibre out of the total number of fibres N in the entire image. L_a is the accumulated length of all fibres and is used to normalize the resulting orientation tensor.

4.2.7 Fibre Curvature and Torsion from Spatial Curves

Another formulation of parametrized spatial curves used in the following are the Frenet-Serret equations:

$$\frac{dt}{ds} = \kappa \mathbf{n}_s \quad (4.20)$$

4 Development of Analytical Methods

$$\frac{d\mathbf{n}_s}{ds} = -\kappa\mathbf{t} + \tau\mathbf{b} \quad (4.21)$$

$$\frac{d\mathbf{b}}{ds} = -\tau\mathbf{n}_s \quad (4.22)$$

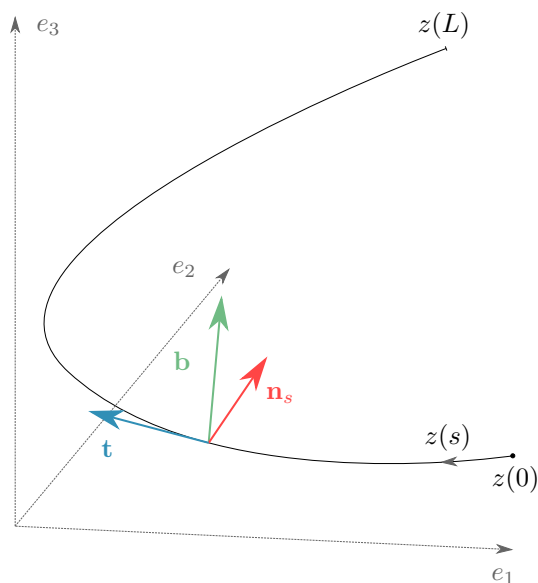


Figure 4.10: Parametrization of spatial curves. The moving coordinate system used in the Frenet-Serret equations is defined by the tangent unit vector \mathbf{t} , the binormal unit vector \mathbf{b} and the normal unit vector \mathbf{n}_s .

Those equations enable to describe a spatial curve only by its curvature κ and torsion τ using a local moving coordinate system (Fig. 4.10) defined by the tangent unit vector \mathbf{t} , the binormal unit vector \mathbf{b} and the normal unit vector \mathbf{n}_s . As this kind of parametrization results in $\kappa(s)$ and $\tau(s)$, the curvature and torsion over length can be used to calculate an average, maximum or minimum value or even to build histograms for the region at hand.

4.3 Porosity and Inclusion Analysis

4.3.1 Segmentation and Volume Fraction

Segmentation of pores or inclusions from the base material can be achieved using thresholding techniques as introduced in 2.3.3. In some cases, it can also be necessary to segment e.g. touching particles. If they are nearly spherical, a distance transform combined with the watershed filter can be used. Figure 4.11 shows an example of this algorithm. The distance transform is applied on the image that includes the touching objects. It sets the grey value of each voxel to the shortest distance to leave the same. Hence, values in the middle of the object will be high while the values on the edges will decrease to zero (Figure 4.11 (b)). Subsequently, the watershed filter is applied. The 2D image can be imagined as a 3D surface plot with the grey values on the z-axis. In a first step, the image resulting from the distance transform has to be inverted as otherwise the centre points of the objects have the highest values. Now the image is "flooded" virtually by increasing the grey value. Fig. 4.12 illustrates this method for the one-dimensional case. The structures can be separated on the points where the virtual fluid touches first while flooding. Actually, there will be touching lines in 2D images (Fig. 4.11 (d)) and touching surfaces in 3D images.

4.3.2 Determination of Surface Curvature

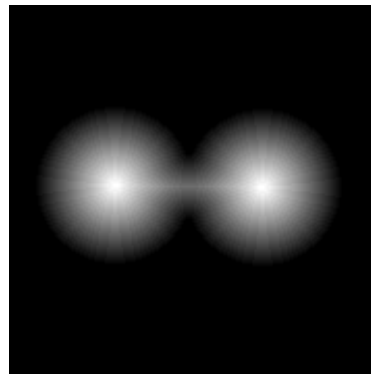
Surface curvature allows for a detailed description of pores and inclusions. Within this thesis, two methods are compared on artificial data as well as on real CT-scans in order to rate the performance.

Implementation of Patch-based Method

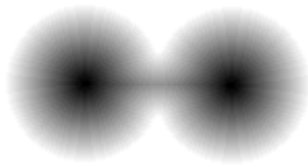
Implementation of the patch-based algorithm is adopted from the Advanced Normalization Tools (ANTs) with respect to the method explained in section 2.7.2. As the patch-based evaluation requires a binary image, the input data has to be segmented previously for an exact localization of the surfaces within the image. Once the principal curvatures are determined, the output can be chosen as Gaussian, mean, minimal or maximal curvature.



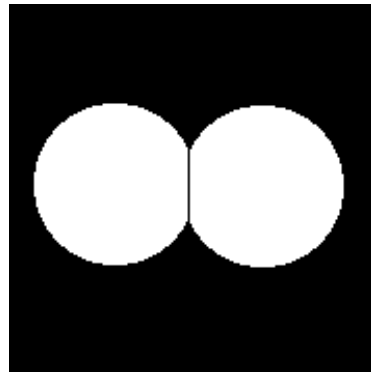
(a) Initial binary image



(b) Distance transform



(c) Inverted distance transform



(d) Segmentation line on the front of the flood that is touching initially

Figure 4.11: Example of the distance transform and the watershed filter for segmenting binary images.

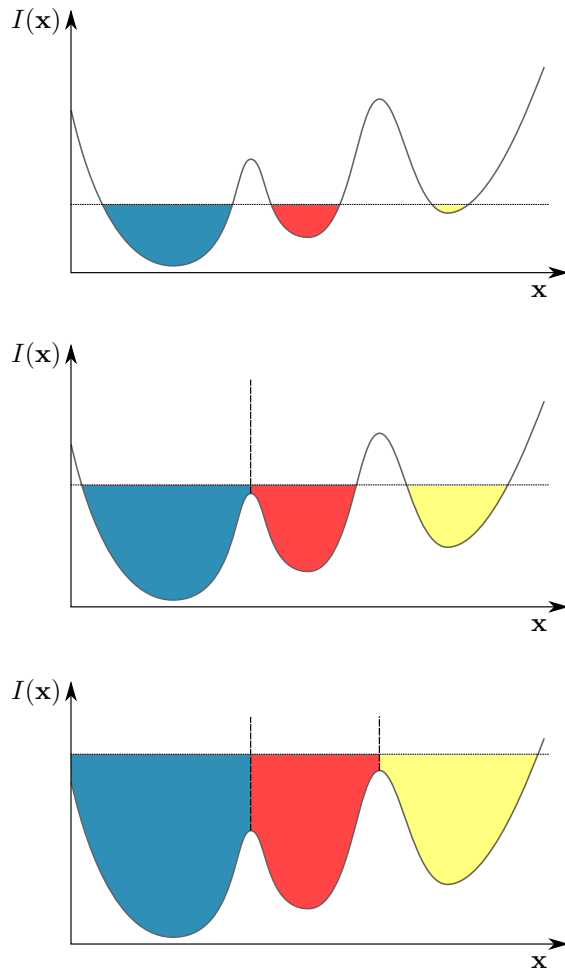


Figure 4.12: Watershed segmentation illustrated on an one dimensional example.

Implementation of Hessian-based Method

Curvature analysis using the Hessian matrix is carried out on the grey value image. In a first step, the image is filtered by a Gaussian blur using the input parameter σ . Subsequently, the Hessian matrix is calculated in each image point in order to derive the shape operator (eq. 2.49). Therefore, an arbitrary orthonormal basis is derived from the image gradient by calculating its cross product with an arbitrary vector. Principal curvatures are derived from the eigenvalues of the shape operator. Finally, the entire image is masked by an edge detection on the initial image to delete all curvatures from non-surface voxels.

Artificial Images and Error Criterion

To validate and compare the methods introduced in section 2.7.2, artificially generated structures were used in a first step. The ITK library was used for building volumetric images including spheres with a specified diameter and thus known curvature. Input parameters for the tool are the edge length of the image w and the sphere diameter d .

As curvatures from artificial test images are known, a local error can be calculated on each surface point. Thus, the difference of the curvature in each point is subtracted and divided by the number of surface voxels N_s .

$$E_c = \frac{1}{N_s} \sum_{i=1}^N \left(\kappa_i - \frac{1}{R} \right) \quad (4.23)$$

In order to calculate the percentage error, E_c can be divided by the real curvature, what leads to

$$E_{c,p} = \frac{R}{N_s} \sum_{i=1}^N \left(\kappa_i - \frac{1}{R} \right) * 100 \%. \quad (4.24)$$

5 Experimental

5.1 CT-Scanners

5.1.1 YXLON CT Precision

Unless expressly stated otherwise, CT-scans shown within this thesis are acquired using an YXLON CT Precision computed tomography system (Fig. 5.1). It is a cone-beam industrial CT system with a maximum resolution of $1\ \mu\text{m}$. The built in FeinFocus tube is an open system which enables to swap the tube-head from a reflection to a transmission tube. The maximum acceleration voltage is 225 kV. The power of the tube is up to 10 W using the transmission and up to 200 W with the reflection tube head. The detector was manufactured by PerkinElmer and has an edge length of 409.6 mm at 2048 pixels. Its surface is protected by a plate of carbon fibre reinforced polymer.



Figure 5.1: YXLON CT Precision computed tomography system.

5.1.2 Zeiss Xradia 520 Versa

The Zeiss Xradia 520 Versa is an X-ray microscope, which combines computed tomography with an optical magnification allowing for the acquisition of high resolution images even with larger samples. The maximum spatial resolution is $0.7\ \mu\text{m}$. Its X-ray source is a sealed transmission tube with an acceleration voltage of 30-160 kV and a maximum power of 10 W. It provides many built-in filters mounted on an automated filter charger and offers the possibility of lab-scale phase contrast measurements, which lead to a higher contrast between materials of the same density like e.g. carbon fibre reinforced polymers.

5.2 Fibre Orientation Distribution

5.2.1 Artificial Images

Artificial data with only one or two short fibres with an aspect ratio of 8 were generated as described in section 4.1.1 in order to optimize input parameters for the implemented orientation analysis approaches and to compare those approaches with each other. Short fibres are used because the aim of this investigation is to provoke critical areas and the fibre ends are most sensitive to misalignments resulting from analysis. In a first step, an artificial single fibre of 80 voxels length and 10 voxels diameter was evaluated with each method within an image with an edge length of 100 voxels. For investigations with two fibres, two configurations have been carried out: The first one with a fibre diameter of 5 voxels, fibre length of 40 voxels and an image size of 50 voxels. The second configuration included fibres of 10 voxels diameter, a length of 80 voxels and an edge length of 100 voxels. For fibre distances and angles (cf. 4.6) an experimental table was created to model the error for a isotropic fibre distribution. Angles were varied from 0° to 90° in steps of 10° . Fibre distances were chosen from zero for touching fibres to one fibre diameter in 6 steps. To avoid a positive influence of the alignment of fibres to the voxel grid, the first fibre was rotated by 20° about the x and the y axis. The rotation of the second fibre started from the new coordinate system. Figure 5.2 shows the output of the implemented tool in 3D. Binary images were generated for all previously mentioned configurations and processed using one out of the three tools for orientation analysis introduced in section 4.1.1.

From the resulting data, the fibre architecture dependent error (eq. 4.2) was calculated. Input parameters for each method were modified and tested with an exhaustive grid search to find the optimum in dependence of the fibre diameter. Table 5.1 shows the modified input parameters for each method. The

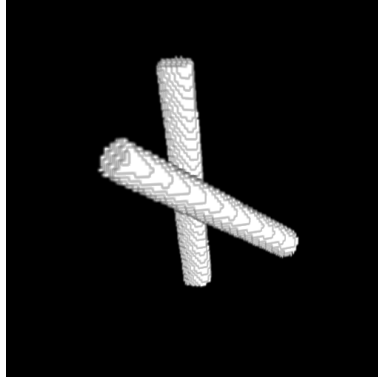


Figure 5.2: Artificially generated images of two fibres with certain distance and angle.

Table 5.1: Variable input parameters for orientation analysis tools for optimization.

Anisotropic Gaussian filter	α, σ
Hessian matrix	σ
Structure tensor	ρ, σ

eigenvalues λ_1, λ_2 and λ_3 of the anisotropic Gaussian filter are simplified by the aspect ratio α and the eigenvalue of the smaller principal axis of the ellipsoid σ . The minimum error of each method using those optimized parameters was taken for a first comparison of the orientation analysis algorithms.

In a further investigation, artificial fibre architectures were built with GeoDict[®]. Those images were generated using two different orientation tensors: A first one \mathbf{N}_U representing a unidirectional orientation distribution and another one called \mathbf{N}_I .

$$\mathbf{N}_U \hat{=} \begin{bmatrix} 1 & 0 & 0 \\ 0 & 0 & 0 \\ 0 & 0 & 0 \end{bmatrix}, \quad \mathbf{N}_I \hat{=} \begin{bmatrix} 0.25 & 0 & 0 \\ 0 & 0.25 & 0 \\ 0 & 0 & 0.5 \end{bmatrix}. \quad (5.1)$$

Figure 5.3 illustrates the resulting structures in 3D with a fibre volume content of 5 vol %. All fibres have a diameter of 5 voxels and an aspect ratio of $\alpha = 40$. For validation of orientation analysis tools, the following structures were used:

- One unidirectional structure with 5 vol %

5 Experimental

- Three structures using orientation tensor \mathbf{N}_I with 5 vol %, 13 vol % and 20 vol %.
- One structure with randomly curved fibres consisting of multiple straight segments with a length of 5 voxels and the orientation tensor \mathbf{N}_I with 5 vol %.

The fibre content by mass changes with the density of the constituents. Nevertheless, assuming a matrix density of 1 g/cm^3 and glass fibres with a density of 2.6 g/cm^3 , the fibre content by mass will result in approximately 12 wt %, 28 wt % and 39 wt % at the investigated fibre volume fractions of 5 vol %, 13 vol % and 20 vol %. The orientation tensors derived from those artificial volumetric images are used to calculate an error based on the error criterion E_T in section 4.1.3 for the evaluation of the orientation analysis methods. Therefore, input parameters were chosen as follows:

- Gaussian filter: $\sigma = 3$ voxels
- Hessian matrix: $\sigma = 3$ voxels
- Structure tensor: $\sigma = 0.8$ voxels, $\rho = 3$ voxels

5.2.2 Real Images with known Orientation

For validation of the introduced methods on real images, materials introduced in section 3.2.1 were used. Those materials have an almost unidirectional fibre orientation distribution and thus, the evaluated orientation tensor should result in \mathbf{N}_U . As error criterion, E_T is calculated for each structure using the three orientation analysis methods introduced in chapter 4.

3D-Printed Specimen

The image of the 3D-printed specimen was acquired using the parameters shown in table 5.2. As the contrast between fibre and matrix material is high, it is possible to separate both phases and apply the statistics for the orientation tensor only on the fibre material (cf. Fig. 3.7 right). For investigations regarding fibre orientation, the input parameters were set to:

- Anisotropic Gaussian filter: $\sigma = 2$ voxels
- Hessian matrix: $\sigma = 2$ voxels
- Structure tensor: $\sigma = 0.2$ voxels, $\rho = 2$ voxels

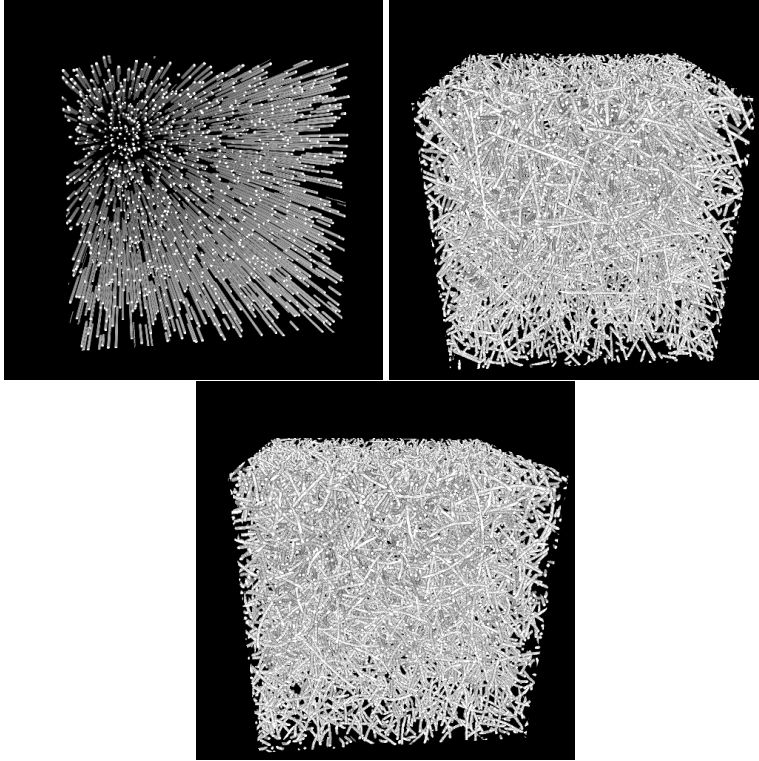


Figure 5.3: Artificial images generated with GeoDict[®]. Left: Unidirectional fibres (\mathbf{N}_U). Right: Fibre architecture with straight fibres and orientation tensor \mathbf{N}_I . Bottom: Fibre architecture with curved fibres and orientation tensor \mathbf{N}_I [46].

Table 5.2: Image acquisition parameters for 3D-printed glass fibre reinforced ABS sample.

Tube head	Transmission tube
Target	Tungsten
Acceleration Voltage	100 kV
Tube current	0.02 mA
Focus-object distance	25.64 mm
Focus-detector distance	849.90 mm
Voxel size	5.87 μm
Integration Time / Pixel binning	1000 ms / 2

5 Experimental

Pultruded Carbon Fibre Rod

The validation of the orientation analysis methods on the pultruded carbon fibre rod was carried out to investigate the accuracy on low-contrast images. Note that the fibres could not be separated from the matrix material and thus every voxel was taken into account in order to determinate the orientation tensors (cf. Fig. 3.7 right). Image acquisition parameters are listed in Table 5.3 and the parameters for the orientation analysis were chosen as follows:

- Gaussian filter: $\sigma = 1$ voxels
- Hessian matrix: $\sigma = 2$ voxels
- Structure tensor: $\sigma = 0.2$ voxels, $\rho = 4$ voxels

Table 5.3: Image acquisition parameters for carbon fibre reinforced pultrusion rod.

Tube head	Transmission tube
Target	Tungsten
Acceleration Voltage	120 kV
Tube current	0.03 mA
Focus-object distance	17.64 mm
Focus-detector distance	849.84 mm
Voxel size	4.04 μm
Integration Time / Pixel binning	1000 ms / 2

5.2.3 LFRP Material

In order to proof the applicability of orientation analysis methods on the Co-DiCo materials mentioned in chapter 3, an orientation analysis was carried out on every LFRP material system listed in Table 3.1.

The glass fibre reinforced SMC used for orientation analysis was scanned in a region of $10 \times 10 \times 3 \text{ mm}^3$ and was manufactured with an fibre mass content of 41 wt – %. Furthermore, a discontinuous carbon fibre reinforced SMC plaque with a size of $15 \times 15 \times 3 \text{ mm}^3$ (55 wt – % CF) and a glass fibre reinforced LFT with an edge length of $10 \times 10 \times 3 \text{ mm}^3$ (30 wt – % GF) were investigated (cf. Table 3.1). In order to test the layer segmentation method introduced in section 4.1.4, a hybrid material consisting of DiCo GF SMC shell layers and unidirectional CF SMC core with an edge length of $10 \times 10 \times 3.3 \text{ mm}^3$ was examined. The corresponding image acquisition parameters for all scans are shown in table 5.4 trough 5.7.

5.2 Fibre Orientation Distribution

Table 5.4: Image acquisition parameters for GF SMC sample

Tube head	Transmission tube
Target	Tungsten
Acceleration Voltage	100 kV
Tube current	0.05 mA
Focus-object distance	21.16 mm
Focus-detector distance	723.93 mm
Voxel size	5.6 μm
Integration Time / Pixel binning	600 ms / 1

Table 5.5: Image acquisition parameters for CF SMC sample

Tube head	Transmission tube
Target	Tungsten
Acceleration Voltage	100 kV
Tube current	0.04 mA
Focus-object distance	33.15 mm
Focus-detector distance	712.01 mm
Voxel size	8.6 μm
Integration Time / Pixel binning	500 ms / 1

Table 5.6: Image acquisition parameters for Hybrid sample

Tube head	Transmission tube
Target	Tungsten
Acceleration Voltage	100 kV
Tube current	0.07 mA
Focus-object distance	21.07 mm
Focus-detector distance	724.97 mm
Voxel size	5.4 μm
Integration Time / Pixel binning	500 ms / 1

5 Experimental

Table 5.7: Image acquisition parameters for GF LFT sample

Tube head	Transmission tube
Target	Tungsten
Acceleration Voltage	100 kV
Tube current	0.04 mA
Focus-object distance	29.40 mm
Focus-detector distance	669.74 mm
Voxel size	5.4 μm
Integration Time / Pixel binning	900 ms / 2

Table 5.8: Image acquisition parameters for LFT samples

Tube head	Transmission tube
Target	Tungsten
Acceleration Voltage	100 kV
Tube current	0.05 mA
Focus-object distance	20.53 mm
Focus-detector distance	725.68 mm
Voxel size	5.3 μm
Integration Time / Pixel binning	500 ms / 1

5.3 Fibre Volume Fraction

The following tests aim for the investigation of the suitability of thresholding methods on CT scans in order to determine the fibre volume fraction of samples described in section 3.2.2. Therefore, a thermogravimetric analysis (TGA) was applied on each sample to determine the exact fibre mass fraction with respect to equation 2.37. Knowing the density of fibre and matrix material, the fibre volume content is derived from the TGA analysis using equation 2.38.

5.3.1 Thresholding Techniques for CT Images

Image Acquisition

CT scans of the LFT material were acquired using the transmission tube head with the parameters listed in table 5.8 and table 5.9.

5.4 Fibre Length Distribution and Fibre Tracking

Table 5.9: Image acquisition parameters for SMC samples

Tube head	Transmission tube
Target	Tungsten
Acceleration Voltage	100 kV
Tube current	0.05 mA
Focus-object distance	21.01 mm
Focus-detector distance	749.93 mm
Voxel size	5.4 μm
Integration Time / Pixel binning	500 ms / 1

Evaluation

The images were cropped close to the sample surface. Special attention was paid to cut a small amount of the sample to avoid to include air, which falsifies the evaluation. Subsequently, all thresholding methods introduced in section 2.3.3 were applied on the global grey value histogram. This enables to calculate the overall fibre volume fraction directly from the histogram by dividing the quantity of fibre voxels by the total amount of voxels.

5.3.2 Thermogravimetric Analysis (TGA)

Fibre volume fraction was measured by a thermogravimetric analysis using a Leco TGA701 device. The SMC specimen were heated up to 550 °C with a heating rate of 37 K/min. This temperature was held for two hours.

LFT samples were incinerated using a heating ramp from 25 °C to 100 °C at a heating rate of 15 °C/min where the temperature was held for 6 h. Subsequently, the temperature was raised to 430 °C with a heating rate of 2 °C/min and held for another 20 h.

5.4 Fibre Length Distribution and Fibre Tracking

The fibre length distribution of GF SMC material and unidirectional reinforced material can be assumed to be known initially from the manufacturing parameters. Nevertheless, a high-resolution scan was investigated in order to explore the limits of the fibre tracking method since the bundled fibres are hardly distinguishable by image processing tools. Furthermore, an injection moulded

5 Experimental

GF reinforced LFT material was investigated for validation of the fibre tracking method. The fibre lengths of the IM-LFT were measured using an optical method on incinerated samples and subsequently separated fibres. Those results are used to validate FLDs examined by the method introduced in section 4.2. Furthermore, the resulting parametrized spatial curves were used to derive orientation tensors and to compare them with voxel-based methods.

5.4.1 FibreShape FiVer

Investigation with FibreShape FiVer was carried out on LFT samples with respect to section 2.5.1 by the "Faserinstitut Bremen (FIBRE)". Samples with an edge length of 5 mm and 10 mm were investigated in a whole and only few fibres were lost. For larger samples, only a subset of the fibres, which was separated by a thinning process, was processed.

5.4.2 FASEP

The FASEP system was used to determine FLDs from the same fibres separated from LFT samples for measurement with FibreShape FiVer in order to compare both systems without an influence of the sample preparation. Therefore, the fibres were stored in small glasses and transported from Bremen to the Fraunhofer ICT in Pfinztal where the fibres were a subsample of the fibres was put back into a Petri dish for image acquisition after another thinning process.

5.4.3 μ CT Investigations

Experiments on LFRPs are carried out on an injection moulded GF LFT and a DiCo GF SMC with respect to section 3.2.3. While the IM-LFT is used for the validation of the FLD, DiCo GF SMC is processed only to prove the applicability.

IM-LFT

For CT investigations, samples with an edge length of only 5 mm and 10 mm were processed using the method based on volumetric images since the resolution of larger samples is not sufficient. Table 5.10 and table 5.11 show the image acquisition parameters of conducted scans.

5.4 Fibre Length Distribution and Fibre Tracking

Table 5.10: Image acquisition parameters for injection moulded LFT samples with an edge length of 5 mm

Tube head	Transmission tube
Target	Tungsten
Acceleration Voltage	100 kV
Tube current	0.02 mA
Focus-object distance	12.39 mm
Focus-detector distance	746.66 mm
Voxel size	3.32 μm
Integration Time / Pixel binning	1000 ms / 2

Table 5.11: Image acquisition parameters for injection moulded LFT samples with an edge length of 10 mm

Tube head	Transmission tube
Target	Tungsten
Acceleration Voltage	100 kV
Tube current	0.02 mA
Focus-object distance	21.69 mm
Focus-detector distance	746.42 mm
Voxel size	5.81 μm
Integration Time / Pixel binning	1000 ms / 2

5 Experimental

Table 5.12: Input parameters for the circular voting filtering of the IM-LFT samples with an edge length of 5 mm

Radius R	3 voxels
Window Radius m	5 voxels
Radial blurring σ_r	1 voxel
Angular blurring σ_a	1 voxel

Table 5.13: Input parameters for the circular voting filtering of the IM-LFT samples with an edge length of 10 mm

Radius R	1 voxel
Window Radius m	3 voxels
Radial blurring σ_r	1 voxel
Angular blurring σ_a	1 voxel

The circular voting filter and the fibre tracking procedure introduced in 4.2 was applied to each scan. Fibre diameters were measured from the raw grey value images in order to use derive the radius as input parameter for the circular voting filter. The window radius was set approximately to the fibre diameter. The input parameters for the investigated sample geometries are listed in table 5.12 and table 5.12 (cf. 4.7). Subsequently, the images were skeletonized using *AnalyzeSkeleton 2D/3D* and the modified *AnalyzeSkeleton* tool in *ImageJ* (cf. section 4.2.3). Resulting centre lines were saved as an ASCII file and imported in *MATLAB* for B-spline fitting.

SMC

As the fibres exist in bundles, a scan with a very high image resolution is necessary. Thus, this scan was acquired at the "Faserinstitut Bremen (FIBRE)" using a Zeiss Xradia 520 Versa X-Ray microscope. Image acquisition parameters are depicted in table 5.14. The image processing was carried out similar to the IM-LFT samples with the filter parameters shown in Table 5.15.

Fibre Length Analysis

The length of each fibre within a dataset was determined by integrating the B-spline curve numerically with respect to equation 4.17. Each fibre length is saved to a list which forms the basis for the fibre length distribution.

5.4 Fibre Length Distribution and Fibre Tracking

Table 5.14: Image acquisition parameters for FLD sample of DiCo GF SMC. The scan was carried out by the Zeiss Xradia 520 Versa X-Ray microscope.

Tube head	Transmission tube
Target	Unknown
Acceleration Voltage	80 kV
Tube current	0.088 mA
Focus-object distance	20.01 mm
Focus-detector distance	40 mm
Optical magnification	4 x
Voxel size	2.45 μm
Integration Time / Pixel binning	1000 ms / 2

Table 5.15: Input parameters for the circular voting filtering of the DiCo GF SMC samples with an edge length of 2.5 mm

Radius R	2.5 voxels
Window Radius m	4 voxels
Radial blurring σ_r	1 voxel
Angular blurring σ_a	1 voxel

Curvature Analysis

Fibre curvatures were determined by re-parametrising the B-spline curves. Therefore, the Frenet-Serret equations 4.20 through 4.22 were applied to derive the local curvature $\kappa(s)$ directly from the parametrization. Subsequently, a weight related histogram is generated to depict the mean curvature of all fibres within the image. For The LFT-Material, a second diagram is shown to visualize the fibre curvature over fibre length. This makes only sense for the IM-LFT material since all of the SMC fibres are already cropped by the sample preparation.

Fibre Orientation Tensors

In order to compare the fibre tracking approach with voxel-based orientation analysis methods, orientation tensors of second order were derived from spatial curves using equation 4.18. The result was compared to the structure tensor based method by evaluating the error E_T with respect to equation 4.3.

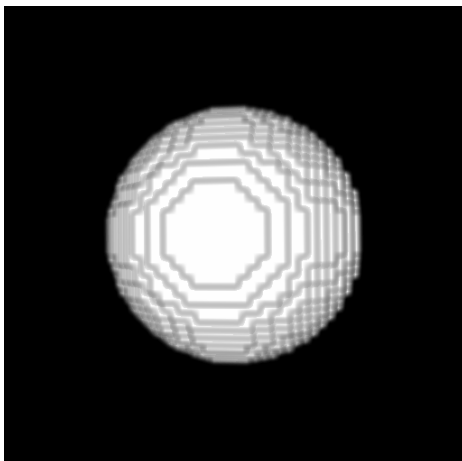


Figure 5.4: Artificially generated sphere for validation of curvature analysis [90].

5.5 Surface Curvature Analysis

5.5.1 Artificial Images

Artificial images of spheres were generated as mentioned in section 4.3.2 for parameter optimization and error estimation of both algorithms investigated. Figure 5.4 shows an example of an artificial sphere in 3D. Those structures were generated with diameters from 2 voxels through 20 voxels in steps of 2 voxels to investigate the influence of the radius of the structure. Subsequently, the method based on the Hessian matrix was applied with blurring parameter of $\sigma = \{0.6, 0.8, 1, 2, 4, 6\}$ voxels. The patch-based method was applied on images with the same radius using a patch size of $\rho = \{1, 2, \dots, 10\}$ voxels and blurring parameter $\sigma = \{0.6, 0.8, 1, 2, 4, 6\}$ voxels.

5.5.2 Real Images with known Curvature

As a reference sample for validating surface curvature algorithms, steel balls from a ball bearing were scanned (cf. Fig. 3.9). The CT scan was acquired with the reflection head and the parameters shown in table 5.16.

Table 5.16: Image acquisition parameters for steel balls extracted from ball-bearings

Tube head	Reflection tube
Target	Tungsten
Acceleration Voltage	180 kV
Tube current	0.11 mA
Focus-object distance	60.98 mm
Focus-detector distance	799.86 mm
Voxel size	14.77 μm
Integration Time / Pixel binning	600 ms / 1

Table 5.17: Image acquisition parameters for porous CFRP-layup shown in figure 3.10

Tube head	Transmission tube
Target	Tungsten
Acceleration Voltage	110 kV
Tube current	0.02 mA
Focus-object distance	24.89 mm
Focus-detector distance	803.6 mm
Voxel size	6.19 μm
Integration Time / Pixel binning	1000 ms / 2

5.5.3 Pore Analysis on Continuous CFRP

In order to derive a local surface curvature from pores, a continuous CFRP-layup made of a PA6 matrix shown in figure 3.10 was scanned and evaluated using the method based on the Hessian matrix with an blurring parameter of $\sigma = 2$ voxels.

6 Results

6.1 Fibre Orientation Distribution

The results regarding orientation analysis within this chapter have partially been published in NDT&E International [46].

Within this chapter, results from three investigated orientation analysis methods based on the anisotropic Gaussian filtering, the Hessian matrix and the structure tensor are presented. Each method was evaluated on artificial images with only one or two fibres, artificial microstructures from GeoDict[®] and two real μ -CT-scans for validation.

6.1.1 Artificial Images with One and Two Fibres

Anisotropic Gaussian Filter

First tests on single fibres with a diameter of 10 voxels using the anisotropic Gaussian filter with varying aspect ratio α and blurring parameter σ show a decreasing error θ_{gE} (cf. Eq. 4.1) for increasing aspect ratios (Fig.6.1) Also a high blurring parameter σ lowers the error to 5.21° at $\alpha = \sigma = 10$ voxels.

The aspect ratio for anisotropic Gaussian filtering was $\alpha = 2$ for the following investigations. Figure 6.2 (left) depicts the error measure using an artificial image with two fibres of 10 voxels in diameter. The minimum error of $E_A = 8.19^\circ$ is located at a blurring parameter of $\sigma = 6$ voxels. At a fibre diameter of 5 voxels, Fig. 6.2 (right) shows that best results with an error of $E_A = 8.42^\circ$ can be achieved using a blurring parameter $\sigma = 3$ voxels.

6 Results

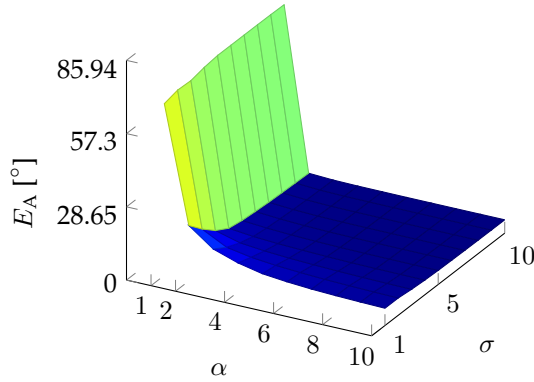


Figure 6.1: Anisotropic Gaussian filter: Error measure E_A over aspect ratio α and blurring parameter σ on an artificial single fibre of 10 voxels diameter [46].

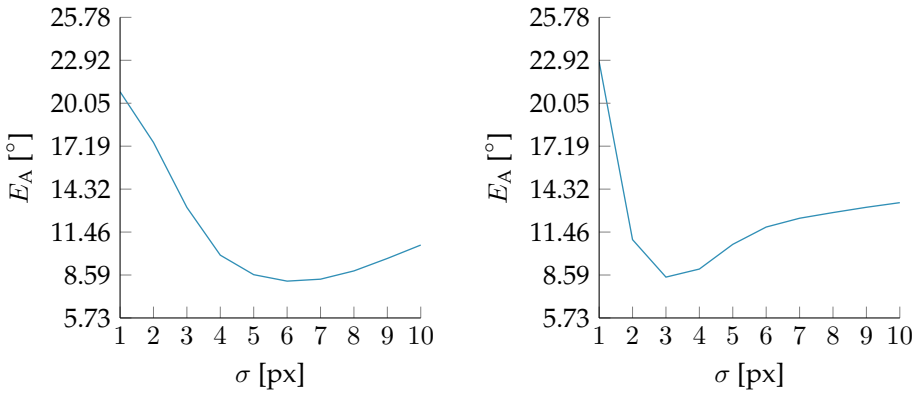


Figure 6.2: Anisotropic Gaussian filter: Fibre architecture dependent error E_A over blurring parameter σ on an artificial image with two fibres. Left: Fibres with 10 voxels in diameter. Right: Fibres with 5 voxels in diameter [46].

Hessian Matrix

Figure 6.3 through 6.4 show curves of the error E_A using the Hessian matrix based method on single fibres of diameters of 5, 10 and 15 voxels. While the curve for a diameter of 5 voxels shows a steadily falling graph, there is a peak at a blurring parameter of $\sigma = 3$ voxels in the curve for a fibre diameter of 10 voxels. A similar peak is located at $\sigma = 4$ voxels investigation a fibre diameter of 15 voxels.

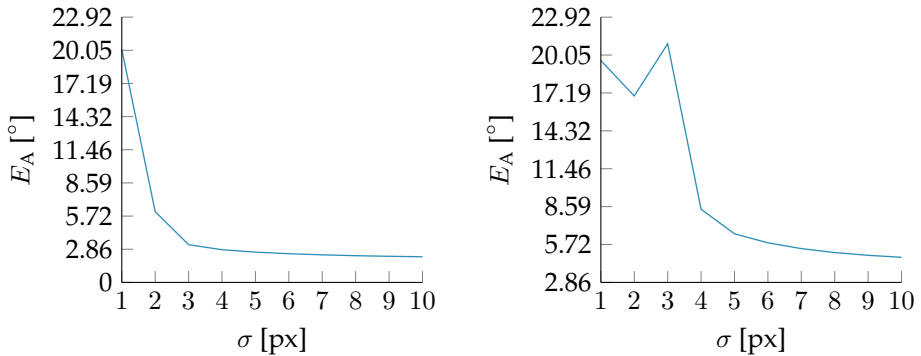


Figure 6.3: Hessian matrix: Error measure E_A over blurring parameter σ for an artificial single fibre of 5 voxels in diameter (left) and 10 voxels (right).

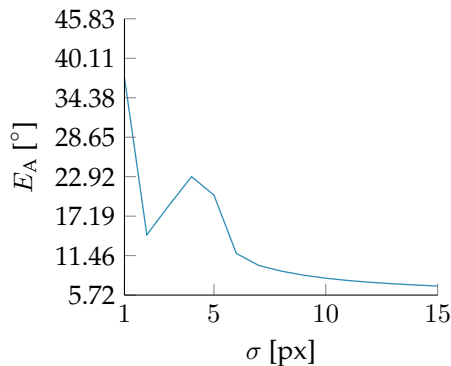


Figure 6.4: Hessian matrix: Error measure E_A over blurring parameter σ for an artificial single fibre of 15 voxels in diameter.

6 Results

The error achieved with the Hessian matrix on images with two fibres are shown in Fig. 6.5 for a fibre diameter of 10 voxels. The curve shows a peak at $\sigma = 3$ voxels and drops to a minimum value of 10.2° at $\sigma = 6$ voxels. Up from that point, the error increases with σ .

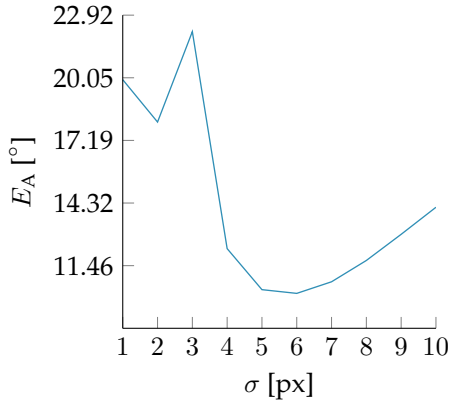


Figure 6.5: Hessian matrix: Fibre architecture dependent error E_A over blurring parameter σ on artificial images with two fibres of 10 voxels in diameter [46].

For fibre diameters of 5 voxels, the minimum fibre architecture dependent error is located at $\sigma = 3$ voxels with 10.31° (Fig. 6.6 left). For higher blurring parameters σ , the error rises to a maximum of 17.48° at $\sigma = 8$ voxels, where it starts to fall slightly to $\sigma = 10$ voxels, which is the last point investigated. Because of the sharp minimum, results are shown in Fig. 6.6 on the right with a finer resolution within a range of $2.5 \leq \sigma \leq 3.5$. In the higher resolution graph, the lowest error of $E_A = 10.31^\circ$ at $\sigma = 2.9$ voxels.

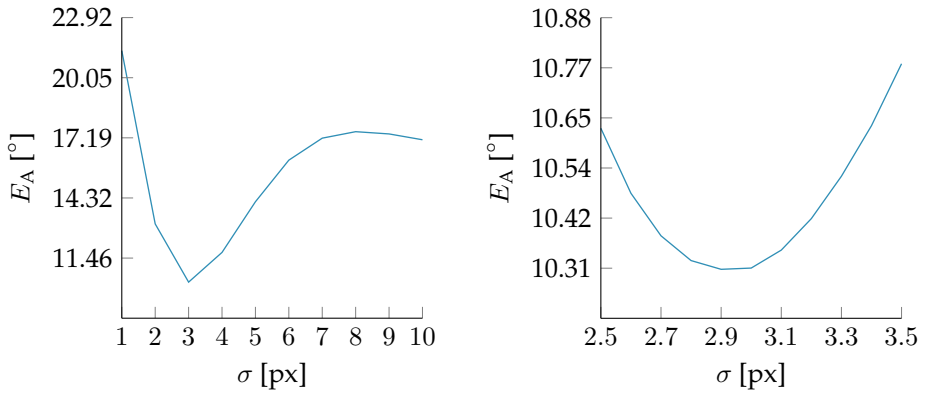


Figure 6.6: Hessian matrix: Fibre architecture dependent error E_A over blurring parameter σ on artificial images with two fibres of 5 voxels in diameter. Left: Coarse sampling. Right: Fine sampling on the same input data at the interesting range of σ [46].

6 Results

Structure Tensor

Tests with single fibres are illustrated in Figure 6.7. The error E_A shows no local minimum in the investigated interval and decreases to 0.36° at $\sigma = 1$ voxel and $\rho = 10$ voxels.

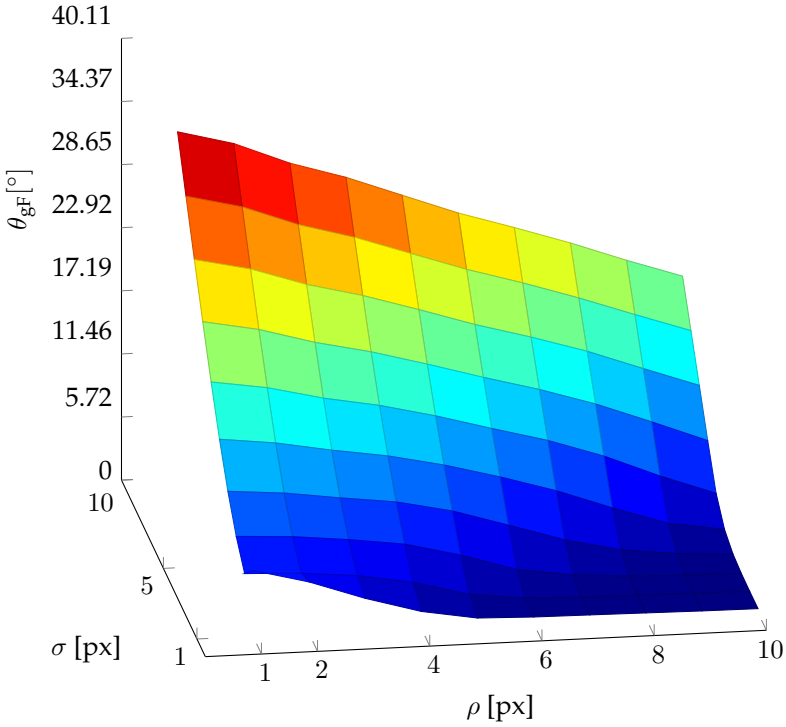


Figure 6.7: Structure tensor: Error measure E_A over blurring parameters σ and ρ on an artificial single fibre of 5 voxels diameter.

Artificial images with two fibres and a diameter of 10 voxels lead to a minimum at $\sigma = 1$ voxel and $\rho = 6$ voxels. Figure 6.8 shows the resulting function in a contour plot. The point with optimal parameters is marked by a red dot. The fibre architecture dependent error is $E_A = 1.66^\circ$.

6.1 Fibre Orientation Distribution

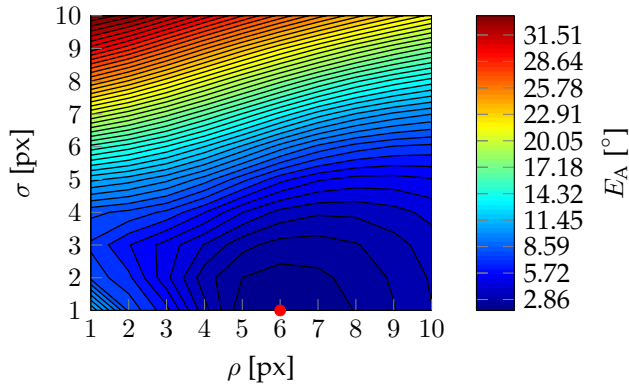


Figure 6.8: Structure tensor: Error measure E_A over blurring parameters σ and ρ on artificial images with two fibres of 10 voxels diameter [46].

As the optimal parameters are located on the edge in Figure 6.8, a smaller range of the parameter space was examined using a higher resolution. Figure 6.9 shows that there is a local minimum at $\sigma = 0.8$ voxels and $\rho = 5.6$ voxels leading to an error of $E_A = 2.18^\circ$.

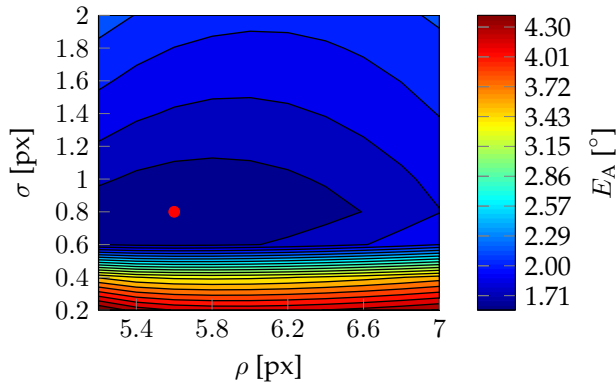


Figure 6.9: Structure tensor: Error measure E_A over blurring parameters σ and ρ on artificial images with two fibres of 10 voxels diameter with high resolution [46].

Similar investigations on fibres with a diameter of 5 voxels and a length of 40 voxels show an optimum at $\sigma = 0.8$ voxels and $\rho = 3$ voxels (Fig. 6.10). The

6 Results

error E_A is 1.60° on this point. Increasing the fibre length to 80 voxels leads to Figure 6.11. The minimum is located at the same set of parameters and the error drops slightly to 1.23° . Also rotating the same fibre configurations to an initial angle of 45° instead of 20° for the other investigations results in the same optimal parameters but an error of 2.01° (Figure 6.12).

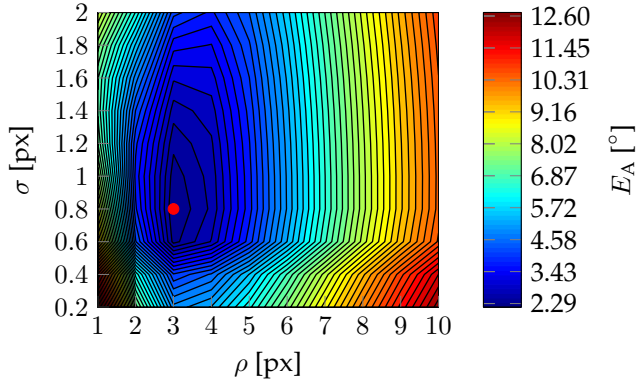


Figure 6.10: Structure tensor: Error measure E_A over blurring parameters σ and ρ on artificial images with two fibres of 5 voxels diameter [46].

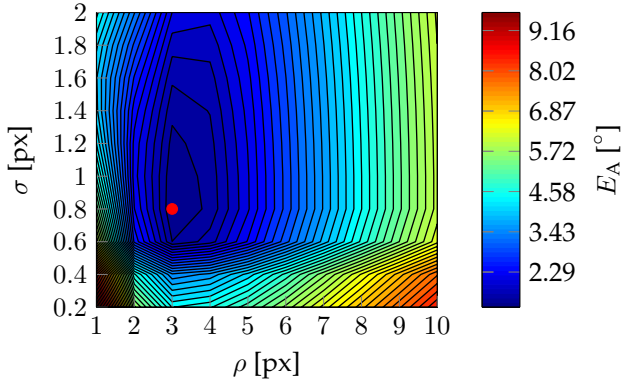


Figure 6.11: Structure tensor: Error measure E_A over blurring parameters σ and ρ on artificial images with two fibres of 5 voxels diameter and 80 voxels length.

6.1 Fibre Orientation Distribution

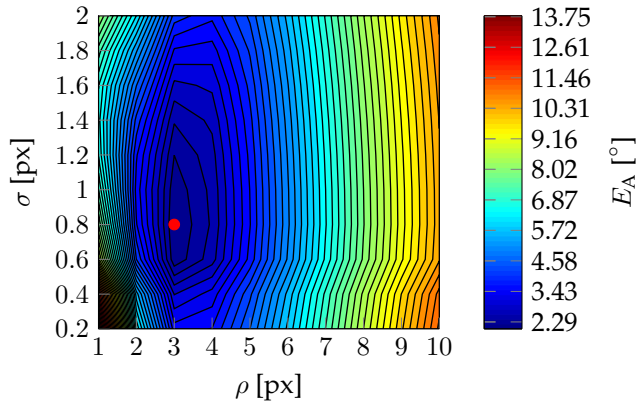


Figure 6.12: Structure tensor: Error measure E_A over blurring parameters σ and ρ on artificial images with two fibres of 5 voxels diameter.

Considering fibres of 15 voxels in diameter results in the error surface shown in Figure 6.13. Optimal parameters are found at $\sigma = 0.8$ voxels and $\rho = 8$ voxels with $E_A = 1.95^\circ$.

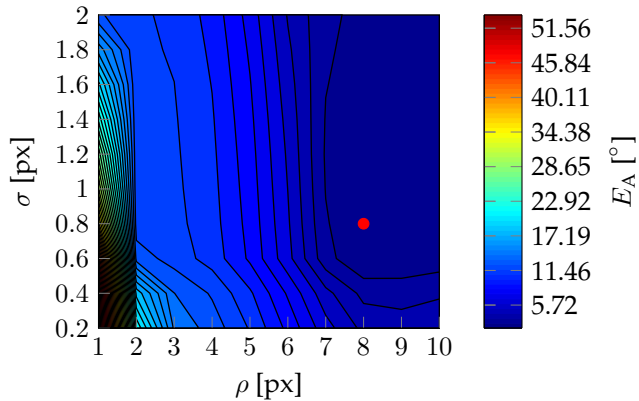


Figure 6.13: Structure tensor: Error measure E_A over blurring parameters σ and ρ on artificial images with two fibres of 15 voxels diameter.

6.1.2 Evaluation of GeoDict[®] Structures

Investigations on artificial fibre architectures generated by GeoDict[®] lead to an tensor-based error E_T listed in table 6.1 and visualised in Figure 6.14. The structure tensor results in the lowest error for most of the configurations using straight fibres except for a fibre volume content of 13 %, where the method based on the anisotropic Gaussian filter shows a slightly better performance. Anisotropic Gaussian filtering and the Hessian matrix lead to a relatively high error for structures with a high volume content of 20 %. Investigations on curved fibres result in the highest error using the anisotropic Gaussian filter and the most precise evaluation with the Hessian matrix.

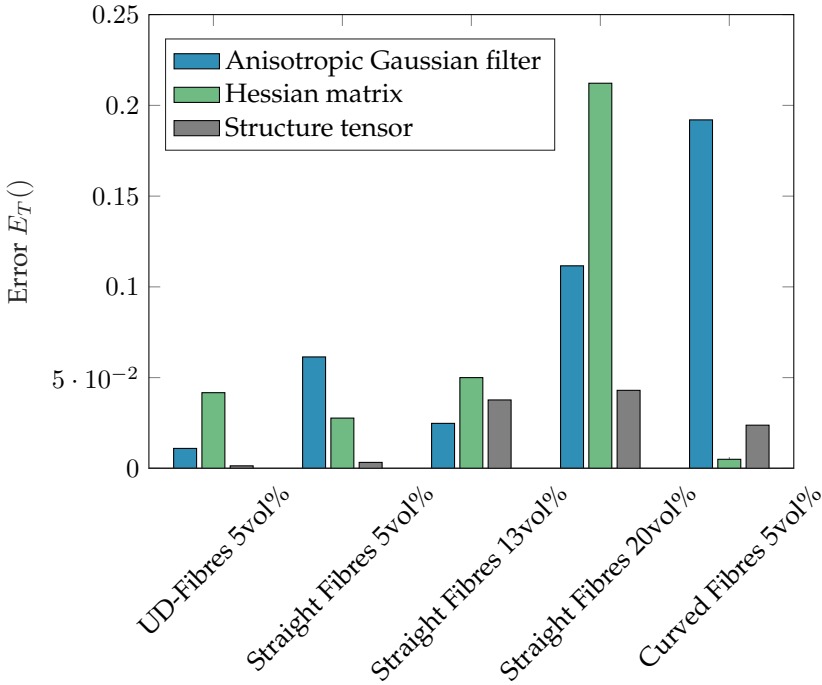


Figure 6.14: Error E_T resulting from artificial GeoDict[®] images.

Computation times and memory consumption for the artificial structures with a size of 500^3 voxels and a bit depth of 16 bit are listed in table 6.2. For larger images, time scales nearly linear with the image size. Calculations were carried out on a 16-core Intel Xeon E5-2620 v4 workstation with 256 GB RAM.

Table 6.1: Error E_T of artificial images from GeoDict[®].

Method	UD-Fibres 5 vol %	Straight Fibres 5 vol %	Straight Fibres 13 vol %	Straight Fibres 20 vol %	Curved Fibres 5 vol %
Anisotropic Gaussian filter	0.0110	0.0614	0.0248	0.1116	0.1920
Hessian matrix	0.0417	0.0277	0.0500	0.2122	0.0050
Structure tensor	0.0014	0.0033	0.0377	0.0430	0.0238

Table 6.2: Computation times and memory consumption for artificial images with a size of 500^3 voxels and a bit depth of 16 bit.

Method	Computation time	Memory consumption
Anisotropic Gaussian Filter	16 min 40 s	6 GB
Hessian matrix	1 min 58 s	8 GB
Structure tensor	2 min 2 s	8 GB

6.1.3 Real Images with known Orientation

Orientation analysis using the three investigated methods on real CT-scans of 3D printed fibre reinforced polymers resulted in orientation tensors shown in Table 6.3. All investigated methods result in orientation tensors with a N_{xx} component that is close to one.

Table 6.3: Orientation Tensors derived from 3D-printed glass fibre reinforced specimen.

Anisotropic Gaussian filter N_G	0.9204	0.0106	0.0036
	0.0106	0.0360	0.0001
	0.0036	0.0001	0.0436
Hessian matrix N_H	0.9270	-0.0013	0.0145
	-0.0013	0.0311	0.0006
	0.0145	0.0006	0.0419
Structure tensor N_{ST}	0.9658	-0.0019	0.0207
	-0.0019	0.0069	0.0002
	0.0207	0.0002	0.0273

Investigations on unidirectional carbon fibre reinforced polymers are illustrated in Table 6.4. Assessing the trace of the tensors, the methods based on the anisotropic Gaussian filter and the Hessian matrix show no preferred orien-

6 Results

tation. The algorithms based on the structure tensor leads to an orientation tensor with N_{xx} close to one.

Table 6.4: Orientation Tensors derived from unidirectional carbon fibre reinforced polymer rod.

Anisotropic Gaussian filter N_G	0.3460	-0.0003	-0.0072
	-0.0003	0.3572	-0.0024
	-0.0072	-0.0024	0.2968
Hessian matrix N_H	0.2588	0.0002	0.0000
	0.0002	0.3720	0.0052
	0.0000	0.0052	0.3693
Structure tensor N_{ST}	0.9977	-0.0039	0.0009
	-0.0039	0.0011	0.0002
	0.0009	0.0002	0.0012

6.1.4 LFRP Material

GF SMC

Figure 6.15 shows an orientation analysis on a sample made of glass fibre reinforced SMC material. The upper image depicts the raw grey level image while the lower one shows the orientations in HSV colour space.

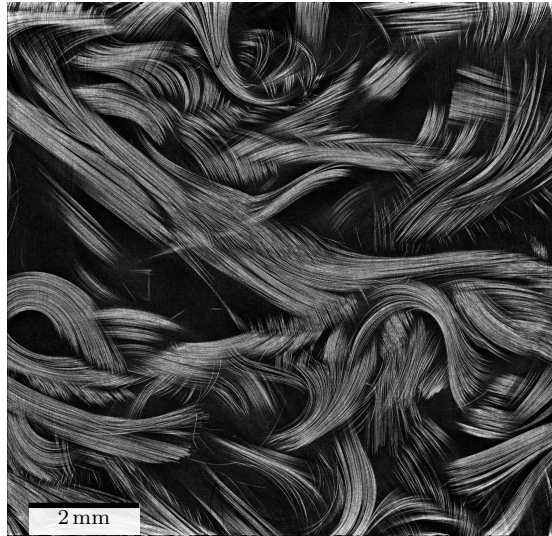
CF SMC

An orientation analysis on carbon fibre reinforced SMC is shown in figure 6.16. As the grey value threshold for fibre segmentation was set to zero, there is an orientation calculated in every voxel.

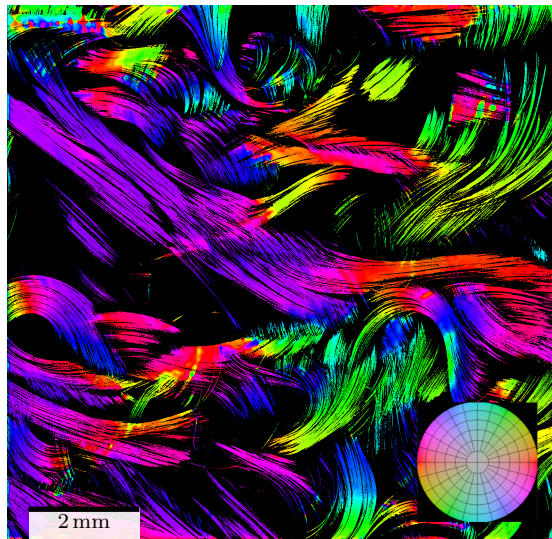
GF LFT

Long fibre reinforced thermoplastics with glass fibres are shown in figure 6.17. Most fibre rovings are fallen apart and there are more single fibres within the image.

6.1 Fibre Orientation Distribution



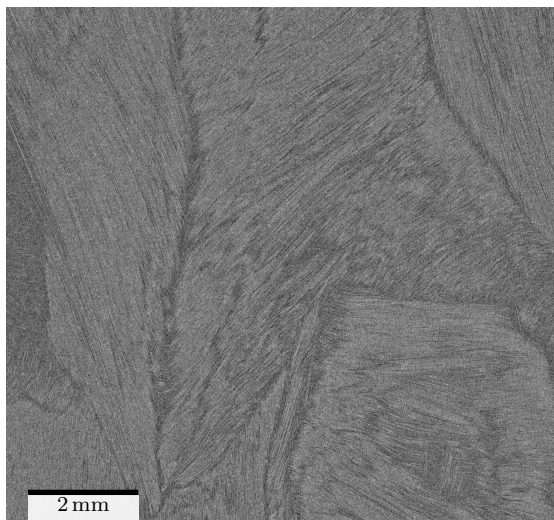
(a) Raw Data



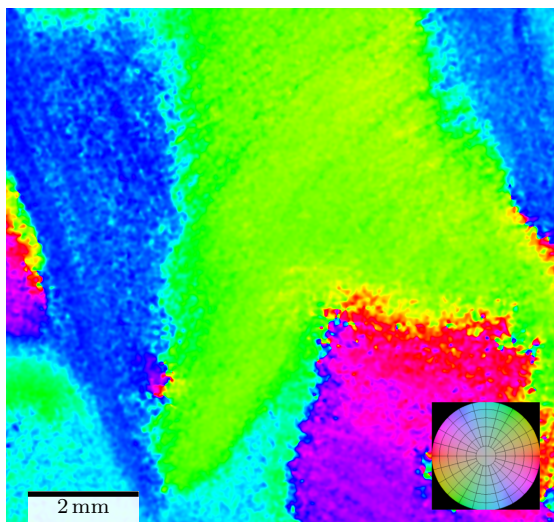
(b) Orientation Analysis

Figure 6.15: Orientation Analysis on GF SMC material using the structure tensor based method. Fibre orientations are coded by colour in HSV colour space.

6 Results



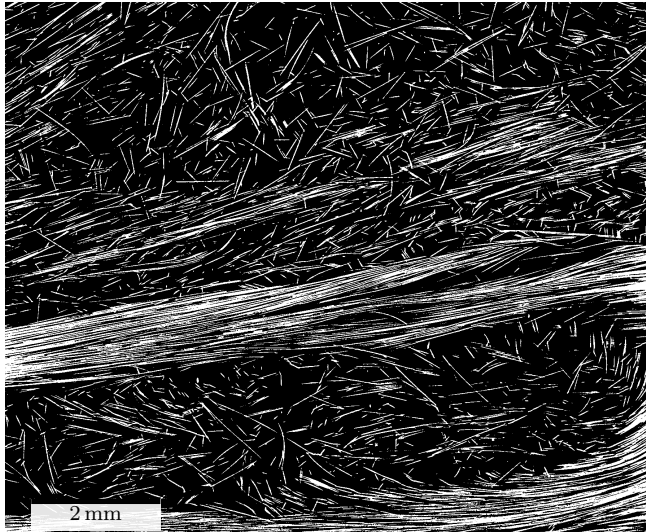
(a) Raw Data



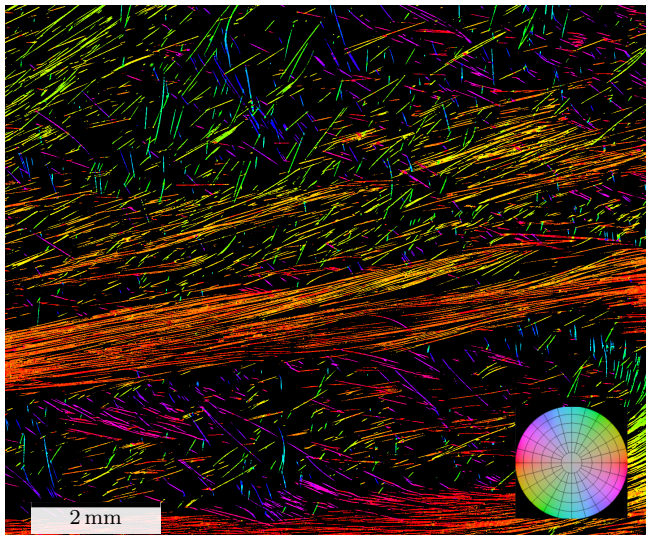
(b) Orientation analysis

Figure 6.16: Orientation analysis on CF SMC material using the structure tensor based method. Fibre orientations are coded by colour in HSV colour space.

6.1 Fibre Orientation Distribution



(a) Raw Data



(b) Orientation analysis

Figure 6.17: Orientation analysis on GF LFT material using the structure tensor based method. Fibre orientations are coded by colour in HSV colour space.

Hybrid Sample

The hybrid sample was processed using the structure tensor first. Subsequently, the coherence measure was carried out in order to separate GF SMC material from CF UD material. Orientation analysis on the SMC looks similar to the bulk material, that was investigated. The carbon fibre reinforced material includes some fixation strings made of glass fibres for holding the carbon fibres in place during the manufacturing process. Those fibres are aligned 90 degree to the CF fibre direction and are clearly visible within the scan (Fig. 6.19 (a)). The side view of the same image illustrates the fibre orientations through the layers: The SMC shell shows different rovings with arbitrary orientation while the unidirectional carbon fibre reinforced core appears mainly in red due to its x-alignment. Note that it is not possible to separate the matrix material from the fibres because of the low contrast between carbon fibre and matrix while the contrast to glass fibre is very high. Figure 6.18 shows the results of the coherence measure (cf. section 4.1.4) over thickness direction. The curve is very noisy but it shows a significantly higher signal at the core layer made of the unidirectional material.

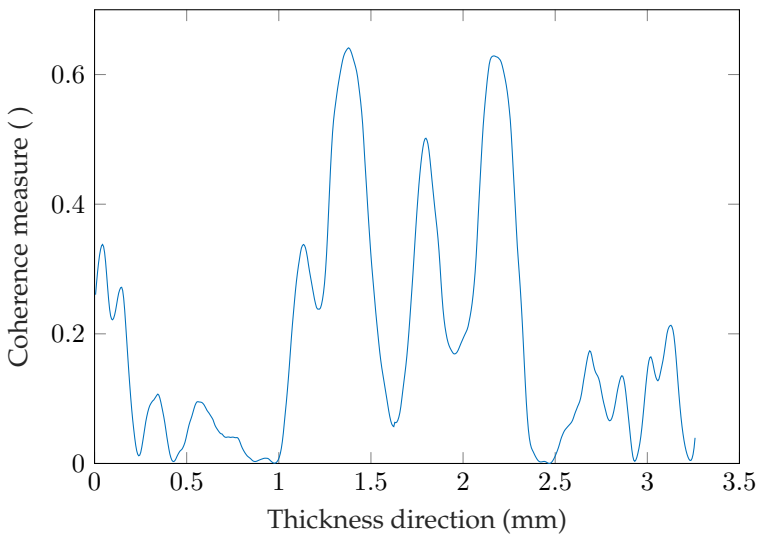


Figure 6.18: Coherence measure over plate thickness direction for layer segmentation.

6.1 Fibre Orientation Distribution

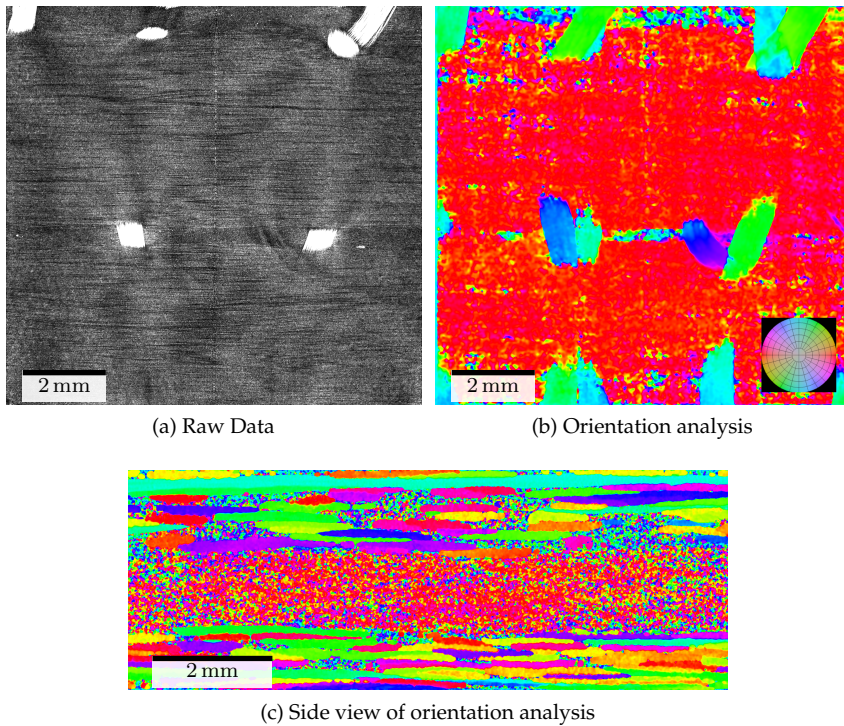


Figure 6.19: Orientation analysis on hybrid specimen within the unidirectional CF including fixation strings made from glass fibres region using the structure tensor based method. Fibre orientations are coded by colour in HSV colour space (b). Note that the colours of the side view correspond to the colour wheel in the top view.

6.2 Fibre Volume Fraction

The following chapter illustrates results from fibre mass and fibre volume measurements using conventional methods like TGA and thresholding techniques on μ CT images. Mass fractions of TGA investigations are converted to volume fractions for a better comparability.

6.2.1 Thermogravimetric Analysis (TGA)

Fibre mass contents for SMC material examined by TGA are shown in Table 6.5. The fibre distribution is almost homogeneous expect for sample 2B.90.2, which was cropped from the edge of a plate (cf. Fig. 3.8).

Table 6.5: Fibre content of SMC samples determined by TGA.

	2A.0.1	2B.0.1	2C.90.2	2D.90.2
Fibre weight Content	45.33 wt %	40.85 wt %	44.82 wt %	43.70 wt %
Fibre volume Content (calculated)	27.44 vol %	23.95 vol %	27.03 vol %	26.14 vol %

Table 6.6 shows fibre mass fractions for investigated LFT samples. The deviation of the mass fraction up to 2.6 % for LFT with 10 % glass fibres with respect to the specification of the manufacturer. This deviation gets smaller for higher fibre mass fractions at 20 % and 30 %.

Table 6.6: Fibre content of LFT samples determined by TGA.

	PP LFT 10 % GF	PP LFT 20 % GF	PP LFT 30 % GF
Fibre weight Content	12.6 wt %	21.68 wt %	28.84 wt %
Fibre volume Content (calculated)	5.19 vol %	9.52 vol %	13.35 vol %

6.2.2 Thresholding Techniques on CT Images

Application of thresholding methods on LFT samples lead to the fibre volume contents shown in Fig. 6.20. The methods of *Shanbhag* and *Intermodes* lead to a significant underestimation of the fibre volume and *Minimum* did not converge. *Percentile*, which should show values of 50 vol %, resulted in 47 vol % to 54 vol %. *Triangle*, *MinError*, *Mean*, *Li* and *Huang* led to an overestimation of

6.2 Fibre Volume Fraction

6 vol % to 12 vol %. *Renyi Entropy* and *MaxEntropy* are close to the real fibre volume fractions with an maximum error of 3.5 vol %. Latter methods did not result in a general over or underestimation. The methods *IJ_IsoData*, *Moments* and *Otsu* predicted the most precise data with a deviation lower than 1.1 vol %, where *Otsu* and *IJ_IsoData* showed an almost constant overestimation.

Results of thresholding investigations on SMC material are illustrated in Figure 6.21. *Triangle*, *MinError*, *Mean*, *Li*, *Intermodes* and *Huang* resulted in a significant over-prediction of fibre volume content. *Percentile*, which should result in a volume fraction of 50 vol %, had a maximum deviation of 0.6 vol %. Methods by *Shanbhag* and *MaxEntropy* tend to under-predict the volume fraction of GF SMC. *IJ_IsoData*, *Minimum* and *Otsu* led to values around 5 vol % higher than the reference measures. *Renyi Entropy* ended up in the right range, but the volume fractions of the samples are almost random within this interval. *Moments* offered the closest results on GF SMC material with an maximum deviation of 1.2 vol %.

6 Results

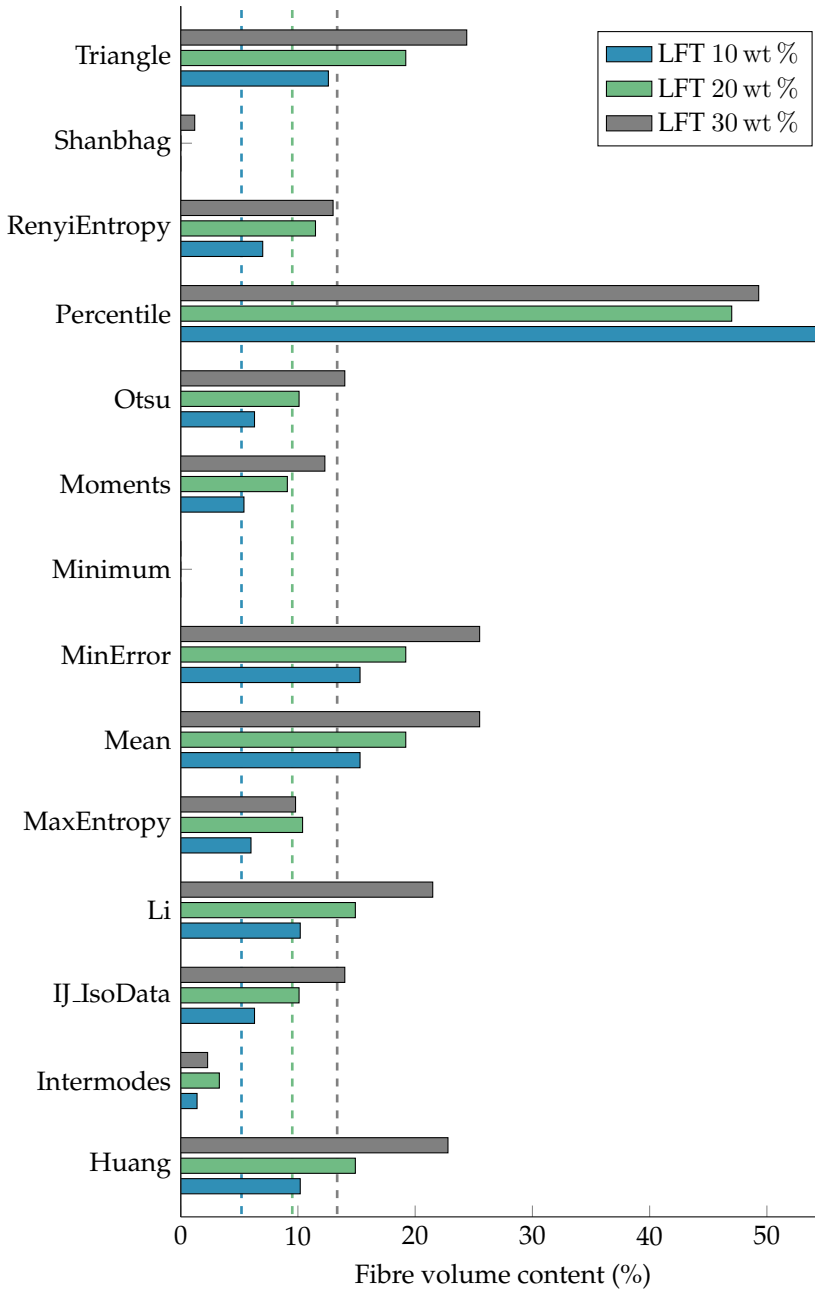


Figure 6.20: Fibre volume fractions of GF LFT determined by different histogram based thresholding techniques. Dashed lines illustrate reference values from TGA measurements.

6.2 Fibre Volume Fraction

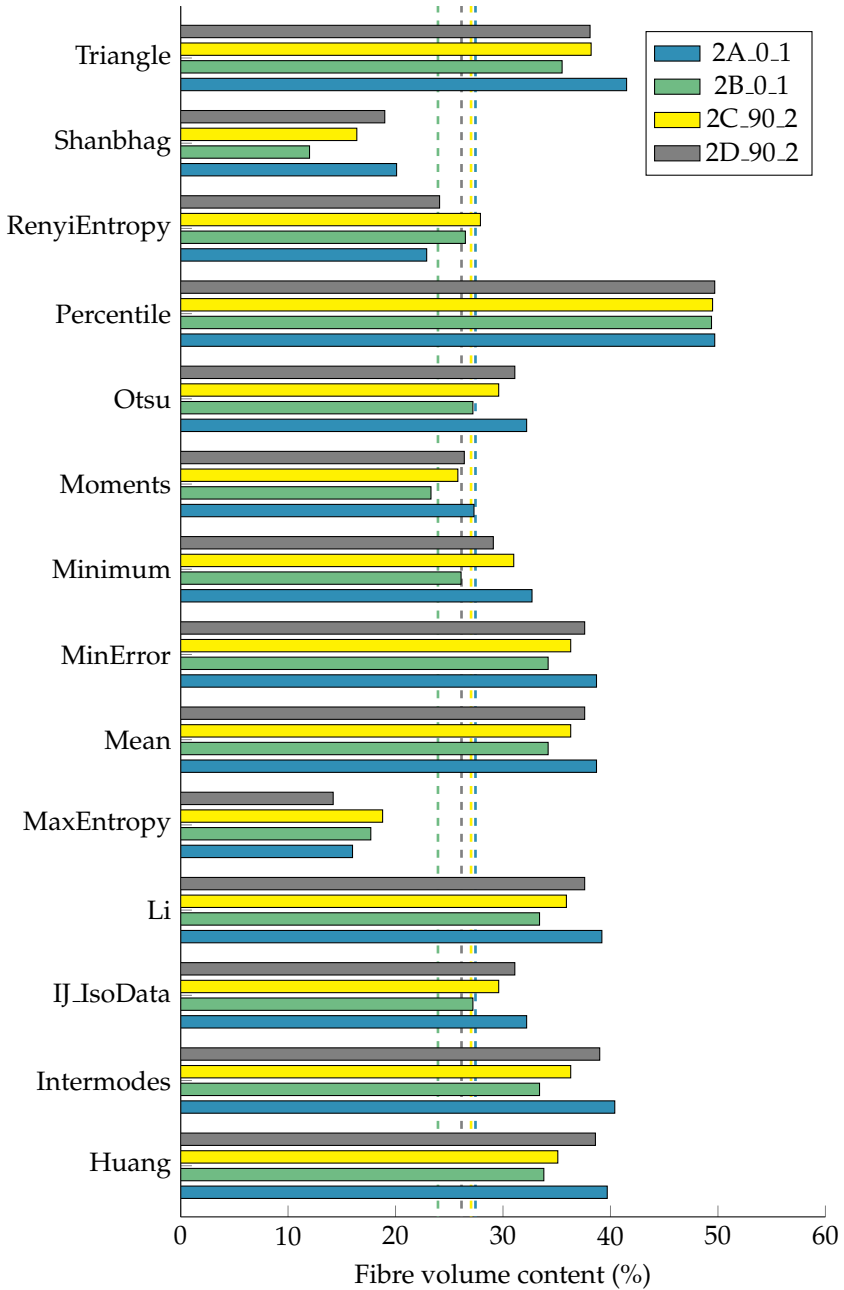


Figure 6.21: Fibre volume fractions of GF SMC determined by different histogram based thresholding techniques. Dashed lines illustrate reference values from TGA measurements.

6.3 Fibre Length Distribution

6.3.1 FibreShape FiVer

Fibre length analysis examined by FiVer are illustrated in Figure 6.22 for LFT samples of different sizes cut from the IM-LFT plate. Both curves for samples with an edge length of 5 mm and 10 mm show their peak value at 0.65 mm while the 10 mm curve is shifted slightly to the right at higher fibre lengths. Measurements on samples with an edge length of 20 mm lead to a peak at 0.85 mm and samples of 40 mm to 0.65 mm. Both curves for larger samples are significantly shifted to higher fibre lengths while the 20 mm curve remains on the right of the 40 mm curve for most of the progression.

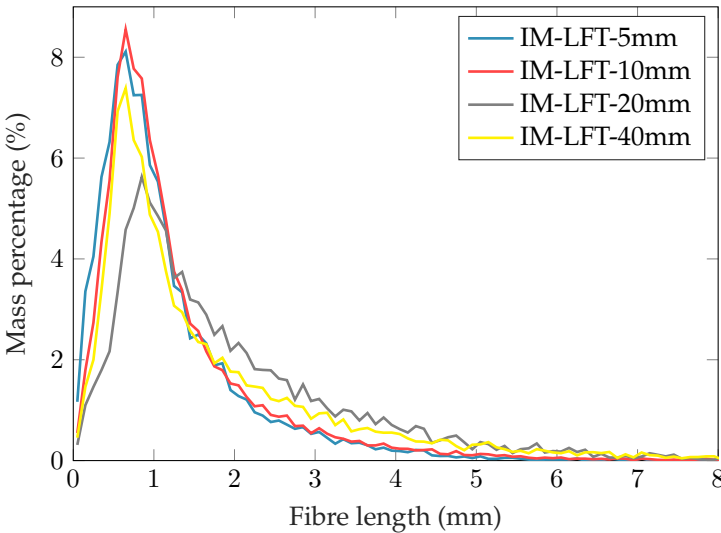


Figure 6.22: Fibre length distribution for samples of all sizes from the IM-LFT plate measured by FiVer.

6.3.2 FASEP

Results from fibre length measurements on the injection moulded LFT material using the FASEP system are depicted in Figure 6.23. Peak values for samples with a size of 5 mm are at 0.7 mm and 0.8 mm for the 10 mm sample, where the smaller sample size led to another lower peak value at 0.2 mm. Results of larger

samples with an edge length of 20 mm and 40 mm, where only a subset of the fibres was investigated, ended up at the same peak value of 0.8 mm. The 20 mm sample shows a higher fibre mass percentage between the peak and approximately 3 mm fibre length while the mass fraction of longer fibres is higher for the 40 mm sample.

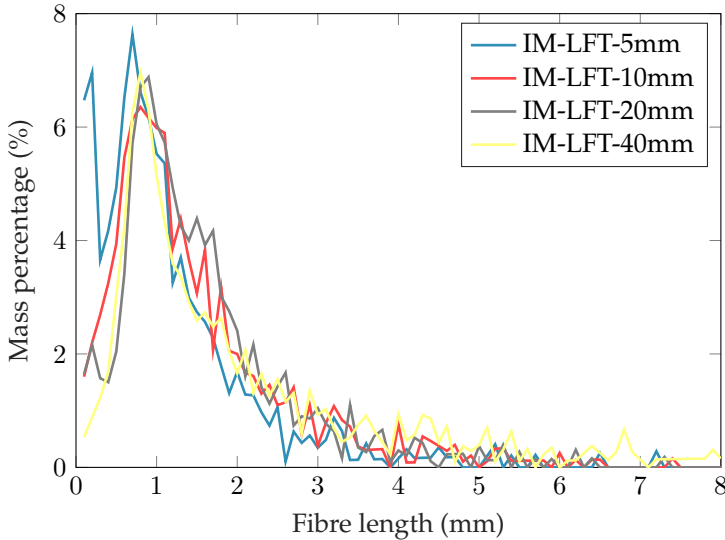


Figure 6.23: Fibre length distribution for samples of all sizes from the IM-LFT plate measured by FASEP.

6.4 Fibre Tracking in CT Images

The following section shows results that are derived from fibre tracking algorithms and comparing measurements from conventional methods if available.

6.4.1 Fibre Length Analysis

IM-LFT

Fibre length measurements on the injection moulded LFT material are depicted in Figure 6.24 for a sample size of 5 mm and 10 mm. All histograms are weighted

6 Results

by mass and are built with a bin width of 0.1 mm using 100 samples to 10 mm. The peak values of the length distribution is 0.7 mm for the sample with an edge length of 5 mm and 0.5 mm for the 10 mm specimen. Long fibres up from 2 mm occur more frequently in the smaller sample size, while more short fibres were found in the 10 mm sample.

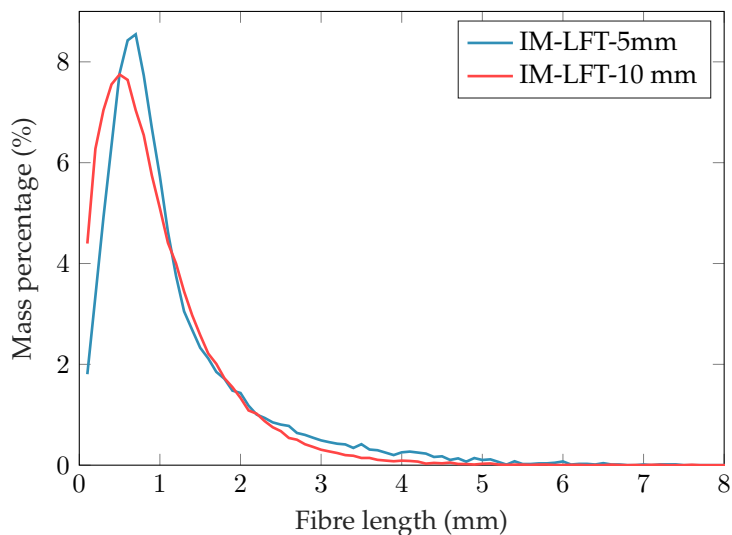


Figure 6.24: Fibre length distributions of two samples cropped from the IM-LFT plate with an edge length of 5 mm and 10 mm.

DiCo GF SMC

Fibre length analysis on the DiCo GF SMC sample with a scanned size of only 2.5 mm shows many very short fibres of approximately 0.1 mm length. Two more peaks can be found at a length of 1.75 mm and 2.25 mm before the curve drops to almost zero at 2.5 mm.

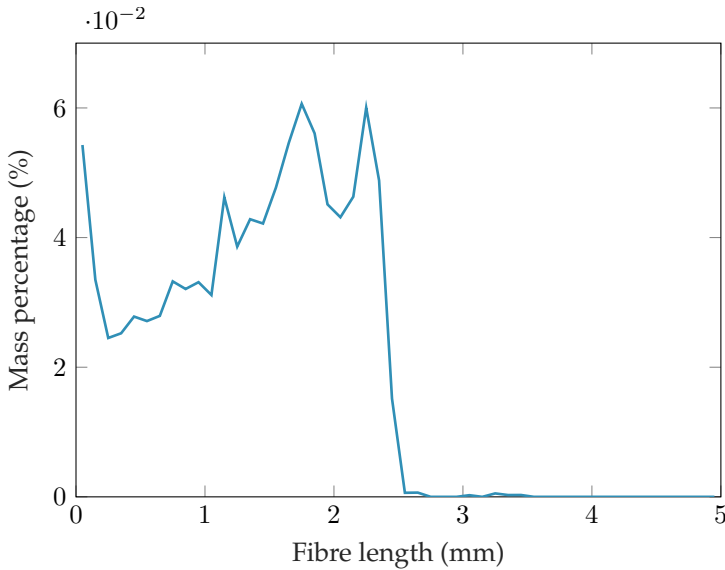


Figure 6.25: Fibre length distributions of the DiCoGF SMC sample with a scanned size of 2.5 mm.

6.4.2 Curvature Analysis

IM-LFT

Figure 6.26 shows the bending radius of each fibre over length as a dot in a heat map for the IM-LFT sample with an edge length of 5 mm. The point cloud underlying this heat map is very scattered for smaller fibre lengths and gets sharper for higher values. Very long fibres up from 5 mm seem to converge against a bending radius of around one.

Building a mass-weighted curvature histogram from the same data leads to Fig. 6.27. The peak value for the bending radius is found at 1.45 mm. Furthermore, there is a small peak at small bending radius of 0.15 mm.

DiCo GF SMC

Figure 6.28 shows the fibre curvature histogram of an the DiCo GF SMC sample with an edge length of 2.5 mm.

6 Results

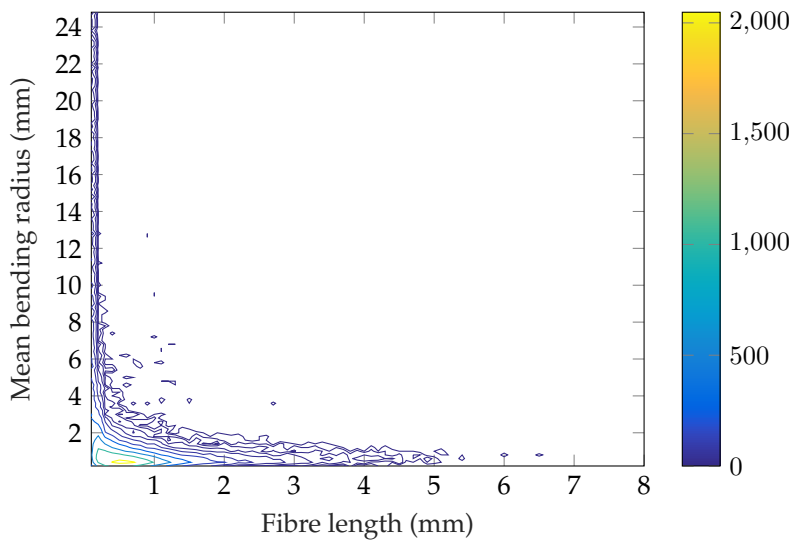


Figure 6.26: Heatmap of fibre bending radius over fibre length including all fibres within the IM-LFT sample with an edge length of 5 mm.

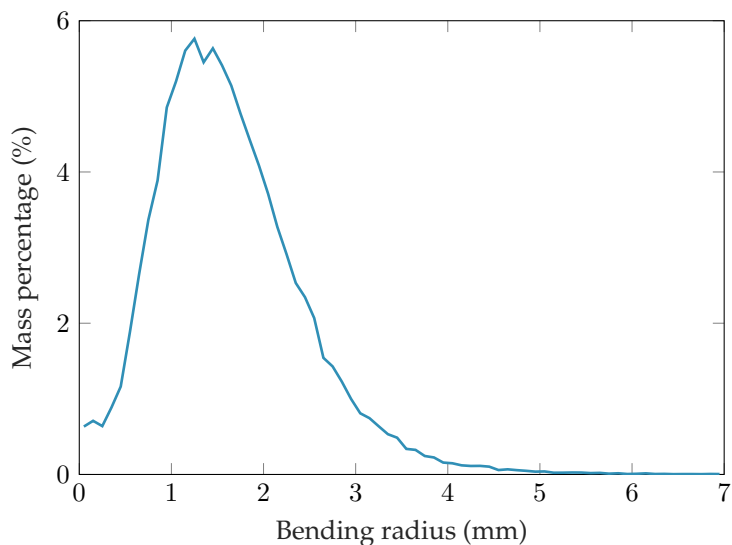


Figure 6.27: Mass percentage over fibre curvatures of the IM-LFT sample.

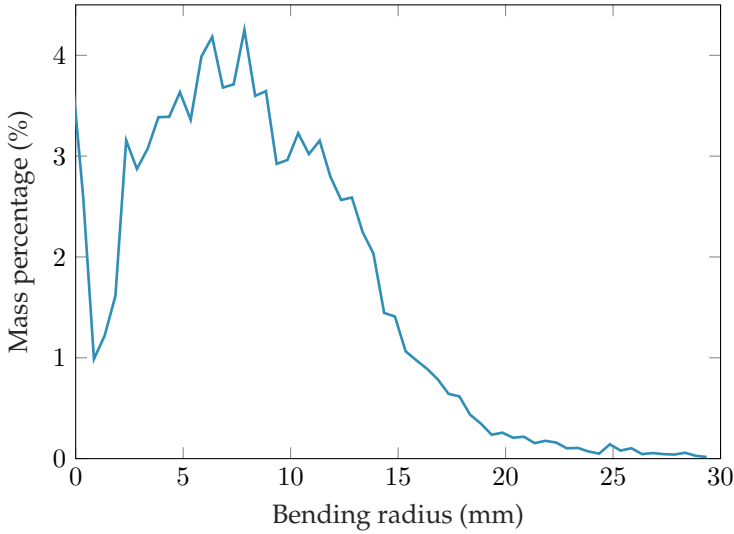


Figure 6.28: Mass percentage over fibre curvatures of the DiCo GF SMC sample with an scanned size of 2.5 mm.

6.4.3 Fibre Orientation Tensors

Fibre orientation tensors derived from spatial curves \mathbf{N}_{sc} and from voxel-based methods \mathbf{N}_{vol} are listed in the following for the IM-LFT sample with an edge length of 5 mm.

$$\mathbf{N}_{vol} = \begin{bmatrix} 0.0318 & 0.0267 & -0.0050 \\ 0.0267 & 0.6926 & -0.0123 \\ -0.0050 & -0.0123 & 0.2756 \end{bmatrix}, \mathbf{N}_{sc} = \begin{bmatrix} 0.0222 & 0.0255 & -0.0047 \\ 0.0255 & 0.6940 & -0.0140 \\ -0.0047 & -0.0140 & 0.2838 \end{bmatrix}$$

The evaluated tensors lead to a tensor-based Error of $E_T = 0.0174$. The same procedure on the IM-LFT sample with an edge length of 10 mm results in an error of $E_T = 0.0397$ derived from the orientation tensors

$$\mathbf{N}_{vol} = \begin{bmatrix} 0.0403 & -0.0115 & -0.0032 \\ -0.0115 & 0.2738 & -0.0658 \\ -0.0032 & -0.0658 & 0.6860 \end{bmatrix}, \mathbf{N}_{sc} = \begin{bmatrix} 0.0324 & -0.0084 & -0.0024 \\ -0.0084 & 0.2947 & -0.0562 \\ -0.0024 & -0.0562 & 0.6729 \end{bmatrix}$$

6.5 Surface Curvature Analysis

The outcomes presented here have partially been published at the EuroHybrid Conference in 2016 [90].

6.5.1 Artificial Images

Errors resulting from the Hessian matrix based measure of surface curvatures on artificial images of spheres with variable radius are depicted in Figure 6.29. The error is around 10 % on spheres of 2 voxels radius using a small blurring parameter σ lower than one voxel. For radii larger than 4 voxels, the error is lower than 2 % for the whole investigated range $0.6 \leq \sigma \leq 6$

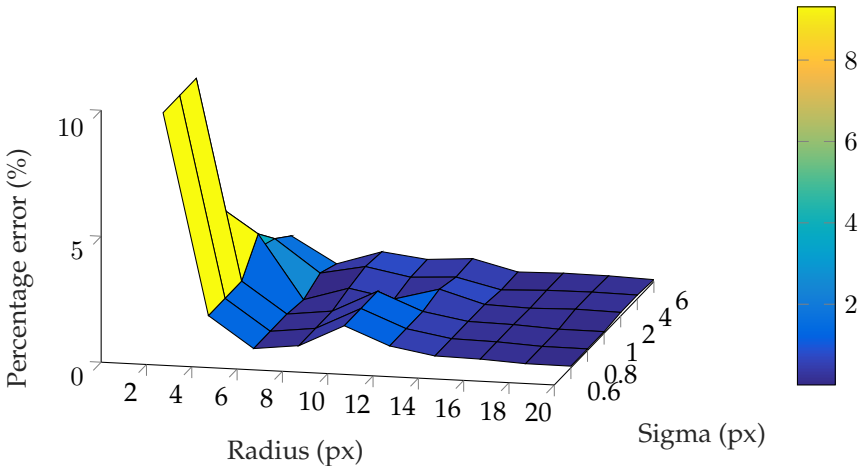


Figure 6.29: Percentage error of surface curvature $E_{c,p}$ examined from spheres of various radius using the Hessian based curvature analysis tool [90].

Investigations with the patch-based method are shown in 6.30. Two different patch sizes $\rho = \{2, 10\}$ are plotted in the graph. Actually, ten steps were evaluated from $\rho = 1 \dots 10$, but the difference from three to ten resulted in surfaces between $\rho = 2$ and $\rho = 10$ in the graph while a patch size of one voxel did not lead to reasonable curvatures. Using a patch size of $\rho = 2$ and higher, the error starts at 50 % for small spheres and decreases constantly with rising radii. The blurring parameter σ shows a very little effect on the results.

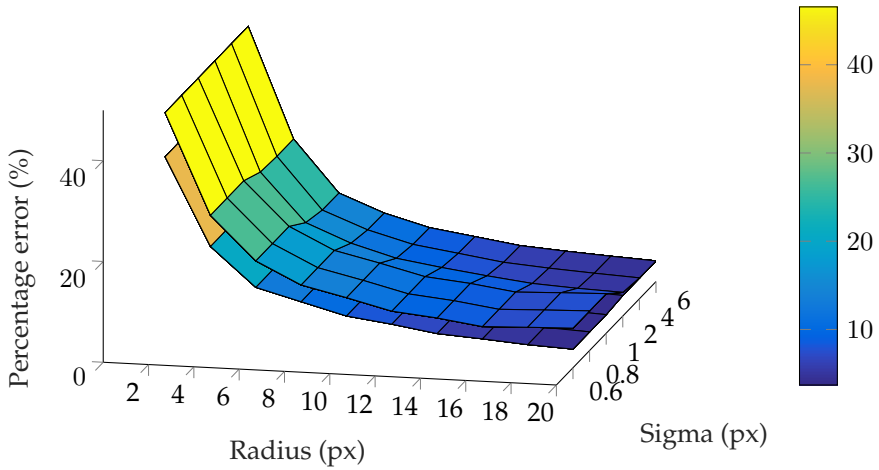


Figure 6.30: Percentage error of surface curvature $E_{c,p}$ examined from spheres of various radius using the patch based curvature analysis tool [90].

6.5.2 Real Images for Validation

Investigations on a real scan of bearing balls of known radius are shown in Figure 6.31 for the method based on the Hessian matrix using blurring parameters of $\sigma = \{3, 10, 20, 30\}$ voxels. Calculation of the curvature in voxels using the ball diameters and the image resolution leads to 0.0075 1/voxels and 0.015 1/voxels for balls with a physical radius of 4 mm and 2 mm. All investigated parameters lead to almost the correct peak values while the sharpness of the regions rises with σ . From a value of $\sigma = 20$ voxels and higher, the function starts to become asymmetric around the peak values and forms a plateau at smaller curvatures.

Figure 6.32 illustrates examinations on the same structure using the patch-based method. It was tested with a wide range of parameters. All configurations resulted in plausible peak values. $\sigma = 1$ voxel and $\rho = 10$ voxels lead to a symmetric function, while $\sigma = 10$ voxel and $\rho = 3$ voxels shows a sharper peak at the same values. Setting σ to a value of 20, the histogram becomes asymmetric in the peak regions and a plateau forms on the left end of the diagram.

Evaluation of the spheres after segmentation by a distance transform and the watershed filter are shown in Figure 6.33 for both methods. The Hessian matrix based method was evaluated with $\sigma = 20$ voxels. Parameters of the patch-based

6 Results

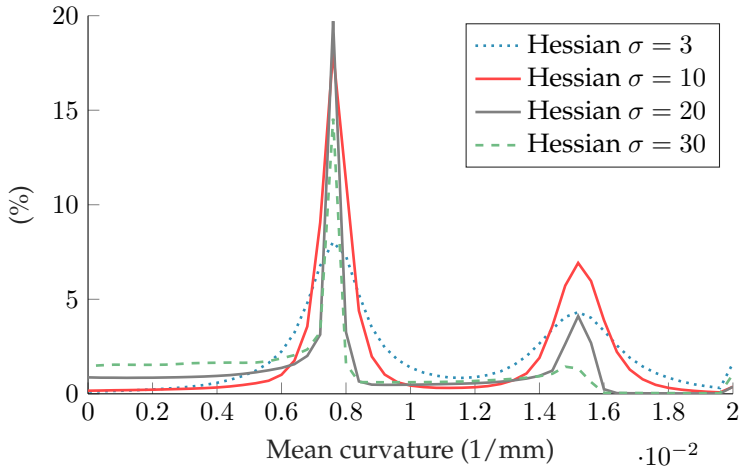


Figure 6.31: Global curvature histogram of steel balls calculated from the surface curvature analysis tool based on the Hessian matrix [90].

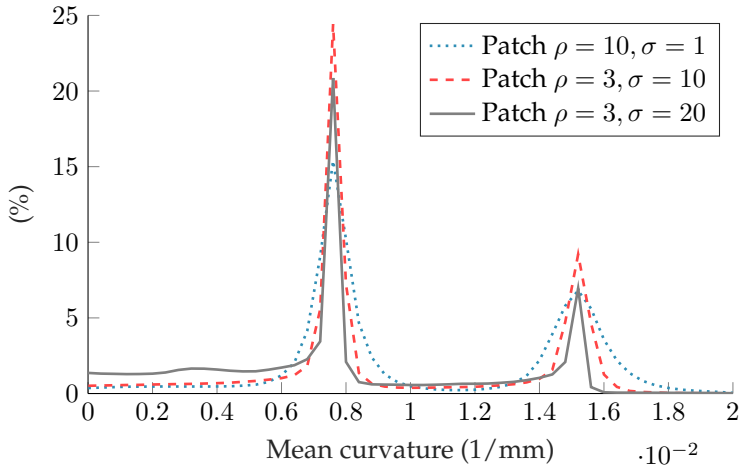


Figure 6.32: Global curvature histogram of steel balls calculated from the surface curvature analysis tool based on the patch method [90].

6.5 Surface Curvature Analysis

algorithm were set to $\sigma = 20$ voxel and $\rho = 6$ voxels. Dark grey dashed lines illustrate the theoretical values calculated from the physical sphere radius.

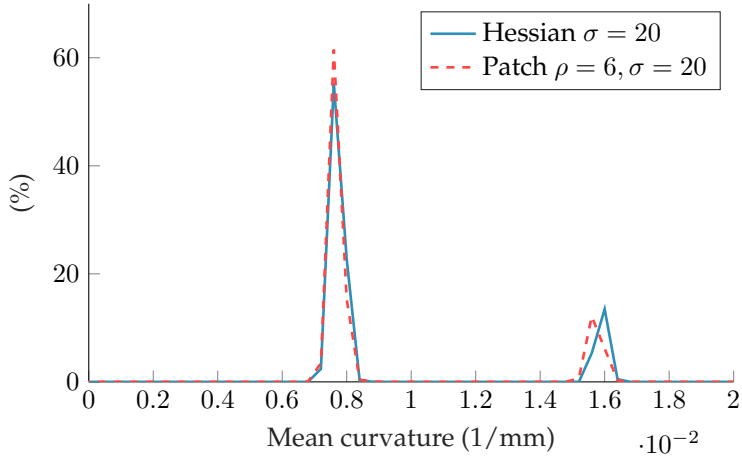


Figure 6.33: Global orientation histogram on steel balls separated by a distance transform and the watershed filter. Dashed lines show the theoretical surface curvature derived from the physical sphere diameter [90].

6.5.3 Pore Analysis on Continuous CFRP

Figure 6.34 shows a curvature analysis on a real porous structure within a CFRP layup. All pores are aligned in fibre direction of the corresponding layer. The image depicts the mean curvature, where the ends of the elongated pores have a higher curvature than the cylindrical part of the pore.

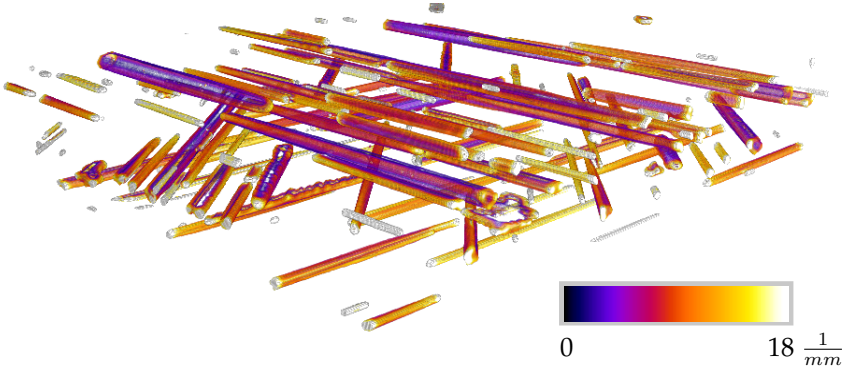


Figure 6.34: Mean curvature analysis on a porous CFRP layup using the Hessian matrix based method. Pore surfaces are coloured with respect to the local curvature.

7 Discussion

7.1 Fibre Orientation Distribution

In the following, the performance of fibre analysis tools is discussed briefly considering results of real and artificial image data in section 6.1. This includes also results of the orientation analysis using parametrized fibres from fibre tracking in section 6.4.3.

7.1.1 Experiments on Artificial Fibres

One and Two Fibre models

Anisotropic Gaussian Filter

Investigations on models using only one or two fibres within an image offered good results in order to determine an optimal parameter set-up in dependence of the fibre diameter for separable high contrast CT images. For reasons mentioned earlier in section 4.1.1, the anisotropic Gaussian filter was limited to an aspect ratio of two. Considering larger aspect ratios, the resulting angular error decreases constantly (Fig. 6.1). Nevertheless, a high aspect ratio could cause issues for curved fibres within real microstructures so the recommendation of the developers [38] was followed throughout this contribution.

Results from the fibre architecture dependent error, which averages the global misalignments over a set of configurations of two fibre models, were used to find an optimal blurring parameter σ . The diagram resulting from an image set with a fibre diameter of 10 voxels led to a minimum at 6 voxels. The same evaluation on fibres with a diameter of 5 voxels resulted in an optimum at 3 voxels. Taking both batches into account, the optimal parameter set is exactly $\sigma = \frac{3}{5}r$, where r is the fibre radius measured from the binary image. This differs slightly from the original paper [37], where it is recommended to set the $\sigma = 0.5r$.

Figure 7.1 shows the cross-section area of an image with two touching fibres processed by the anisotropic Gaussian filter as glyph image where each dash represents its orientation. The blurring parameter used for this evaluation was

7 Discussion

$\sigma = 6$ voxels. The angle between the fibres is 70° . There are many misaligned voxels in the area that influenced by the other fibre. Also, the fibre ends show many dashes that are not aligned in fibre direction. The reason for errors using this method are quite obvious: The orientation is determined by finding the best fitting direction of the ellipsoid over all orientations in every point. At fibre end points and intersection areas, the ellipsoid covers more white area by rotating it out of the fibre direction. Thus, the misaligned angle is recognized as fibre orientation. Because of the significant misalignments at the intersection and the fibre ends, the method is only accurate for low volume fractions and long fibres. Nevertheless, this method can be a good alternative to the structure tensor if the working memory is limited, but only at the cost of higher computation times.

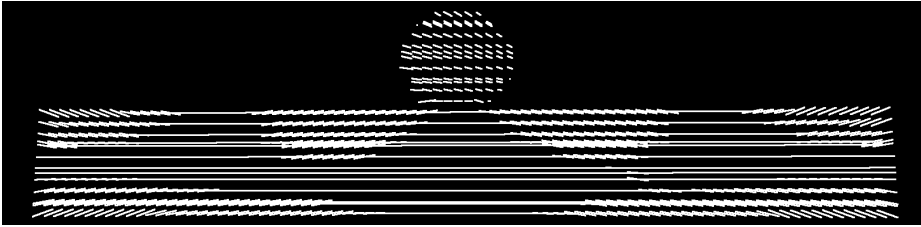


Figure 7.1: Cross section area of two touching fibres with an angle of 70° and a diameter of 10 voxels processed by the anisotropic Gaussian filter [46].

Hessian Matrix

Investigations on a single fibre with a diameter of 5 voxels, 10 voxels or 15 voxels using the orientation analysis based on the Hessian matrix does not lead to an optimum. The error decreases constantly with increasing blurring parameter σ . Nevertheless, for a fibre diameter of 10 voxels and 15 voxels, there is a peak of the error at around $\sigma = \frac{1}{3}r$.

Experiments with two fibres and a fibre diameter of 10 voxels showed that the peak value at a third of the fibre diameter is also present for those models. The optimal value for this diameter was found at 6 voxels. Evaluation of fibres with 5 voxels in diameter did not show this singularity. The minimum error can be found at $\sigma = 2.9$ voxels.

All investigations using the Hessian matrix suggest that the optimal blurring parameter can be estimated by $\sigma = \frac{1}{2}r$. This could cause problems as the peak appears nearby this value at one third of the fibre radius. For an inconvenient choice of σ or for structures including fibres with various diameter, it is likely to end up in the peak error mentioned above.

Figure 7.2 shows a slice through two touching fibres with an relative angle of 70° . The blurring parameter σ was 6 voxels. The influence of the second fibre is very high as the dashes are not aligned to the fibre direction in this region. Also, the orientation on the fibre ends is not estimated correctly. On straight fibre areas without surrounding objects, the orientation estimation is quite good. In summary, the Hessian matrix based method will offer good results on long fibres with low fibre content as there are only few fibre ends and intersection points on binarized data. As fibre reinforced materials for technical applications usually have a fibre mass content of 30% and more, this method is not applicable with appropriate precision. Since the structure tensor led to much better results with the same memory consumption and almost the same processing time, it is the better choice for orientation analysis.

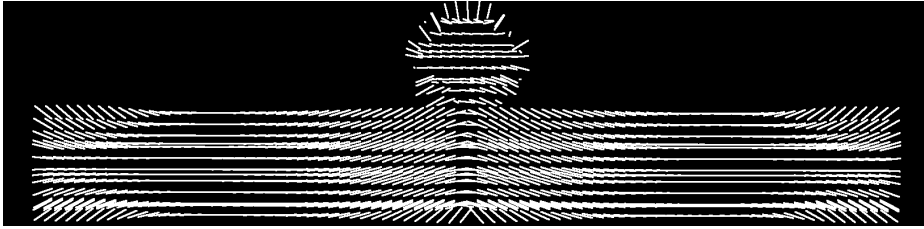


Figure 7.2: Cross section area of two fibres with an angle of 70° and a diameter of 10 voxels processed by the method based on the Hessian matrix [46].

Structure Tensor

Artificial images with only one fibre showed that there is no clear minimum, but the error gets lower for small σ and large ρ (Fig. 6.7). Considering the fibre architecture dependent error with two fibres, there is a local minimum at $\sigma = 0.8$ voxels and $\rho = 5.6$ voxels on fibres of 10 voxels in diameter. Further investigations showed that the optimum of σ remains at the same value for all configurations. The second blurring parameter that is used for the averaging of the tensors within a certain image region is dependent on the fibre diameter. On fibres with a diameter of 5 voxels, it can be found at 3 voxels (Fig. 6.10) and for a diameter of 15 voxels, it is located at 8 voxels (Fig. 6.13). Thus, the optimal parameter ρ is slightly larger than half the diameter. An initial rotation (Fig. 6.12) or doubling of the aspect ratio of the fibres (Fig. 6.11) does not have an influence on the optimal parameter set.

An image plane of the cross section of two fibres is depicted in Fig. 7.3. The relative angle between the fibres is 70° . Process parameters for the structure tensor were $\sigma = 1$ voxel and $\rho = 6$ voxels. Fibres are well aligned in fibre direction. Actually, there is a small misalignment of the dashes that is not visible in

7 Discussion

the first graph. Figure 7.4 shows the same data tilted 20° about the x -axis to illustrate this issue. In the area of differently aligned touching fibres, orientation goes over from one fibre direction to the other steadily. Nevertheless, this error is low compared to the anisotropic Gaussian filter or the Hessian matrix based method which result in an orientation that points towards the centre line of the disturbing fibre.

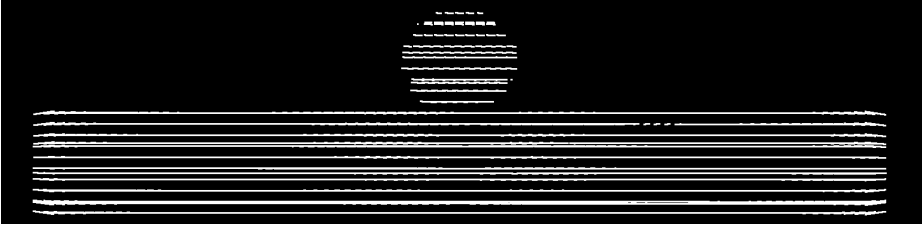


Figure 7.3: Cross section area of two fibres with an angle of 70° and a diameter of 10 voxels processed by the method based on the structure tensor [46].

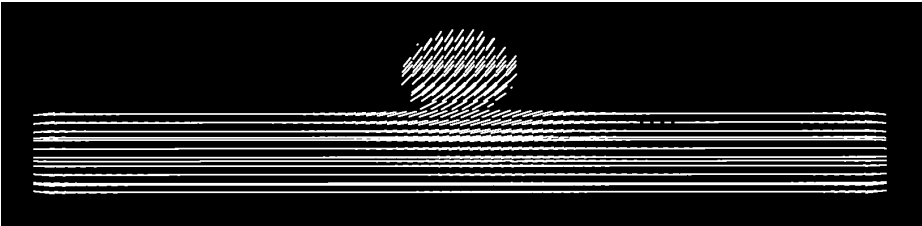


Figure 7.4: Cross section area of two fibres with an angle of 70° and a diameter of 10 voxels processed by the method based on the structure tensor. The slice was rotated 20° about the x -axis to visualize misaligned glyphs on the intersection.

Table 7.1 sums up the errors of artificial images of pairwise fibres. While the Hessian matrix did not show a dependency on the fibre diameter, the error of the structure tensor and the anisotropic Gaussian filter is smaller for a fibre diameter of 10 voxels. The structure tensor based method resulted in the highest precision followed by the anisotropic Gaussian filter.

In the following, the impact of the error criterion E_A on mechanical models used for engineering applications is investigated. Therefore, the elastic stiffness tensor of an unidirectional long fibre reinforced polymer was calculated by a direct Mori-Tanaka [92] homogenisation scheme using the orientation tensors of 2nd and 4th order (cf. e.g. [93]). The method was applied on a unidirectional re-

Table 7.1: Fibre architecture dependent error E_A resulting from investigated methods with different fibre diameters.

Method	10 voxels diameter	5 voxels diameter
Anisotropic Gaussian filter	8.19°	8.48°
Hesse matrix	10.31°	10.31°
Structure tensor	1.68°	2.18°

inforced material because it shows the highest anisotropy in stiffness. Young's modulus and Poisson's ratio of the matrix material were set to $E_M = 3.4$ GPa and $\nu_M = 0.22$, respectively. The fibres were assumed to be made of glass with an Young's modulus of $E_F = 73$ GPa and a Poisson's ratio of $\nu_F = 0.385$. The aspect ratio of the fibres was chosen to $\alpha = 250$. Due to the unidirectional fibre architecture, the fibre orientation tensors of 2nd and 4th order read

$$\mathbf{N} \doteq \begin{bmatrix} 1 & 0 & 0 \\ 0 & 0 & 0 \\ 0 & 0 & 0 \end{bmatrix}, \quad \mathbb{N} \doteq \begin{bmatrix} 1 & 0 & 0 & 0 & 0 & 0 \\ 0 & 0 & 0 & 0 & 0 & 0 \\ 0 & 0 & 0 & 0 & 0 & 0 \\ 0 & 0 & 0 & 0 & 0 & 0 \\ 0 & 0 & 0 & 0 & 0 & 0 \\ 0 & 0 & 0 & 0 & 0 & 0 \end{bmatrix}. \quad (7.1)$$

The orientation-dependent effective Young's modulus \bar{E} is calculated by

$$\bar{E}(\mathbf{d}) = (\mathbf{d} \otimes \mathbf{d} \cdot \bar{\mathbb{C}}^{-1}[\mathbf{d} \otimes \mathbf{d}])^{-1}, \quad (7.2)$$

where $\bar{\mathbb{C}}$ is the effective stiffness tensor and \mathbf{d} is parametrized in spherical coordinates. Figure 7.5 depicts $\bar{E}(\mathbf{d})$ in the x - y plane (cf. [94]). Table 7.1 sums up the error E_A in dependence of the fibre architecture for fibre diameters of 5 voxels and 10 voxels for each of the three investigated methods. In order to evaluate the impact of this error criterion on the effective stiffness predicted by the previously described Mori-Tanaka model, the error of each method is plotted into Fig. 7.5 by coloured dashed lines. The Young's modulus at an angle of 0° is 18.73 GPa. This value is the reference for further investigations. Considering the error of the Hessian based method at an angle of 10.31° , the Young's modulus is only 15.19 GPa which is equivalent to a percentage error of 18.9%. The algorithm based on the anisotropic Gaussian filter leads to an error of 13%. Using the method based on the structure tensor, the percentage error decreases to only 0.6% at a value of 18.61 GPa.

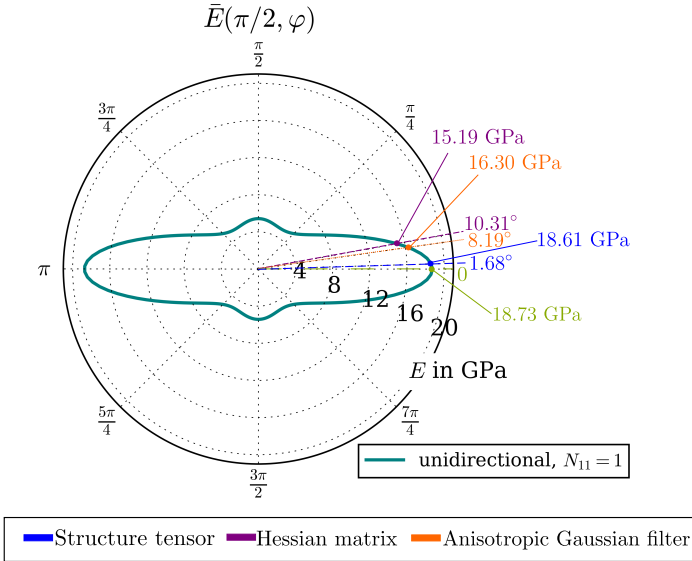


Figure 7.5: Polar plot of the Young’s modulus of a unidirectional glass fibre reinforced polymer [46].

7.1.2 Artificial Fibre Architectures

Figure 6.14 shows that the analysis of tensor based errors resulting from artificial images lead to relatively high errors using the Hessian matrix based method or the anisotropic Gaussian filter. The anisotropic Gaussian filter does also not show a constant trend with increasing fibre volume fraction. Hessian matrix and the structure tensor based method result in a constantly increasing error with fibre content, where the error of the structure tensor is significantly lower. Considering curved fibres the Hessian matrix showed the best performance, but the data is not that firm as the real orientation tensor was derived by an approximation from GeoDict®.

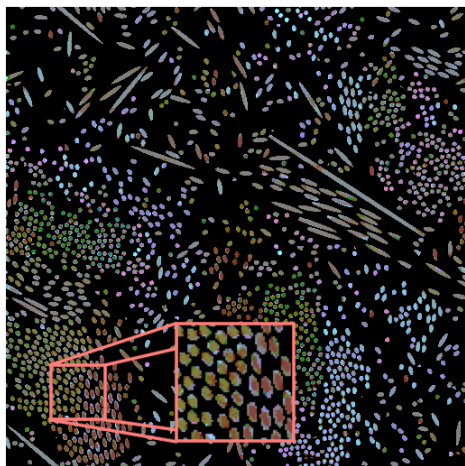
The results match the investigations on one and two fibre models in the previous section very well. The Hessian matrix based method shows the worst performance in most cases. Considering the microstructure with straight fibres and a fibre fraction of 5 vol %, it results in a lower error than the anisotropic Gaussian filter. This results from the fact that the fibres are very sparse and there are no touching points so the Hessian matrix can perform well. The anisotropic Gaussian filter can only result in discrete orientations that are chosen by a orientation table initially. Thus, it cannot match orientations that are not listed within this table perfectly. Those are reasons why the anisotropic

Gaussian filter performs better than the Hessian matrix for higher fibre contents. The Hessian matrix is negatively affected by the touching fibres and thus, the resulting error gets larger than the influence of the misalignment caused by the quantification of the anisotropic Gaussian filter (cf. Fig. 7.1 and Fig 7.2).

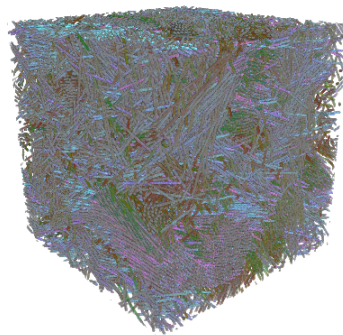
Considering 2D slices and 3D rendered data of processed images, misaligned areas can be spotted. Figures 7.6 through 7.8 show those images for the three methods investigated. The 2D slice cropped from the image processed by the anisotropic Gaussian filter shows a different orientation in the centre of each fibre than on its edge. This effect appears especially in regions of high fibre density. The rendered 3D representation of the same data shows not many different colours on the surface what means that the orientation does not change very much. Most of the surface appears in a purple colour. The method based on the Hessian matrix is illustrated in figure 7.7 and shows the same effect. The fibre orientation changes over the fibre cross-section and the 3D representation is dominated by a purple colour. The orientation analysis using the structure tensor in figure 7.8 shows a constant orientation within each fibre in 2D and a very colourful representation on the surface in 3D, where each fibre bundle can be recognised. This indicates that this method does not produce significant edge effects. The same circumstance was already observed on the two fibre models in figures 7.1 through 7.4. Also, the effect of misalignments on the edge where fibres are very close was clearly visible in those images. Comparing the colour of single fibres in the images processed by the Hessian matrix and the structure tensor, the base colours are very similar for most of the structure. In contrast to that, the image resulting from the anisotropic Gaussian filter shows a slightly different colour in most of the fibres what is an effect of the quantification. Most of the exact orientations are not available in the table of orientations used for the evaluation.

7.1.3 Real Images with known Orientation

Scans of real CT-scans of known orientations offered important new findings about the applicability of the investigated orientation analysis tools. The orientation analysis on the glass fibre reinforced 3D-printed sample led to good results for all of the three methods. The N_{xx} -component of all the orientation tensors is higher than 0.92, what indicates a high x -alignment of the fibres. Those very good results are caused by the high contrast between glass and polymer matrix and the low fibre content of only 10 %. Thus, the fibres are very sparse distributed throughout the material. The average fibre length is 0.2 mm and the fibre radius is around $13 \mu\text{m}$ so the aspect ratio is approximately 15.4. The fibres are long enough to keep the influence of the fibre ends small. Nevertheless, there is a little impact of fibre ends and neighbouring fibres which caused

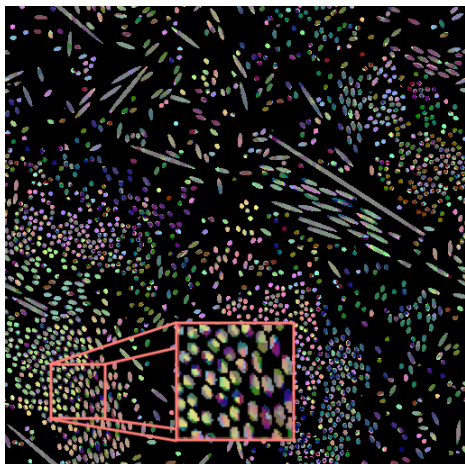


(a) 2D slice

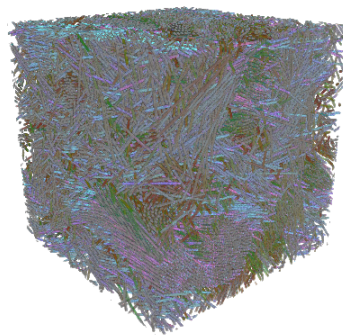


(b) 3D rendered Image

Figure 7.6: Fibre orientation analysis on artificial image with 20 vol% glass fibres using the method based on anisotropic Gaussian filtering. Fibre orientation is coded by colour using the HSV colour space.



(a) 2D slice



(b) 3D rendered Image

Figure 7.7: Fibre orientation analysis on artificial image with 20 vol% glass fibres using the method based on the Hessian matrix. Fibre orientation is coded by colour using the HSV colour space.

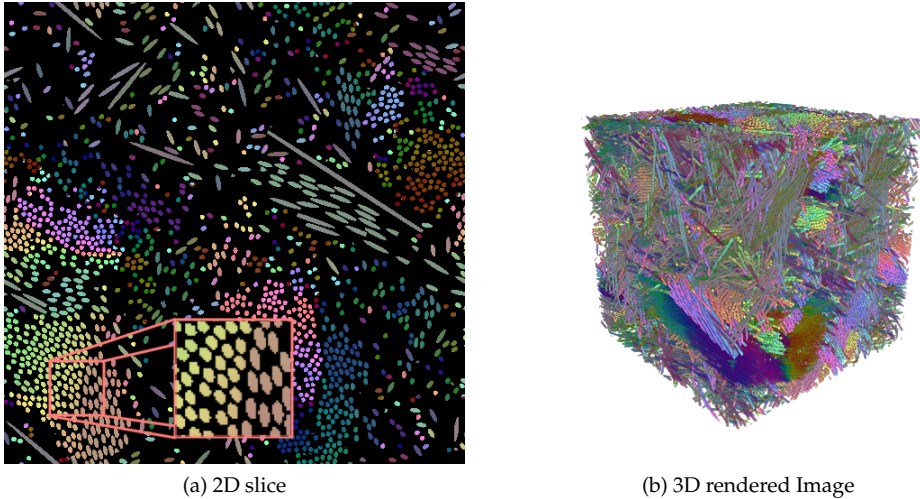


Figure 7.8: Fibre orientation analysis on artificial image with 20 vol% glass fibres using the method based on the structure tensor. Fibre orientation is coded by colour using the HSV colour space.

a small difference between the methods at hand. Even though the correct fibre orientation tensor is not known, it is most likely that the structure tensor is most precise with $N_{xx}=0.97$. The methods based on the anisotropic Gaussian filter and the Hessian matrix suffer from their typical errors described previously and lead to values of $N_{xx}=0.92$ and $N_{xx}=0.93$.

Further validation using a continuous carbon fibre reinforced rod show the weaknesses of the methods. The contrast is very low what is typical for carbon fibre reinforced polymers. Thus, it is not possible to separate fibres from matrix material and the fibre orientation analysis has to be carried out over the entire volume. The methods based on the anisotropic Gaussian filter and the Hessian matrix result in an orientation tensor that is almost isotropic. Further investigations with various parameter sets were carried out in order to optimize those methods for the data at hand, but none of them was working. The structure tensor led to a highly anisotropic orientation tensor with $N_{xx}=0.998$. Note that the input parameters for this method are chosen differently to the recommendations in section 7.1.1. As the fibres cannot be separated, the mask size for the averaging of the tensors was set to $\rho=4$ in order to integrate over a larger region and make the method more robust against image noise.

7.1.4 Orientation Tensors derived from Spatial Curves

Deriving the orientation tensor from spatial curves is different to voxel-based methods regarding the method to achieve those tensors. While voxel-based methods result in a volume weighted tensor, the calculation from spatial curves according to equation 4.18 leads to a tensor weighted by its fibre length. For constant fibre diameters, both approaches result in exactly the same tensor. Investigations on high resolution scans of LFT material in section 6.4 showed that orientation tensors derived from spatial curves result in almost the same tensors calculated by voxel based methods. For the two scans with a resolution of $3.32 \mu\text{m}/\text{voxel}$, the bias between both methods is $E_T = 0.017$ and $E_T = 0.027$. Using larger image regions with a resolution of $5.85 \mu\text{m}/\text{voxel}$, the error increases to $E_T = 0.04$ for both methods. It is noteworthy that this error is still lower than most results of voxel based methods on artificial data (cf. section 6.1.2). The conclusion is that voxel-based methods do not cause a large discrepancy due to quantification errors caused by the voxel grid.

7.1.5 LFRP Material

The structure tensor gave the best performance with respect to the precision and robustness in previous investigations. Thus, only this method was applied on the materials of interest.

GF SMC

Glass fibre reinforced SMC shows a high contrast between glass fibres and polymer matrix but most of the fibres exist in bundles what makes it difficult to separate them one by one. Nevertheless, the fibre bundles can be separated from the matrix. Assuming that the error resulting from an over-segmentation influences each bundle in the same way, the statistical orientation approaches should work fine. Figure 6.15 shows clearly that the orientation analysis works well in most regions. Only some small parts of the bundles show misalignments if there is another neighbouring bundle in the next image slice. However, those erroneous evaluations are quite small compared to the entire sample and can be neglected.

CF SMC

SMC material with carbon fibres is more demanding to the algorithm as the contrast is very low. It is not possible to separate fibres from the matrix material

and thus, the threshold for the fibre analysis is set to zero. This causes, that the algorithm evaluates orientations also on positions under absence of fibres. Assuming that the influence of neighbouring fibre bundles has the same effect on the orientation analysis that is carried out on the bulk matrix material, it will still be a good approximation of the real distribution function. Figure 6.16 shows clearly that most of the areas within the image are evaluated correctly.

GF LFT

Considering orientation analysis tasks, glass fibre reinforced LFT material is very similar to the GF SMC material. Fibres have a high contrast to the matrix but in most of the regions they can be separated one by one because they do not exist in bundles. High shear deformation in the extruder forces the initial fibre bundles to drift apart during the manufacturing process. Figure 6.17 shows the corresponding orientation analysis where most of the fibres are separated.

Hybrid Sample

As the hybrid sample consists of discontinuous GF SMC and continuous carbon fibre reinforced material, the evaluation should work well because both materials systems have been investigated before. Nevertheless, trying to separate the different microstructures by the coherence measure (cf. 6.18) causes some issues. Even though the three regions can be recognized by the naked eye, it is hardly possible to separate them automatically. Considering a sample size of only $10 \times 10 \times 3.3 \text{ mm}^3$, there is a high possibility that there are some image slices in thickness direction of the SMC material that are almost unidirectional. Thus, there are slices with a coherence measure higher than 0.3 within the SMC regions. Also the region consisting of continuous CFRP material shows two significant low points with a coherence measure below 0.2. Those points are caused by the fixation strings made of glass fibre which are used to keep the carbon fibres in position during the manufacturing process. These two reasons make it difficult to separate the microstructures in the present case. Nevertheless, the method can be used if there are no fixation strings within the continuous fibre reinforced regions or if the image region is large enough that the probability for a unidirectional area in the SMC material gets low.

7.2 Fibre Volume Fraction

Fibre volume fractions calculated by a threshold on the grey value must be treated with caution as image histograms differ with the reconstruction method, material system, fibre architecture and image resolution. In the following, results of investigations on GF SMC and GF LFT in section 6.2 are discussed.

GF LFT Material

Global image histograms of the LFT samples investigated are shown in figure 7.9 for a fibre volume content of 10 wt %, figure 7.10 for 20 wt % and figure 7.11 for 30 wt %. First of all, it is noteworthy that none of the LFT images shows a bimodal histogram (cf. Fig. 2.4). Thus, the *Minimum* method did not converge as there is no local minimum within the histogram. The number of voxels at the peak value decrease with increasing fibre content and more values are classified in values up to about 200. Due to the sharp peak at lower values, it is hardly possible to binarize 50 % of the image using the *Percentile* method. Actually, it is only possible to separate at natural numbers and thus, there are only 255 possibilities to set a threshold on an 8bit image. The higher the slope of the histogram, the higher is the possible quantification step in volume fraction. Thus, the probability is not that low to get the same results for two different methods. Nevertheless, higher values at a lower slope are more interesting for the material at hand as the fibre content is relatively low. Picking the best thresholding grey value by hand with respect to the fibre volume fraction derived from TGA measurements leads to a grey value of 65 on the 10 wt % specimen, 69 with 20 wt % and 58 with 30 wt % glass fibres. The values are marked by a red dot in the histograms. Considering LFT material with the parameters at hand, *Otsu* and *IJ_IsoData* provided the most reliable data as it resulted in a relatively small and almost constant over-prediction.

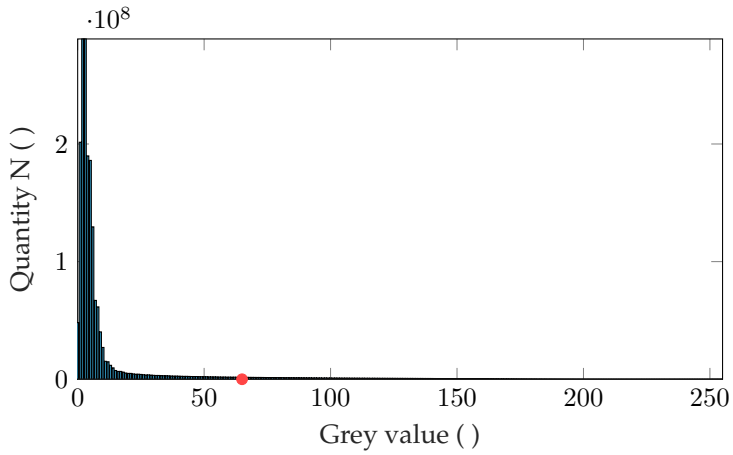


Figure 7.9: Global image histogram of 10% GF LFT sample. The red dot illustrates the correct threshold for segmentation with respect to the TGA measurements.

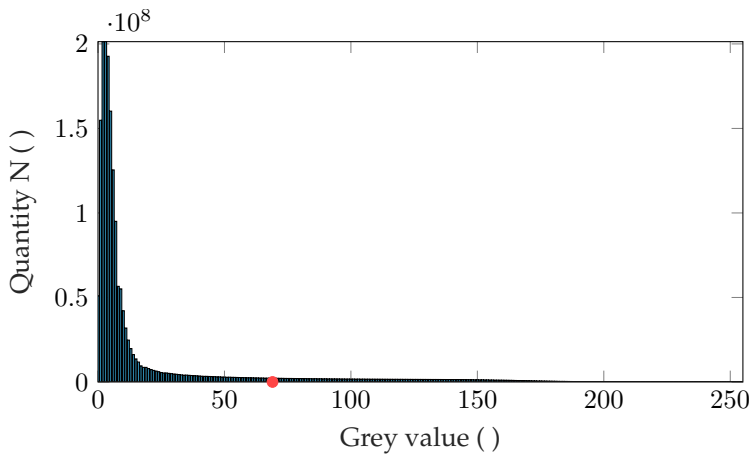


Figure 7.10: Global image histogram of 20% GF LFT sample. The red dot illustrates the correct threshold for segmentation with respect to the TGA measurements.

7 Discussion

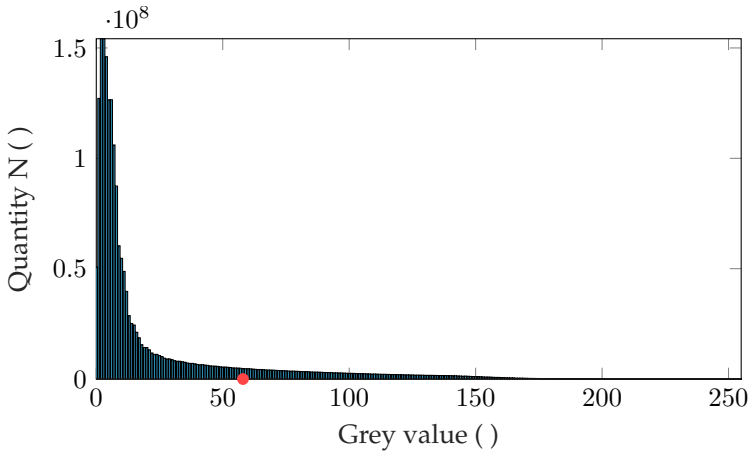


Figure 7.11: Global image histogram of 30 % GF LFT sample. The red dot illustrates the correct threshold for segmentation with respect to the TGA measurements.

GF SMC Material

Investigation of fibre volume fraction on SMC material resulted in a very different result as on LFT Material. The image histogram of sample 2B_0.1 is illustrated in figure 7.12. Histograms of other SMC samples look very similar. The optimum threshold with respect to TGA experiments is at a grey value of 71 leading to a fibre volume content of 23.96 vol %. Segmentation techniques on SMC samples tend to recognize the little spaces between the fibres within a bundle as fibre material. Thus, more methods resulted in an over-estimation of the fibre content. *Percentile* showed did not deviate more than 0.6 vol % what is caused by the relatively low slope compared to the LFT samples. The best performance on SMC Material was provided by the *Moments* algorithm with an maximum error of 1.2 vol %.

Summed up, the evaluation of fibre volume content can be used for relative investigations but not for absolute values. Also, the thresholding method should be chosen with respect to the material system at hand in order to obtain good approximations. Nevertheless, the average percentage error on SMC material is around 4 %, what is quite high depending on the application of the data. Considering e.g. the fibre volume fraction over thickness of a sample for mechanical models, it is recommendable to norm the overall fibre content by a known value.

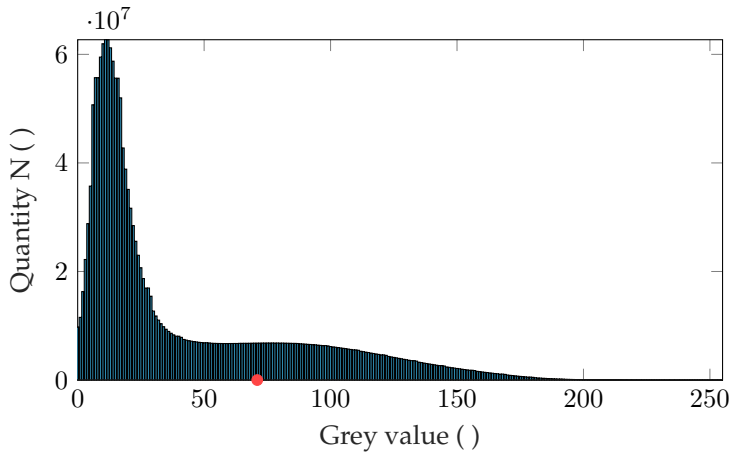


Figure 7.12: Global image histogram of GF SMC sample B.0_1. The red dot illustrates the correct threshold for segmentation with respect to the TGA measurements.

7.3 Fibre Length Distribution

7.3.1 Optical Methods

FiVer

Fibre length distributions from specimen incineration and optical measurements using FiVer show a tendency for rising x -values of the peaks for increasing specimen sizes. Nevertheless, both investigated batches have their peak value at 0.8 mm for 5 mm and 10 mm samples. For those sample sizes, all fibres within the specimen were measured while only a subset of fibres was extracted from the samples with an edge length of 20 mm and 40 mm. Small samples show a constant FLD while the curves of larger specimens are less consistent. The thinning process that is necessary to extract a subset of fibres could possibly influence the results as smaller fibres could get lost and thus peaks are shifted to the right-hand side.

FASEP

Even if there is an additional smaller peak in the FLD of the IM-LFT-5mm sample, the positions of the peak values on the length axis are very close with FASEP and FiVer. It is especially noticeable that the resulting FASEP curves appear “noisy”. This results from a lower quantity of fibres that were investigated and is not necessarily a measure for the quality of the FLD. Table 7.2 shows the number of fibres that were investigated by the different systems for each sample.

Table 7.2: Number of investigated fibres by FASEP and FiVer for each sample.

	FASEP	FiVer
IM-LFT 5mm	6346	49567
IM-LFT 10mm	6563	205668
IM-LFT 20mm	5073	42172
IM-LFT 40mm	5053	78636

Even though there are small deviations in the FLDs using FASEP and FiVer, both methods seem to indicate plausible data. Nevertheless, based on the available data, it is not possible to give a statement about the quality of both methods. There are too many factors, like the sample preparation or the transport of the fibres from one device to the other, which can possibly influence the results. Summed up, both methods seem to offer FLDs with sufficient accuracy for injection moulded LFTs.

7.3.2 FLD derived from CT-Images

Fibre length measurements on LFT material with PP matrix (identifier LFT) are depicted in Figure 7.13 for a sample size of 5 mm and in Figure 7.14 for a sample size of 10 mm. All histograms are weighted by mass and built with a bin width of 0.1 mm using 100 samples to 10 mm. Results of specimen with an edge length of 5 mm are very similar to those from the measurements using optical methods like FiVer or FASEP. All peaks are at a fibre length of 0.7 mm.

Measurements on 10 mm samples show a bias between the methods where the curve resulting from the fibre tracking algorithm is shifted slightly to the left. Peak values are at 0.7 mm for results from both optical methods and 0.5 mm derived the CT-data even if the curve from FASEP includes slightly more long fibres. Obviously, the fibre tracking method did not work properly on the image

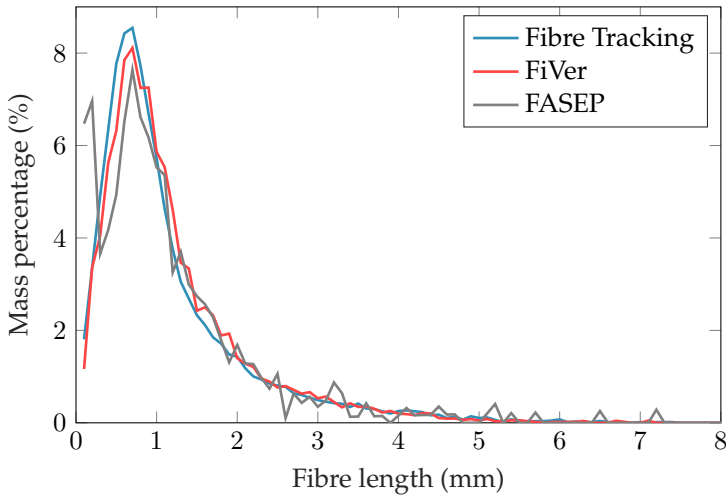


Figure 7.13: Fibre length distribution of the IM-LFT sample with an specimen size of 5 mm.

with lower resolution. The image data of the smaller sample has a resolution of $3.32 \mu\text{m}$ in contrast to the large one with only $5.81 \mu\text{m}$. The glass fibres used in the material have a diameter of around $13 \mu\text{m}$ and thus, a fibre has a diameter of around 4 voxels in the high resolution but only slightly more than 2 voxels in the image with lower resolution. The pre-processing introduced in section 4.2.1 cannot perform very well on small diameters as the surface of the fibre is too small to cause enough image gradients that enable to gain the grey value of the centre line. Consequently, it is not possible to separate fibres at touching points and many intersections have to be resolved in the fibre tracking algorithm (Fig. 4.8). If intersections get to large, what happens quite often for in resolution images, it is no longer possible to assign connecting fibres correctly. Furthermore, fibre paths get interrupted due to a low resolution since the circular voting filter generates a less constant grey value along the centre line and thus, gaps appear after thresholding .

7 Discussion

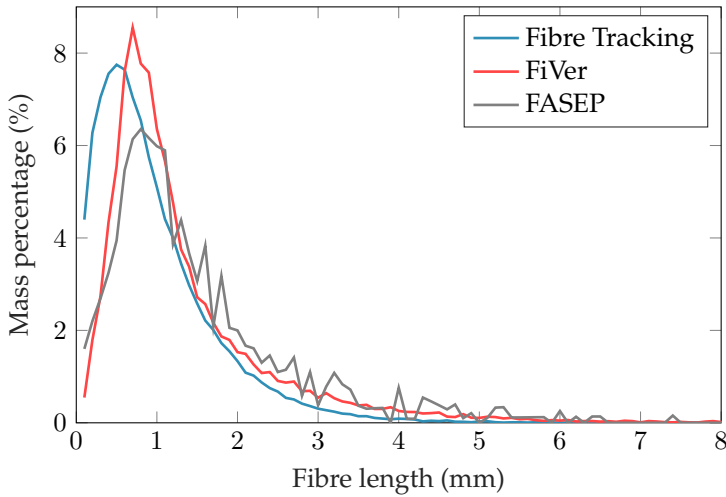


Figure 7.14: Fibre length distribution of the IM-LFT sample with a specimen size of 10 mm.

7.4 Fibre Curvature

IM-LFT

In section 6.4.2, statistics about fibre curvature of the 5 mm IM-LFT are shown. Most of the fibres within the sample have a bending radius of 1 mm. There is also a very small peak at a radius of 0.15 mm. Fibres with such a small bending radius are most likely over-fitted because the fibres break at a bending radius of around 0.132 mm. The spline fitting algorithm uses a 3rd degree polynomial function for a length of twenty voxels. However, if a fibre is e.g. only three voxels long, the same cubic function is not well defined and can lead to extremely high curvatures (cf. Fig. 4.9). Unfortunately, there is no alternative method than computed tomography to derive fibre curvatures from composite materials in order to acquire data for validation. Furthermore, there is no other image processing tool to evaluate fibre curvatures at the current state of research. Thus, spline fits of a random subset of curved fibres longer than 4 mm with a bending radius between 0.5 mm and 1.5 mm were plotted in figure 7.15 to estimate the quality of the achieved data. All fibres have random colours to distinguish between different objects easily. All plotted fibres within the graph show a high curvature and length. Most of them seem to be tracked correctly except the blue fibre on the left, where two fibre ends were connected erro-

neously. Figure 7.16 shows a subset of fibres with a length of more than 0.7 mm and a bending radius larger than 3 mm.

Compared to the estimation of fibre length distributions from tracked fibres, the curvature is less critical as a lost fibre does not necessarily result in a wrong value. Curvature can also be evaluated on many smaller fibre snippets while the connectivity of the entire fibre is essential for the determination of fibre length distributions. Thus, curvature can also be derived with slightly lower image resolutions.

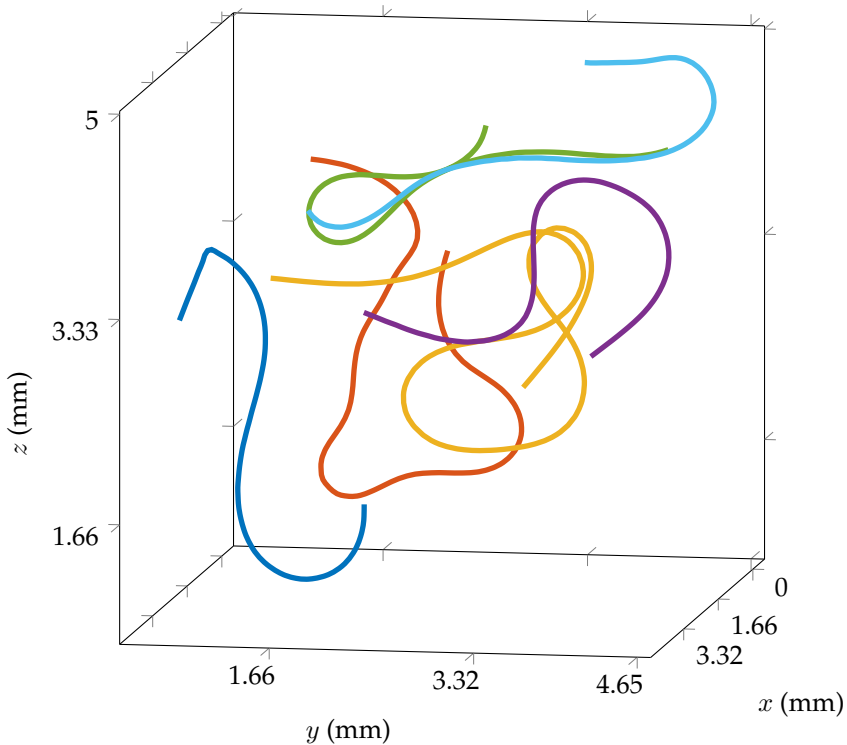


Figure 7.15: Plot of a random subset of fibres longer than 4 mm and a mean bending radius of $0.5 \text{ mm} \leq r \leq 1.5 \text{ mm}$ derived from the IM-LFT sample with a size of 5 mm.

7 Discussion

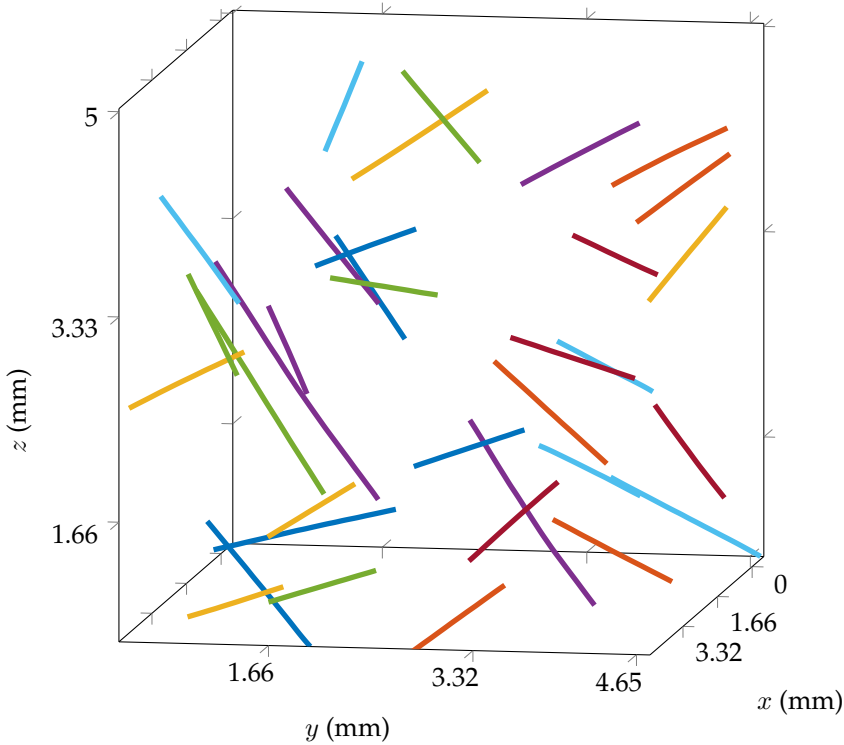


Figure 7.16: Plot of a random subset of fibres longer than 0.7 mm and a mean fibre bending radius $r \geq 3$ mm derived from the IM-LFT sample with a size of 5 mm.

DiCo GF SMC

The fibre curvature histogram shown in Figure 6.28 shows a lot of fibres with very high curvature. It is likely that those fibres are tracked erroneously as the fibre radius within the material was not perfectly constant and consequently, the CircularVoting filter could not perform very well in order to gain the centre axis of the material. Nevertheless, there is another less sharp peak at 7.5 mm and reaches to curvatures up to a bending radius of 30 mm. For SMC material, those values are plausible because the fibres exist in bundles and thus, the bending stiffness of the fibres is much higher. As they are flat within the material, it is easier to bend them over the lower principal axis of their cross-section it is easier for them to bend in plate thickness direction. Hence, the fibre cur-

vature cannot be seen on materials with transparent matrix materials. Figure 7.17 shows a subset of fibres with a length of more than 0.5 mm and a bending radius higher than 2 mm tracked from the DiCo GF SMC material with an scanning size of 2.5 mm.

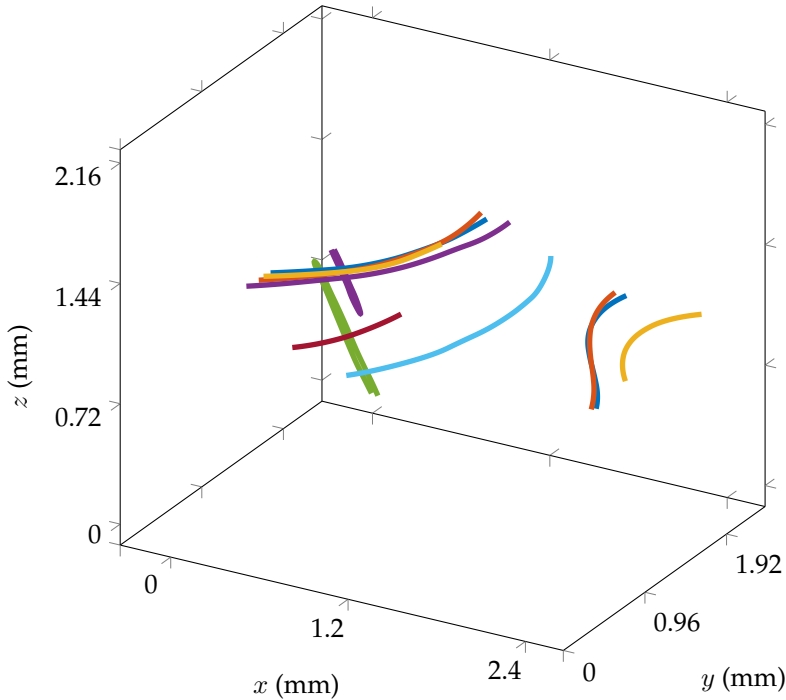


Figure 7.17: Plot of a random subset of fibres longer than 0.5 mm and a mean bending radius higher than 2 mm derived from the DiCo GF SMC sample with a size of 2.5 mm.

Those fibres were found near the centre of the plate in two different roving with high curvature. The green fibre on the left is tracked erroneously as two fibres are connected. Considering the same structure with fibre radii higher than 2 mm, there are many more fibres because most of them in SMC material have a low curvature.

Summed up, the curvature analysis of LFRP materials seems to be plausible, even if there is no proof of correctness. Obviously, the data is less accurate for low resolution images. But as the curvature is less dependent on the connectivity of voxels, it is possible to use smaller samples with higher resolution for this kind of characterization.

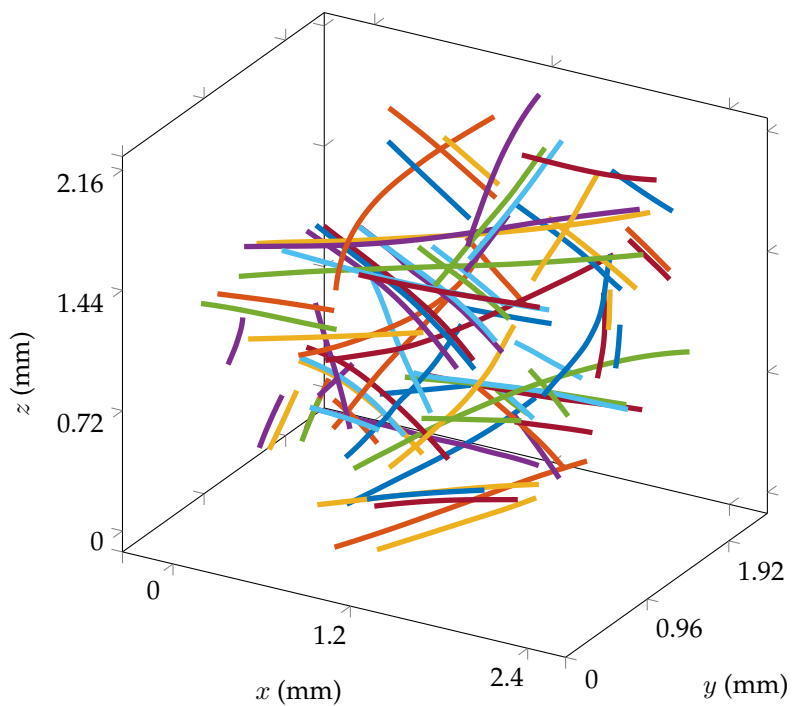


Figure 7.18: Plot of a random subset of fibres longer than 0.5 mm and a mean fibre bending radius lower than 2 mm derived from the DiCo GF SMC sample with a size of 2.5 mm.

7.5 Surface Curvature Analysis

7.5.1 Surface Curvature Analysis on Artificial Images

Results from artificial images of spheres showed that there is no optimum for the blurring parameter σ using the Hessian matrix based method. Nevertheless, the error is lower than 2% for $\sigma \geq 2$ voxels and a sphere radius up to 20 voxels. Computing times are almost independent of parameter σ due to the efficient implementation by a separable recursive filter. The patch based method results in an error of around 5% using a high patch diameter of $\rho = 10$ voxels while the blurring parameter σ did not affect the precision significantly. On the downside, the large patch size affects the computation time considerably. Furthermore, the algorithm leads to relatively high errors on small pores. It falls below 10% at a sphere radius of around 10 voxels.

7.5.2 Surface Curvature Analysis on Real Images for Validation

Evaluations of the CT scan of ball bearings shows a good correspondence of the curvature calculated by both algorithms and the images. On the entire structure, both methods lead to an asymmetric function if the blurring parameter σ is chosen too high (cf. Figure 6.31 and 6.32). Nevertheless, a higher value leads to sharper peaks in the curvature histogram. Figure 7.19 shows the surface curvature evaluated by the Hessian matrix in a two-dimensional slice through the structure for a blurring parameter of σ of 3 voxels and 10 voxels. Apparently, the curvature gets smoother with higher σ , but also the influence of neighbouring objects increases. Using small σ , a slight speckle pattern appears on the structure. This leads to a wider peak in the surface curvature histogram in Figure 6.31. On touching points, the curvature turns from a small positive value into a high negative value. Those highly negative curvatures can be seen in Figure 7.20 by the red circles on the touching points, while the spheres appear in yellow where the intensity illustrates the curvature. The transition of the curvatures between structures of different radii is the reason for the plateau areas which appear between the peaks and also on the left-hand side of the left peak. As the curvature fades slowly from one value to the other, all values in between are also existent within the image.

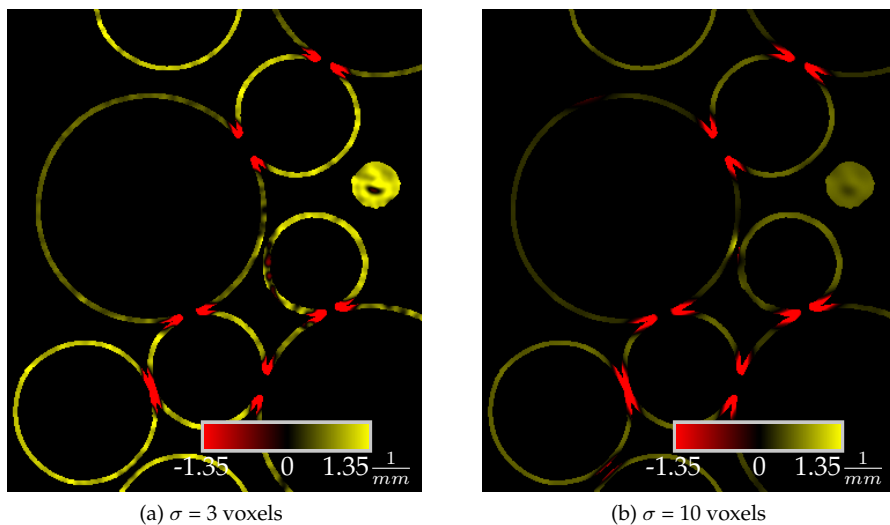


Figure 7.19: Curvature derived from the CT-scan of bearing balls by the Hessian-based method.

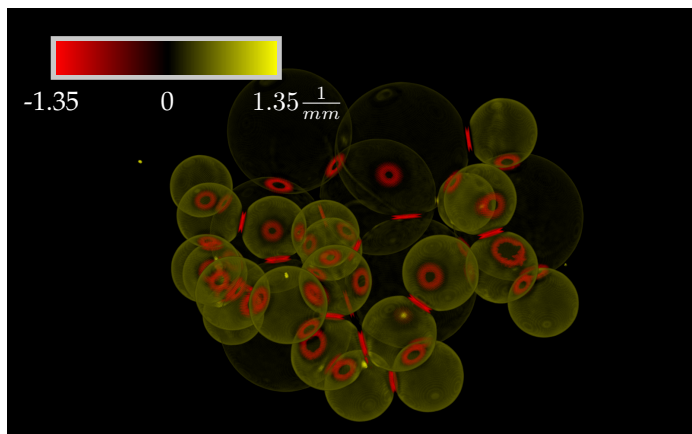


Figure 7.20: 3D representation of curvature derived from the CT-scan of bearing balls by the Hessian-based method with $\sigma=10$ voxels.

The patch-based method shows a very related behaviour for with respect to the blurring parameter σ . Higher values cause a smoother curvature distribution on the surface with growing transition zones between different radii. Figure 7.21 shows that using a large patch size offers also a good result and keeps the transition zones small but as mentioned before, the computation times increase significantly with ρ .

Separation of the spheres by a watershed filter results in a histogram where peaks are not connected by a plateau. The histogram shown in 6.33 was generated by a superposition of the curvatures of the single spheres which were processed one by one. Thus, blurring parameters can be chosen larger without influencing neighbouring objects. The dashed lines in the histogram illustrate the real curvature of the objects derived from the physical radius. Converted to the radius, the Hessian based method leads to peak values of 3.87 mm and 1.91 mm. The patch-based method results in 3.89 mm and 1.89 mm.

Methods for determination of surface curvature can be used for the local description of pores or inclusions. High curvatures within a microstructure usually come along with high notch factors and could be used in order to find hot spots in strain. Furthermore, fibre ends cause a high Gaussian curvature (eq. 2.41). This circumstance can also be seen on the pore analysis of the CFRP-layup in figure 6.34, where the ends of the elongated pores show a high mean curvature. Assuming a volumetric image with straight fibres, areas on the shell of the fibres have theoretically a Gaussian curvature of zero as one of the principal curvatures is zero. Hence, the shell appears very dark while the fibre ends show bright dots in the resulting image. Nonetheless, the algorithms can be used for the analysis of foams since the curvature correlates with the pore diameter.

7 Discussion

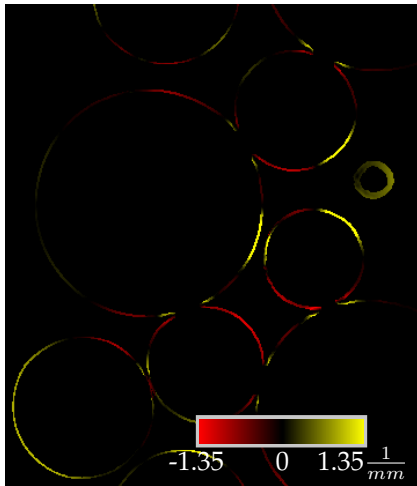
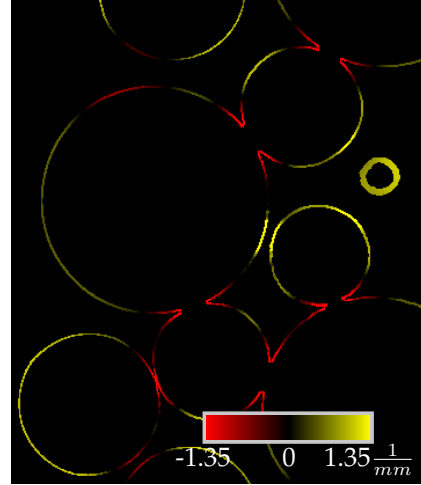
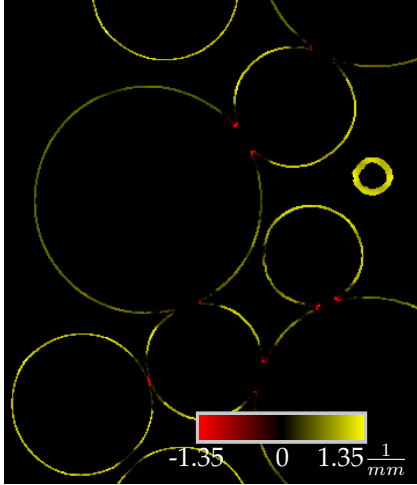


Figure 7.21: Curvature derived from the CT-scan of bearing balls by the patch-based method.

8 Conclusion

Investigations have been made in order to evaluate different approaches for orientation analysis on volumetric images. Therefore, artificial binary data of single and pairwise fibres with certain angle, diameter and distance have been investigated in order to determine optimal parameter sets for each algorithm. The algorithms have been applied to binary images artificial microstructures generated by GeoDict[®] in order to calculate the tensor-based error E_T . Results showed that the structure tensor based method leads to the most precise data on most of the structures investigated. It was also observed that the structure tensor based orientation analysis leads to an assessable error for higher fibre volume contents where the methods based on the Hessian matrix and the anisotropic Gaussian filter had outliers considering the error over fibre volume fraction. Investigations on real images like a short fibre reinforced 3D printed bar with known fibre orientation led to good results with all three orientation analysis tools as the fibres have a high contrast and are separable from the matrix material. Evaluation of a carbon fibre reinforced pultruded rod resulted in almost isotropic orientation tensors for the methods based on the Hessian matrix and the anisotropic Gaussian filter. The contrast of carbon fibres on polymer is too low to separate fibres from matrix material. Only the structure tensor based method provides good results on those low-contrast images. As the structure tensor was the only method that has satisfied all requirements for a precise and robust orientation analysis, it was applied on LFRPs including carbon and glass fibre reinforced SMC as well as unidirectional carbon fibre reinforced material. Image slices through the volumetric images were shown which illustrate the planar orientation in HSV colour space. Those pictures show a very good correspondence of calculated orientations and the local structure described by the CT scan. The coherence measure was introduced to separate continuous from discontinuous layers within a lay-up. It was shown that the method works in general, but as there are fixation strings made of glass fibre 90° to the unidirectional fibres, this method is applicable for this material.

The fibre architecture dependent error E_A was used to estimate the influence of a misalignment caused by the fibre orientation analysis on an elastic mechanical model. The stiffness tensor for a unidirectional glass fibre reinforced polymer was calculated using a homogenisation scheme with respect to Mori-Tanaka. It

8 Conclusion

was shown that the error resulting from the structure tensor leads to a deviation of only 0.6 % in stiffness.

Fibre volume fractions were calculated by common grey value thresholding techniques. For validation, samples of glass fibre reinforced LFT and SMC has been incinerated in a thermogravimetric analysis device in order to derive the fibre mass fraction. Using the density of the constituents, results were converted to the fibre volume fraction. Results of thresholding methods on volumetric images of both material systems showed that there is no universally applicable procedure. Many of the methods investigated led to a significant overestimation of fibre volume content and can be excluded from the list of suitable thresholding procedures. Most promising methods were *Otsu*, *Moments* and *IJ_IsoData*. While *Otsu* and *IJ_IsoData* work pretty good on separated glass fibres within LFT materials, the *Moments* method provides best results on the SMC material with bundled fibres.

A fibre tracking algorithm has been introduced in order to evaluate fibre length distributions, orientation tensors and statistics about fibre curvature. The circular voting filter was used as a pre-filter to separate glass fibres by gaining the centre lines by a surface overlap measure. It was shown that the pre-filter is able to improve the raw data for the use for thresholding and skeletonization. An algorithm was introduced to resolve remaining crossings in the resulting fibre network and connect fibre segments with matching orientations. The voxel data of the centre lines was used to fit spatial curves by B-splines and to parametrize those curves using the Frenet-Serret equations. Using this parametrization, a mean curvature was evaluated for each fibre. This enables to construct statistics describing e.g. curvature over fibre length or to localize curved or straight fibres. Spatial curves integrated to derive orientation tensors of 2nd order and compare them with voxel-based methods investigated preciously. Resulting errors were approximately in the same range as those of the structure tensor on artificial structures and thus it can be stated that the volume averaged and the length averaged orientation tensor can be assumed to be equal in glass fibre reinforced polymers. Theoretically, this is only true for constant fibre diameters. The small deviation of the diameter of glass fibres seems not to influence the statistic significantly. Furthermore, same spatial curves were used for the determination of fibre length distributions which were validated by conventional measurements using data from IST AG FibreShape FiVer and FASEP. Comparison shows very good agreement of FLDs using specimen with an edge length of 5 mm. Larger samples showed a bias of the curve where the data derived from CT-scans ends in shorter fibres. Statistical approaches could help to solve the problem of limited sample size using computed tomography in order to evaluate FLDs. The introduced method enables to use a lot of data like curvature, fibre length and orientation distributions which can be utilized for statistics. Furthermore, cut fibres can be localized on the edge of

the specimen to build a statistic about the quantity of fibres cut once, twice, or not at all.

Surface curvature has been calculated by two different approaches based on the Hessian matrix and on a surface patch of variable size utilizing the Gaussian map. Tests on artificial data showed that the method based on the Hessian matrix works much better on small pores or inclusions at lower computation times. Investigations on real images of balls with known diameter confirmed the applicability of both methods on CT-data. Surface curvature can be used as an indicator for notches as a high curvature causes a high notch factor. This information can be used in in-situ tests in order to predict spots for crack initiation. As cracks have a very high curvature, the algorithm could also be used to locate the crack root and thus to keep track of its growth.

List of Figures

2.1	Periodic structures for continuous fibre reinforced materials. . . .	4
2.2	Example of a statistical volume element.	4
2.3	Schematic layout of a commercial computed tomography system.	5
2.4	Bimodal histogram of a grey-scale image.	8
2.5	Graphical solution of the triangle thresholding technique.	12
2.6	26-neighbourhood of a voxel at a finished part of a skeleton (red).	13
2.7	Example of a skeletonization in 2D. Left: Initial image drawn with a line thickness of 10 px. Middle: Image processed by the ImageJ skeletonization by Arganda-Carreras. Right: Result from the <i>AnalyzeSkeleton</i> -algorithm. End-points are illustrated in green, junction points in red and slab voxels in blue.	14
2.8	Exemplary graphical representation of a network that is built by the <i>AnalyzeSkeleton</i> ImageJ plugin from previously skeletonized data as shown in figure 2.7 [30].	15
2.9	Cross section area of a secant plane through a fibre: Stereology makes use of the ellipsoidal cross-section to calculate the fibre orientation [35].	16
2.10	Principle of the orientation analysis using the anisotropic Gaussian Filter. The anisotropic Gaussian filter is rotated to a new coordinate system defined by $\{e'_1, e'_2, e'_3\}$. Fibre A is well aligned to the rotated Gaussian kernel and leads to a high filter response for the currently investigated orientation. Fibre B is badly aligned and leads to a lower response.	18
2.11	Curvature in an one-dimensional line (left) and a two-dimensional image (right). Red lines mark the curvatures of the grey values evaluated in a certain point in both examples. In 1D, there is only one curvature κ . For 2D images, the analysis leads to two curvatures κ_1, κ_2 , where the smaller one can be found in direction of the image structure.	20
2.12	Determining the fibre orientation using the structure tensor [46].	21
2.13	Partitioning of the sphere in 60 fields of equal area using the algorithm introduced and implemented by Leopardi [47].	23

List of Figures

2.14 Definition of orientation angles in 2D and 3D. Blue areas and volumes are taken into account for the orientation distribution histogram while red areas are redundant due to the opposing directions. 24

2.15 Weibull distribution. Blue: Discrete values, Red: Analytical distribution function. 26

2.16 Curvature on 2D an 3D structures. 32

2.17 Illustration of Gauss map. \mathbf{n} shows the normal vector to the surface of an object for a certain point, where the Gaussian map is evaluated. \mathbf{t}_1 and \mathbf{t}_2 illustrate the vectors of the corresponding plane where the surface normal vectors derived from the image gradient in a certain region are mapped to. 34

3.1 GRK 2078 Material. From bottom to top: Continuous carbon fibre SMC, discontinuous glass fibre SMC, hybrid material made of both bulk composites in a sandwich-design with the carbon fibre SMC on the shell and the glass fibre SMC in the core. 39

3.2 CT scan of a woven glass fibre reinforced material with pores. Glass fibres have a good visibility while the contrast of the pores (marked by red circles) is very low. 41

3.3 CT scan of a glass fibre reinforced SMC. 42

3.4 CT scan of a carbon fibre SMC. Carbon fibres can not be separated but the orientation can be seen. 43

3.5 CT scan of a glass fibre reinforced LFT material. Fibres have a high contrast to the matrix an the curvature of the fibres is clearly noticeable. 45

3.6 3D-printed GF reinforced sample. The in-plane printing path is shown by the lines on top of the sample. The arrow on the left illustrates the stacking direction of the single layers. 47

3.7 CT-Scan of 3D printed ABS GF 10 specimen (left) and the unidirectional continuous carbon fibre reinforced specimen (right) [46]. 47

3.8 Location of SMC samples on the originally manufactured plate. 48

3.9 CT scan of balls extracted from ball-bearings for validation of curvature analysis [90]. 50

3.10 CT scan of a carbon fibre reinforced material with pores. Carbon fibres can hardly be recognized while the pores show a high contrast and sharpness. 51

4.1 Program flow chart for the orientation analysis using the anisotropic Gaussian Filter. 54

4.2 Program flow chart for the orientation analysis using the Hessian Matrix. 55

4.3	Flow chart for the structure tensor based orientation analysis.	56
4.4	Partitions of the sphere created with the <i>MATLAB</i> tool of Leopardi. From left to right: Six partitions with centre points in the equator plane / Ten Partitions without centre points in the equator plane / 150 partitions without centre points in the equator plane.	57
4.5	Exemplary orientation histogram using a polar plot. Colour and size of each point in the polar plot illustrate the volume fraction of the corresponding orientation.	58
4.6	Left: Arrangement of the two-fibre models. Images are generated with variable distance d , and angle α . Right: Error in orientation θ_E , which is calculated in each fibre voxel [46].	59
4.7	Principle of the CircularVoting Filter.	63
4.8	Minimum example for additional added method for fibre tracking [30].	67
4.9	B-spline fit of a 13 voxel long fibre. Blue cubes depict the skeletonized fibre with a voxel size of $3\mu\text{m}$. Above: B-spline interval of 20 points. Below: Same B-spline fit with an interval of only 3 points. The fibre is clearly over-fitted.	68
4.10	Parametrization of spatial curves. The moving coordinate system used in the Frenet-Serret equations is defined by the tangent unit vector \mathbf{t} , the binormal unit vector \mathbf{b} and the normal unit vector \mathbf{n}_s	70
4.11	Example of the distance transform and the watershed filter for segmenting binary images.	72
4.12	Watershed segmentation illustrated on an one dimensional example.	73
5.1	YXLON CT Precision computed tomography system.	75
5.2	Artificially generated images of two fibres with certain distance and angle.	77
5.3	Artificial images generated with GeoDict [®] . Left: Unidirectional fibres (\mathbf{N}_U). Right: Fibre architecture with straight fibres and orientation tensor \mathbf{N}_I . Bottom: Fibre architecture with curved fibres and orientation tensor \mathbf{N}_I [46].	79
5.4	Artificially generated sphere for validation of curvature analysis [90].	88
6.1	Anisotropic Gaussian filter: Error measure E_A over aspect ratio α and blurring parameter σ on an artificial single fibre of 10 voxels diameter [46].	92

List of Figures

6.2 Anisotropic Gaussian filter: Fibre architecture dependent error E_A over blurring parameter σ on an artificial image with two fibres. Left: Fibres with 10 voxels in diameter. Right: Fibres with 5 voxels in diameter [46]. 92

6.3 Hessian matrix: Error measure E_A over blurring parameter σ for an artificial single fibre of 5 voxels in diameter (left) and 10 voxels (right). 93

6.4 Hessian matrix: Error measure E_A over blurring parameter σ for an artificial single fibre of 15 voxels in diameter. 93

6.5 Hessian matrix: Fibre architecture dependent error E_A over blurring parameter σ on artificial images with two fibres of 10 voxels in diameter [46]. 94

6.6 Hessian matrix: Fibre architecture dependent error E_A over blurring parameter σ on artificial images with two fibres of 5 voxels in diameter. Left: Coarse sampling. Right: Fine sampling on the same input data at the interesting range of σ [46]. 95

6.7 Structure tensor: Error measure E_A over blurring parameters σ and ρ on an artificial single fibre of 5 voxels diameter. 96

6.8 Structure tensor: Error measure E_A over blurring parameters σ and ρ on artificial images with two fibres of 10 voxels diameter [46]. 97

6.9 Structure tensor: Error measure E_A over blurring parameters σ and ρ on artificial images with two fibres of 10 voxels diameter with high resolution [46]. 97

6.10 Structure tensor: Error measure E_A over blurring parameters σ and ρ on artificial images with two fibres of 5 voxels diameter [46]. 98

6.11 Structure tensor: Error measure E_A over blurring parameters σ and ρ on artificial images with two fibres of 5 voxels diameter and 80 voxels length. 98

6.12 Structure tensor: Error measure E_A over blurring parameters σ and ρ on artificial images with two fibres of 5 voxels diameter. . . 99

6.13 Structure tensor: Error measure E_A over blurring parameters σ and ρ on artificial images with two fibres of 15 voxels diameter. . . 99

6.14 Error E_T resulting from artificial GeoDict[®] images. 100

6.15 Orientation Analysis on GF SMC material using the structure tensor based method. Fibre orientations are coded by colour in HSV colour space. 103

6.16 Orientation analysis on CF SMC material using the structure tensor based method. Fibre orientations are coded by colour in HSV colour space. 104

6.17 Orientation analysis on GF LFT material using the structure tensor based method. Fibre orientations are coded by colour in HSV colour space. 105

6.18 Coherence measure over plate thickness direction for layer segmentation. 106

6.19 Orientation analysis on hybrid specimen within the unidirectional CF including fixation strings made from glass fibres region using the structure tensor based method. Fibre orientations are coded by colour in HSV colour space (b). Note that the colours of the side view correspond to the colour wheel in the top view. . 107

6.20 Fibre volume fractions of GF LFT determined by different histogram based thresholding techniques. Dashed lines illustrate reference values from TGA measurements. 110

6.21 Fibre volume fractions of GF SMC determined by different histogram based thresholding techniques. Dashed lines illustrate reference values from TGA measurements. 111

6.22 Fibre length distribution for samples of all sizes from the IM-LFT plate measured by FiVer. 112

6.23 Fibre length distribution for samples of all sizes from the IM-LFT plate measured by FASEP. 113

6.24 Fibre length distributions of two samples cropped from the IM-LFT plate with an edge length of 5 mm and 10 mm. 114

6.25 Fibre length distributions of the DiCoGF SMC sample with a scanned size of 2.5 mm. 115

6.26 Heatmap of fibre bending radius over fibre length including all fibres within the IM-LFT sample with an edge length of 5 mm. . . 116

6.27 Mass percentage over fibre curvatures of the IM-LFT sample. . . 116

6.28 Mass percentage over fibre curvatures of the DiCo GF SMC sample with a scanned size of 2.5 mm. 117

6.29 Percentage error of surface curvature $E_{c,p}$ examined from spheres of various radius using the Hessian based curvature analysis tool [90]. 118

6.30 Percentage error of surface curvature $E_{c,p}$ examined from spheres of various radius using the patch based curvature analysis tool [90]. 119

6.31 Global curvature histogram of steel balls calculated from the surface curvature analysis tool based on the Hessian matrix [90]. . . 120

6.32 Global curvature histogram of steel balls calculated from the surface curvature analysis tool based on the patch method [90]. . . 120

6.33 Global orientation histogram on steel balls separated by a distance transform and the watershed filter. Dashed lines show the theoretical surface curvature derived from the physical sphere diameter [90]. 121

6.34 Mean curvature analysis on a porous CFRP layup using the Hessian matrix based method. Pore surfaces are coloured with respect to the local curvature. 122

List of Figures

7.1	Cross section area of two touching fibres with an angle of 70° and a diameter of 10 voxels processed by the anisotropic Gaussian filter [46].	124
7.2	Cross section area of two fibres with an angle of 70° and a diameter of 10 voxels processed by the method based on the Hessian matrix [46].	125
7.3	Cross section area of two fibres with an angle of 70° and a diameter of 10 voxels processed by the method based on the structure tensor [46].	126
7.4	Cross section area of two fibres with an angle of 70° and a diameter of 10 voxels processed by the method based on the structure tensor. The slice was rotated 20° about the x-axis to visualize misaligned glyphs on the intersection.	126
7.5	Polar plot of the Young's modulus of a unidirectional glass fibre reinforced polymer [46].	128
7.6	Fibre orientation analysis on artificial image with 20 vol % glass fibres using the method based on anisotropic Gaussian filtering. Fibre orientation is coded by colour using the HSV colour space.	130
7.7	Fibre orientation analysis on artificial image with 20 vol % glass fibres using the method based on the Hessian matrix. Fibre orientation is coded by colour using the HSV colour space.	130
7.8	Fibre orientation analysis on artificial image with 20 vol % glass fibres using the method based on the structure tensor. Fibre orientation is coded by colour using the HSV colour space.	131
7.9	Global image histogram of 10 % GF LFT sample. The red dot illustrates the correct threshold for segmentation with respect to the TGA measurements.	135
7.10	Global image histogram of 20 % GF LFT sample. The red dot illustrates the correct threshold for segmentation with respect to the TGA measurements.	135
7.11	Global image histogram of 30 % GF LFT sample. The red dot illustrates the correct threshold for segmentation with respect to the TGA measurements.	136
7.12	Global image histogram of GF SMC sample B.0_1. The red dot illustrates the correct threshold for segmentation with respect to the TGA measurements.	137
7.13	Fibre length distribution of the IM-LFT sample with an specimen size of 5 mm.	139
7.14	Fibre length distribution of the IM-LFT sample with an specimen size of 10 mm.	140
7.15	Plot of a random subset of fibres longer than 4 mm and a mean bending radius of $0.5 \text{ mm} \leq r \leq 1.5 \text{ mm}$ derived from the IM-LFT sample with a size of 5 mm.	141

7.16 Plot of a random subset of fibres longer than 0.7 mm and a mean fibre bending radius $r \geq 3$ mm derived from the IM-LFT sample with a size of 5 mm. 142

7.17 Plot of a random subset of fibres longer than 0.5 mm and a mean bending radius higher than 2 mm derived from the DiCo GF SMC sample with a size of 2.5 mm. 143

7.18 Plot of a random subset of fibres longer than 0.5 mm and a mean fibre bending radius lower than 2 mm derived from the DiCo GF SMC sample with a size of 2.5 mm. 144

7.19 Curvature derived from the CT-scan of bearing balls by the Hessian-based method. 146

7.20 3D representation of curvature derived from the CT-scan of bearing balls by the Hessian-based method with $\sigma=10$ voxels. 146

7.21 Curvature derived from the CT-scan of bearing balls by the patch-based method. 148

List of Tables

3.1	Primary continuous and discontinuous fibre reinforced materials	45
4.1	Exemplary output file for three dimensional fibre paths extracted from a volumetric image by the modified ImageJ plugin AnalyzeSkeleton.	66
5.1	Variable input parameters for orientation analysis tools for optimization.	77
5.2	Image acquisition parameters for 3D-printed glass fibre reinforced ABS sample.	79
5.3	Image acquisition parameters for carbon fibre reinforced pultrusion rod.	80
5.4	Image acquisition parameters for GF SMC sample	81
5.5	Image acquisition parameters for CF SMC sample	81
5.6	Image acquisition parameters for Hybrid sample	81
5.7	Image acquisition parameters for GF LFT sample	82
5.8	Image acquisition parameters for LFT samples	82
5.9	Image acquisition parameters for SMC samples	83
5.10	Image acquisition parameters for injection moulded LFT samples with an edge length of 5 mm	85
5.11	Image acquisition parameters for injection moulded LFT samples with an edge length of 10 mm	85
5.12	Input parameters for the circular voting filtering of the IM-LFT samples with an edge length of 5 mm	86
5.13	Input parameters for the circular voting filtering of the IM-LFT samples with an edge length of 10 mm	86
5.14	Image acquisition parameters for FLD sample of DiCo GF SMC. The scan was carried out by the Zeiss Xradia 520 Versa X-Ray microscope.	87
5.15	Input parameters for the circular voting filtering of the DiCo GF SMC samples with an edge length of 2.5 mm	87
5.16	Image acquisition parameters for steel balls extracted from ball-bearings	89
5.17	Image acquisition parameters for porous CFRP-layup shown in figure 3.10	89

List of Tables

6.1	Error E_T of artificial images from GeoDict®.	101
6.2	Computation times and memory consumption for artificial images with a size of 500^3 voxels and a bit depth of 16 bit.	101
6.3	Orientation Tensors derived from 3D-printed glass fibre reinforced specimen.	101
6.4	Orientation Tensors derived from unidirectional carbon fibre reinforced polymer rod.	102
6.5	Fibre content of SMC samples determined by TGA.	108
6.6	Fibre content of LFT samples determined by TGA.	108
7.1	Fibre architecture dependent error E_A resulting from investigated methods with different fibre diameters.	127
7.2	Number of investigated fibres by FASEP and FiVer for each sample.	138

Bibliography

Publications

- [1] Martin Ostoja-Starzewski. „Material spatial randomness: From statistical to representative volume element“. In: *Probabilistic Engineering Mechanics* 21.2 (2006), pp. 112–132.
- [2] Thorsten M. Buzug. *Computed tomography: from photon statistics to modern cone-beam CT*. Springer Science & Business Media, 2008.
- [3] L.A. Feldkamp, L.C. Davis, and J.W. Kress. „Practical cone-beam algorithm“. In: *JOSA A* 1.6 (1984), pp. 612–619.
- [4] Frank Natterer. *The mathematics of computerized tomography*. SIAM, 2001.
- [5] Hans J. Johnson, Matthew M. McCormick, and Luis Ibanez. „The ITK Software Guide Book 2: Design and Functionality Fourth Edition Updated for ITK version 4.7“. In: *Kitware, Inc.(January 2015)* (2015).
- [6] W. Schroeder, K. Martin, and B. Lorensen. *VTK Textbook 4th edition*. Kitware. 2006.
- [8] Caroline A. Schneider, Wayne S. Rasband, and Kevin W. Eliceiri. „NIH Image to ImageJ: 25 years of image analysis“. In: *Nature methods* 9.7 (2012), pp. 671–675.
- [9] Johannes Schindelin, Curtis T. Rueden, Mark C. Hiner, and Kevin W. Eliceiri. „The ImageJ ecosystem: An open platform for biomedical image analysis“. In: *Molecular reproduction and development* 82.7-8 (2015), pp. 518–529.
- [10] Johannes Schindelin et al. „Fiji: an open-source platform for biological-image analysis“. In: *Nature methods* 9.7 (2012), pp. 676–682.
- [11] Bernd Jähne. *Digitale Bildverarbeitung und Bildgewinnung*. Springer-Verlag Berlin Heidelberg, 2012.
- [12] Luis Ibanez Will Schroeder Lydia Ng Josh Cates and the Insight Software Consortium. *itk software guide*. <http://www.itk.org>, 2005.

BIBLIOGRAPHY

- [13] Terry S. Yoo, Michael J. Ackerman, William E. Lorensen, Will Schroeder, Vikram Chalana, Stephen Aylward, Dimitris Metaxas, and Ross Whitaker. „Engineering and Algorithm Design for an Image Processing API: A Technical Report on ITK - the Insight Toolkit“. In: *Insight Journal* (2002), pp. 586–592.
- [14] Antti Niemistö. *A Comparison of Nonparametric Histogram-Based Thresholding Algorithms*. Oct. 2004.
- [15] Antti Niemistö. *HistThresh toolbox*. Open Source Software. Apr. 2014.
- [16] T. W. Ridler and S. Calvard. „Picture Thresholding Using an Iterative Selection Method“. In: *IEEE Transactions on Systems, Man, and Cybernetics* 8.8 (1978), pp. 630–632.
- [17] Liang-Kai Huang and Mao-Jiun J. Wang. „Image thresholding by minimizing the measures of fuzziness“. In: *Pattern Recognition* 28.1 (1995), pp. 41–51.
- [18] Judith M. S. Prewitt and Mortimer L. Mendelsohn. „The Analysis of Cell Images“. In: *Annals of the New York Academy of Sciences* 128.3 (1966), pp. 1035–1053.
- [19] J.N. Kapur, P.K. Sahoo, and A.K.C. Wong. „A new method for gray-level picture thresholding using the entropy of the histogram“. In: *Computer Vision, Graphics, and Image Processing* 29.3 (1985), pp. 273–285.
- [20] C.A. Glasbey. „An Analysis of Histogram-Based Thresholding Algorithms“. In: *CVGIP: Graphical Models and Image Processing* 55.6 (1993), pp. 532–537.
- [21] Abhijit G. Shanbhag. „Utilization of information measure as a means of image thresholding“. In: *CVGIP: Graphical Models and Image Processing* 56.5 (1994), pp. 414–419.
- [22] J. Kittler and J. Illingworth. „Minimum error thresholding“. In: *Pattern Recognition* 19.1 (1986), pp. 41–47.
- [23] Wen-Hsiang Tsai. „Moment-preserving thresholding: A new approach“. In: *Computer Vision, Graphics, and Image Processing* 29.3 (1985), pp. 377–393.
- [24] Nobuyuki Otsu. „A threshold selection method from gray-level histograms“. In: *IEEE transactions on systems, man, and cybernetics* 9.1 (1979), pp. 62–66.
- [25] Worthie Doyle. „Operations useful for similarity-invariant pattern recognition“. In: *Journal of the ACM (JACM)* 9.2 (1962), pp. 259–267.
- [26] G.W. Zack, W.E. Rogers, and S.A. Latt. „Automatic measurement of sister chromatid exchange frequency.“ In: *Journal of Histochemistry & Cytochemistry* 25.7 (1977), pp. 741–753.

- [27] H. Homann. „Implementation of a 3D thinning algorithm“. In: *Insight Journal* (Oct. 2007).
- [28] T. C. Lee, R. L. Kashyap, and C. N. Chu. „Building Skeleton Models via 3-D Medial Surface Axis Thinning Algorithms“. In: *CVGIP: Graphical Models and Image Processing* 56.6 (1994), pp. 462–478.
- [29] Ignacio Arganda-Carreras. *Skeleton3D and AnalyzeSkeleton for Fiji*. online. 2008.
- [31] Sabine Predak. „Mikrowellen-Orientierungsmessungen zur zerstörungsfreien Charakterisierung kurzfaserverstärkter Kunststoffe“. PhD thesis. Universität Stuttgart, 2008.
- [32] Ervin E. Underwood. „The mathematical foundations of quantitative stereology“. In: *Stereology and Quantitative Metallography*. ASTM International, 1972.
- [33] S. Fakirov and C. Fakirova. „Direct determination of the orientation of short glass fibers in an injection-molded poly(ethylene terephthalate) system“. In: *Polymer Composites* 6.1 (1985), pp. 41–46.
- [34] G. Fischer, P. Schwarz, U. Mueller, and U. Fritz. „Measuring spatial fiber orientation - A method for quality control of fiber reinforced plastics“. In: *Advances in Polymer Technology* 10.2 (1990), pp. 135–141.
- [35] T. Komori and K. Marishima. „Estimation of Fiber Orientation and Length in Fiber Assemblies“. In: *Textile Research Journal* 48.6 (1978), pp. 309–314.
- [36] N. C. Davidson, A. R. Clarke, and G. Archenhold. „Large-area, high-resolution image analysis of composite materials“. In: *Journal of Microscopy* 185.2 (1997), pp. 233–242.
- [37] K. Robb, O. Wirjadi, and K. Schladitz. „Fiber Orientation Estimation from 3D Image Data: Practical Algorithms, Visualization, and Interpretation“. In: *Proceedings of the 7th International Conference on Hybrid Intelligent Systems*. IEEE Computer Society, 2007, pp. 320–325.
- [38] O. Wirjadi, K. Schladitz, A. Rack, and T. Breuel. „Applications of Anisotropic Image Filters for Computing 2d and 3d-fiber Orientations“. In: *Stereology and Image Analysis—10th European Congress of ISS*. 2009.
- [39] Oliver Wirjadi. „Models and algorithms for image-based analysis of microstructures“. PhD thesis. Technische Universität Kaiserslautern, 2009.
- [40] J. Fliege and U. Maier. „The distribution of points on the sphere and corresponding cubature formulae“. In: *IMA Journal of Numerical Analysis* 19.2 (1999), pp. 317–334.
- [41] Rudolf Rothe. „Zum problem des talwegs“. In: *Sitz. ber. d. Berliner Math. Gesellschaft* 14 (1915), pp. 51–69.

BIBLIOGRAPHY

- [42] P. J. Elbischger, H. Bischof, P. Regitnig, and G. A. Holzapfel. „Automatic analysis of collagen fiber orientation in the outermost layer of human arteries“. In: *Pattern Analysis and Applications* 7.3 (2004), pp. 269–284.
- [43] F. Daniels, B.M. ter Haar Romenij, M. P. Rubbens, and H. C. van Assen. „Quantification of Collagen Orientation in 3D Engineered Tissue“. In: *Proc. Intern. Conf. on Biomedical Engineering BioMed 2006*. Ed. by F. Ibrahim. 2006, pp. 344–348.
- [44] Michael van GINKEL. „Image Analysis using Orientation Space based on Steerable Filters“. PhD thesis. Technische Universiteit Delft, 2002.
- [45] M. Krause, J. M. Hausherr, B. Burgeth, C. Herrmann, and W. Krenkel. „Determination of the fibre orientation in composites using the structure tensor and local X-ray transform“. In: *Journal of Materials Science* 45.4 (2010), pp. 888–896.
- [47] Paul Leopardi. „A Partition of the Unit Sphere into Regions of Equal Area and Small Diameter“. In: *Electronic Transactions on Numerical Analysis* Volume 25 (2006), p309–327.
- [48] S. G. Advani and C. L. Tucker. „The Use of Tensors to Describe and Predict Fiber Orientation in Short Fiber Composites“. In: *Journal of Rheology* 31 (1987), pp. 751–784.
- [49] Maher Moakher and Peter J. Basser. „Fiber Orientation Distribution Functions and Orientation Tensors for Different Material Symmetries“. In: *Visualization and Processing of Higher Order Descriptors for Multi-Valued Data*. Ed. by Ingrid Hotz and Thomas Schultz. Cham: Springer International Publishing, 2015, pp. 37–71.
- [50] K. V. Mardia. „Statistics of Directional Data“. In: *Journal of the Royal Statistical Society. Series B (Methodological)* 37.3 (1975), pp. 349–393.
- [51] Nicholas I. Fisher, Toby Lewis, and Brian J.J. Embleton. *Statistical analysis of spherical data*. Cambridge university press, 1987.
- [52] K.G. Van den Boogaart, Ralf Hielscher, J. Prestin, and H. Schaeben. „Kernel-based methods for inversion of the Radon transform on $SO(3)$ and their applications to texture analysis“. In: *Journal of Computational and Applied Mathematics* 199.1 (2007), pp. 122–140.
- [53] H. Schaeben. „A simple standard orientation density function: The hyperspherical de la Vallée Poussin kernel“. In: *Physica Status Solidi (B)* 200.2 (1997), pp. 367–376.
- [54] Shao-Yun Fu and Bernd Lauke. „Effects of fiber length and fiber orientation distributions on the tensile strength of short-fiber-reinforced polymers“. In: *Composites Science and Technology* 56.10 (1996), pp. 1179–1190.

- [55] J. Andersons, R. Joffe, M. Hojo, and S. Ochiai. „Glass fibre strength distribution determined by common experimental methods“. In: *Composites Science and Technology* 62.1 (2002), pp. 131–145.
- [56] Nicolas Le Moigne, Martien van den Oever, and Tatiana Budtova. „A statistical analysis of fibre size and shape distribution after compounding in composites reinforced by natural fibres“. In: *Composites Part A: Applied Science and Manufacturing* 42.10 (2011), pp. 1542–1550.
- [57] A. Bernasconi, P. Davoli, A. Basile, and A. Filippi. „Effect of fibre orientation on the fatigue behaviour of a short glass fibre reinforced polyamide-6“. In: *International Journal of Fatigue* 29.2 (2007), pp. 199–208.
- [58] *Textile-glass-reinforced plastics - Prepregs, moulding compounds and laminates - Determination of the textile-glass and mineral-filler content; calcination methods (ISO 1172:1996); German version EN ISO 1172:1998*. DIN Deutsches Institut für Normung e. V., DIN German Institute for Standardization.
- [59] Mark R Hartwich, Norbert Höhn, Helga Mayr, Konrad Sandau, and Ralph Stengler. „FASEP® ULTRA-Automated Analysis of fibre length distribution in glass-fibre-reinforced products“. In: *SPIE Europe Optical Metrology*. International Society for Optics and Photonics. 2009, pp. 738921–738921.
- [60] Ralph Stengler, Konrad Sandau, Mark Rafael Hartwich, Norbert Höhn, and Helga Mayr. „Neuartige Prozessplanung und -steuerung bei der Verarbeitung von Langfaserverstärkten Thermoplasten (LFT) mittels einer neuen bildanalytischen Bestimmung von Faserlängenverteilungen“. In: *Querschnitt* 23 (Mar. 2009).
- [61] D. Salaberger, K. A. Kannappan, J. Kastner, J. Reussner, and T. Auinger. „Evaluation of Computed Tomography Data from Fibre Reinforced Polymers to Determine Fibre Length Distribution“. In: *International Polymer Processing* 26.3 (2011), pp. 283–291.
- [62] Matthias Teßmann, Stephan Mohr, Svitlana Gayetskyy, Ulf Haßler, Randolph Hanke, and Günther Greiner. „Automatic Determination of Fiber-Length Distribution in Composite Material Using 3D CT Data“. In: *EURASIP Journal on Advances in Signal Processing* 2010.1 (2010), p. 545030.
- [63] A. F. Frangi, W. J. Niessen, R. M. Hoogeveen, T. van Walsum, and M. A. Viergever. „Model-based quantitation of 3-D magnetic resonance angiographic images“. In: *IEEE Transactions on Medical Imaging* 18.10 (1999), pp. 946–956.

BIBLIOGRAPHY

- [64] Franz Pfeifer, Johann Kastner, and Rotraud Freytag. „Method for three-dimensional evaluation and visualization of the distribution of fibres in glass-fibre reinforced injection molded parts by μ -X-ray computed tomography“. In: *17th world conference on nondestructive testing*. 2008, pp. 1–7.
- [65] Dietmar Salaberger, Michael Jerabek, Thomas Koch, and Johann Kastner. „Consideration of Accuracy of Quantitative X-Ray CT Analyses for Short-Glass-Fibre-Reinforced Polymers“. In: *Materials Science Forum* 825-826 (2015), pp. 907–913.
- [66] Katja K. Narva, Lippo V.J. Lassila, and Pekka K. Vallittu. „Fatigue resistance and stiffness of glass fiber-reinforced urethane dimethacrylate composite“. In: *The Journal of prosthetic dentistry* 91.2 (2004), pp. 158–163.
- [67] Derek Hull and T.W. Clyne. *An introduction to composite materials*. Cambridge university press, 1996.
- [69] A. Elmoutaouakkil, L. Salvo, E. Maire, and G. Peix. „2D and 3D Characterization of Metal Foams Using X-ray Tomography“. In: *Advanced Engineering Materials* 4.10 (2002), pp. 803–807.
- [70] C.L. Lin and J.D. Miller. „3D characterization and analysis of particle shape using X-ray microtomography (XMT)“. In: *Powder Technology* 154.1 (2005), pp. 61–69.
- [71] William E. Lorensen and Harvey E. Cline. „Marching cubes: A high resolution 3D surface construction algorithm“. In: *ACM siggraph computer graphics*. Vol. 21. 4. ACM. 1987, pp. 163–169.
- [72] Loring W. Tu. *Differential Geometry: Connections, Curvature, and Characteristic Classes*. Vol. 275. Springer, 2017.
- [73] Brian Avants and James Gee. „The Shape Operator for Differential Analysis of Images“. In: *Information Processing in Medical Imaging: 18th International Conference, IPMI 2003, Ambleside, UK, July 20-25, 2003. Proceedings*. Ed. by Chris Taylor and J. Alison Noble. Berlin, Heidelberg: Springer Berlin Heidelberg, 2003, pp. 101–113.
- [74] Brian B. Avants, Nicholas J. Tustison, Gang Song, Philip A. Cook, Arno Klein, and James C. Gee. „A reproducible evaluation of ANTs similarity metric performance in brain image registration“. In: *NeuroImage* 54.3 (2011), pp. 2033–2044.
- [75] Hans J. Johnson Brian B. Avants Nicholas J. Tustison. *Advanced Normalization Tools (ANTs)*. OpenSource project.
- [76] John F. Hughes. „Differential geometry of implicit surfaces in 3-space-a primer“. In: *Report, Department of Computer Science Brown University Providence, Rhode Island* (2003).

- [77] Peter Dombrowski. „Krümmungsgrößen gleichungsdefinierter Untermannigfaltigkeiten RIEMANNscher Mannigfaltigkeiten“. In: *Mathematische Nachrichten* 38.3-4 (1968), pp. 133–180.
- [79] Viktor Müller, Barthel Brylka, Felix Dillenberger, Robert Glöckner, Stefan Kolling, and Thomas Böhlke. „Homogenization of elastic properties of short-fiber reinforced composites based on measured microstructure data“. In: *Journal of Composite Materials* 50.3 (2016), pp. 297–312.
- [81] Viktor Müller. *Micromechanical modeling of short-fiber reinforced composites*. Karlsruhe, 2016.
- [83] Y. Benveniste. „A new approach to the application of Mori-Tanaka’s theory in composite materials“. In: *Mechanics of materials* 6.2 (1987), pp. 147–157.
- [85] Du Hwan Chung and Tai Hun Kwon. „Invariant-based optimal fitting closure approximation for the numerical prediction of flow-induced fiber orientation“. In: *Journal of rheology* 46.1 (2002), pp. 169–194.
- [86] Laurent Orgéas, Pierre J. J. Dumont, and Luigi Nicolais. „Sheet Molding Compounds“. In: *Wiley Encyclopedia of Composites*. Ed. by L. Nicolais and A. Borzacchiello. Hoboken, NJ, USA: John Wiley & Sons, Inc, 2011.
- [87] David Bücheler. „Locally Continuous-fiber Reinforced Sheet Moulding Compounds“. PhD thesis. KIT, 2017.
- [88] W. Krause, F. Henning, S. Tröster, O. Geiger, and P. Eyerer. „LFT-D A Process Technology for Large Scale Production of Fiber Reinforced Thermoplastic Components“. In: *Journal of Thermoplastic Composite Materials* 16.4 (2003), pp. 289–302.
- [91] D. S. Paik, C. F. Beaulieu, G. D. Rubin, B. Acar, R. B. Jeffrey, J. Yee, J. Dey, and S. Napel. „Surface normal overlap: a computer-aided detection algorithm with application to colonic polyps and lung nodules in helical CT“. In: *IEEE Transactions on Medical Imaging* 23.6 (2004), pp. 661–675.
- [92] Tanaka Mori and K. Tanaka. „Average stress in matrix and average elastic energy of materials with misfitting inclusions“. In: *Acta metallurgica* 21.5 (1973), pp. 571–574.
- [94] T. Böhlke and C Brüggemann. „Graphical representation of the generalized Hookes law“. In: *Technische Mechanik* 21.2 (2001), pp. 145–158.
- [95] A. M. Lopez, F. Lumbreras, J. Serrat, and J. J. Villanueva. „Evaluation of methods for ridge and valley detection“. In: *IEEE Transactions on Pattern Analysis and Machine Intelligence* 21.4 (1999), pp. 327–335.
- [96] Malte Kuhlmann and Claudia Redenbach. „Estimation of Fibre Length Distributions from Fibre Endpoints“. In: *Scandinavian Journal of Statistics* 42.4 (2015), pp. 1010–1022.

BIBLIOGRAPHY

- [97] Kanatani Ken-Ichi. „Distribution of directional data and fabric tensors“. In: *International Journal of Engineering Science* 22.2 (1984), pp. 149–164.

Own Publications

- [7] Benjamin Bertram and Pascal Pinter. *Composight*. Sourceforge, 2015.
- [30] Pascal Pinter, Benjamin Bertram, and Kay André Weidenmann. „A Novel Method for the Determination of Fibre Length Distributions from μ CT-data“. In: *6th Conference on Industrial Computed Tomography, Wels, Austria (iCT 2016)*. 2016.
- [46] Pascal Pinter, Stefan Dietrich, Benjamin Bertram, Loredana Kehrer, Peter Elsner, and Kay André Weidenmann. „Comparison and error estimation of 3D fibre orientation analysis of computed tomography image data for fibre reinforced composites“. In: *NDT & E International* (2018).
- [68] Benjamin Bertram, Pascal Pinter, and Kay André Weidenmann. „Non-destructive Determination of the local Fiber Volume Content in flat AL(OH)₃-filled SMC Parts from ray Projections“. In: *Proceedings of the 17th European Conference on Composite Materials ECCM 17*. 2016.
- [78] Trevor Sabiston, Pascal Pinter, Julie Lévesque, Kay André Weidenmann, and Kaan Inal. „Evaluating the number of pseudo grains required in a two-step homogenization to predict the response of sheet moulding compound composites from the exact fibre orientation distribution“. In: *Composites Part A (submitted)* (2018).
- [80] Loredana Kehrer, Pascal Pinter, and Thomas Böhlke. „Homogenization of temperature-dependent short fibre reinforced polypropylen and experimental investigations of long fibre reinforced vinylester“. In: *Proceedings in Applied Mathematics and Mechanics*. Proceedings to 17th European Conference on Composite Materials, 2016.
- [82] Matthew Bondy, Pascal Pinter, and William Altenhof. „Experimental characterization and modelling of the elastic properties of direct compounded compression molded carbon fibre/polyamide 6 long fibre thermoplastic“. In: *Materials & Design* 122 (2017), pp. 184–196.
- [84] Bartholomäus Brylka, Pascal Pinter, Kay Weidenmann, and Thomas Böhlke. „X-ray computed tomography based stiffness approximation of long fiber reinforced polypropylene“. In: *Composites Science and Technology (submitted)* (2018).

- [89] Anselm Heuer, Pascal Pinter, and Kay André Weidenmann. „Analysis of the Effects of Raster Orientation in Components Consisting of Short Glass Fibre Reinforced ABS of Different Fibre Volume Fraction Produced by Additive Manufacturing“. In: *Key Engineering Materials*. Vol. 742. Trans Tech Publ. 2017, pp. 482–489.
- [90] Pascal Pinter, Benjamin Bertram, and Kay André Weidenmann. „Algorithms for the Determination of Curvature from 3D -CT Images A Comparison“. In: *Proceedings of the 2nd International Conference Euro Hybrid*. 2016.
- [93] Loredana Kehrer, Pascal Pinter, and Thomas Böhlke. „Mean and full field homogenization of artificial long fiber reinforced thermoset polymers.“ In: *Proceedings in Applied Mathematics and Mechanics*. 2017 (submitted).